

Surrogate models for diffusive transport in radially-symmetric media

Luke Patrick Filippini

BMath

Submitted in fulfilment of the
requirement for the degree of
Master of Philosophy (Mathematics)



School of Mathematical Sciences
Faculty of Science
Queensland University of Technology
2023

Keywords

Radially-symmetric, Stochastic Diffusion, Surrogate Modelling,
Weighted Exponential Model, Heterogeneous Media

Acknowledgements

First and foremost, I want to extend my deep gratitude and thanks to my Principal Supervisor Dr Elliot Carr and Associate Supervisor Prof Matthew Simpson for their guidance and support throughout my degree. Your contributions, knowledge and honest feedback have been invaluable to me, and I have benefited enormously as a researcher, presenter and individual as a result. Thank you both for your time, effort and patience.

I also acknowledge the support provided to me by the School of Mathematical Sciences, within the Faculty of Science at QUT, during my candidature. This research was supported by an Australian Government Research Training Program Scholarship. I am grateful to have had the opportunity to present my work at multiple conferences: QANZIAM, CTAC and ANZIAM. Additionally, I want to sincerely thank the Australian Mathematical Sciences Institute (AMSI) which covered my accommodation costs during my attendance at AMSI Summer School 2023. I was able to complete a coursework unit as part of my attendance and took the opportunity to give a brief presentation about the work presented in this thesis.

I must also acknowledge and thank my friends and family for their support during this whole process. In particular, I want to thank my friends and peers at QUT who have freely supported me through both my successes and setbacks. Also, I want to give a special mention to my high school maths teacher, Ms Jones, whose teaching, listening and support contributed to the betterment of my character and my love for mathematics. Lastly, to my mum, Belinda, and dad, Garry, thank you for your love, support and reassurance during the challenges and breakthroughs in and outside my work. I wouldn't have achieved this without you.

Abstract

Mathematical modelling of diffusion-controlled transport is a fundamental tool applied across numerous disciplines, including biology, physics and medicine. Important applications include drug delivery from cylindrical and spherical capsules and the drying of thin agricultural products. In this thesis, we consider diffusion-controlled release of particles from geometries with radial symmetry. A quantity commonly used to characterise such diffusive processes is the proportion of particles remaining within the geometry over time, denoted as $\mathcal{P}(t)$. Traditionally, $\mathcal{P}(t)$ is modelled using a stochastic or continuum approach. However, the stochastic approach is time-consuming, computationally expensive and lacks analytical insight into the influence of key physical parameters on the release profile. Furthermore, the continuum approach yields complicated infinite series solutions which obscure the precise effect of each physical parameter on $\mathcal{P}(t)$ and convolute the fitting of experimental release data. To address these issues, we develop surrogate models that provide relatively simple closed-form analytical approximations of $\mathcal{P}(t)$ which are computationally inexpensive to evaluate. Surrogate models are frequently used in drug delivery and thin-layer drying applications to describe quantities analogous to $\mathcal{P}(t)$. These models provide meaningful insight into the precise influence of important physical parameters on the release profile. This implies, for example, that a drug delivery capsule or drying chamber can then be optimised to achieve a desired release profile while minimising experimental testing.

Here, we develop several simple one-term, two-term and weighted two-term surrogate models to approximate $\mathcal{P}(t)$ by matching moments with the continuum analogue of the stochastic diffusion model. These models are developed for homogeneous slab, circular, annular, spherical and spherical shell geometries with a constant particle movement probability and heterogeneous slab, circular, annular and spherical geometries comprised of two concentric layers with different particle movement probabilities. Each model is easy to evaluate and provides analytical insight into the influence of key physical parameters of the diffusive transport system, including the dimension, diffusivity, geometry and boundary conditions, on $\mathcal{P}(t)$. The weighted two-term model captures the stochastic and continuum descriptions of $\mathcal{P}(t)$ with the highest degree of accuracy.

Contents

Keywords	i
Acknowledgements	ii
Abstract	iii
List of Figures	vi
List of Tables	vii
1 Introduction	1
1.1 Overview	1
1.1.1 Application to drug delivery and food drying	3
1.1.2 Surrogate models	3
1.1.3 Thesis contributions	5
1.2 Objectives and structure	5
2 Simplified models of diffusion in radially-symmetric geometries	8
2.1 Introduction	8
2.2 Stochastic model	10
2.2.1 Homogeneous geometry	11
2.2.2 Heterogeneous geometry	11
2.2.3 Boundary conditions	12
2.2.4 Calculation of $\mathcal{P}(t)$	12
2.3 Continuum model	12
2.3.1 Homogeneous geometry	13
2.3.2 Heterogeneous geometry	13
2.3.3 Boundary conditions	14
2.3.4 Calculation of $\mathcal{P}(t)$	14
2.4 Surrogate models	15
2.4.1 Motivation	15
2.4.2 Moments	16
2.4.3 Surrogate model 1: One-term exponential model	17
2.4.4 Surrogate model 2: Two-term exponential model	19

2.4.5	Surrogate model 3: Weighted two-term exponential model	22
2.5	Results	26
2.6	Conclusion	30
3	Supporting information for surrogate model development	31
3.1	Analysis of analytical solutions for $\mathcal{P}_c(t)$	31
3.1.1	Separation of variables and eigenfunction expansion	31
3.1.2	Limitations of continuum models	33
3.1.3	Initial value problem for $\mathcal{P}_c(t)$	35
3.2	Surrogate model development and analysis	35
3.2.1	One-term model	35
3.2.2	Two-term model	39
3.2.3	Weighted two-term model	44
3.2.4	Parameter estimation using one-term model (2.35)	46
3.3	Finite volume and time stepping schemes	46
3.3.1	Homogeneous materials	47
3.3.2	Heterogeneous materials	48
3.3.3	Crank-Nicolson method	50
3.4	Results for one- and three-dimensional geometries	51
3.5	Additional project considerations	55
3.5.1	Non-zero steady-state	55
3.5.2	Smooth diffusivity function	56
3.5.3	Addition of reaction term	57
4	Conclusion	59
4.1	Summary and discussion	59
4.2	Future work	60
Appendix		62
Bibliography		64

List of Figures

1.1	Diffusion-controlled release of particles from homogeneous radially-symmetric geometries	2
1.2	Stochastic and continuum models of particle release from a homogeneous annular geometry	2
1.3	Stochastic and continuum values for $\mathcal{P}(t)$ compared with example surrogate exponential models	5
2.1	Stochastic and continuum calculations for $\mathcal{P}(t)$ compared with an example surrogate model for a homogeneous annular geometry	9
2.2	Surrogate exponential models compared with stochastic and continuum models for the homogeneous test cases (two-dimensional geometries)	28
2.3	Surrogate exponential models compared with stochastic and continuum models for the heterogeneous test cases (two-dimensional geometries)	29
3.1	Series solutions for continuum models compared with numerical results for a homogeneous slab, disc and sphere	34
3.2	Comparison between analytical and numerical solutions for $M_0(r)$	37
3.3	Comparisons between analytical and numerical solutions for $M_1(r)$	42
3.4	Schematic of a vertex-centred finite volume discretisation for a homogeneous radially-symmetric geometry	47
3.5	Schematic of a vertex-centred finite volume discretisation for a heterogeneous radially-symmetric geometry	48
3.6	Surrogate exponential models compared with stochastic and continuum models for the homogeneous test cases (one-dimensional geometries)	52
3.7	Surrogate exponential models compared with stochastic and continuum models for the homogeneous test cases (three-dimensional geometries)	53
3.8	Surrogate exponential models compared with stochastic and continuum models for the heterogeneous test cases (one-dimensional geometries)	54
3.9	Surrogate exponential models compared with stochastic and continuum models for the heterogeneous test cases (three-dimensional geometries)	54

List of Tables

2.1	Geometry and boundary parameters for seven cases	18
2.2	Geometry and boundary parameter values for seven test cases	27
2.3	Mean absolute errors for the Weibull model of Carr [18]	30
3.1	Numerical roots of transcendental equations	34
A1	Surrogate model parameters (one-dimensional geometries)	62
A2	Surrogate model parameters (two-dimensional geometries)	62
A3	Surrogate model parameters (three-dimensional geometries)	63

Chapter 1

Introduction

1.1 Overview

Mathematical modelling of transport phenomena is a valuable tool applied across numerous disciplines, including biology [1–5], ecology [4, 6, 7], physics [8–10], medicine [11, 12] and other fields [13, 14]. The most ubiquitous component of transport processes is arguably diffusion, and many fields of research require an understanding of systems that are diffusion-controlled or dominated [1, 4, 14]. To elaborate, a mathematical interpretation of diffusive transport is, for example, fundamental for the estimation of material thermal properties [15, 16], a useful tool for providing insight into animal migration patterns [4] and vital for the improvement of effective disease treatment [5, 11, 17]. Here, we focus on the diffusion-controlled release of particles over time from geometries with radial symmetry, such as discs, annuli, spheres and spherical shells, which arise in drug delivery and food drying applications (Fig. 1.1).

A quantity frequently used to characterise diffusive processes is the proportion of particles remaining within the geometry over time, denoted as $\mathcal{P}(t)$ [18–21]. Traditionally, $\mathcal{P}(t)$ is modelled using a stochastic or continuum approach. The stochastic approach requires performing repeated simulations of an unbiased random walk model governing particle movement in a radially-symmetric domain. The quantity $\mathcal{P}(t)$ is computed by normalising the number of remaining particles over time for each simulation by the total number of particles (see section 2.2) (Fig. 1.2(a)). In this work, we assume that particles are initially uniformly distributed throughout the geometry. For the continuum approach, $\mathcal{P}(t)$ is computed by determining the continuum analogue of the stochastic model (Fig. 1.2(b)) and then calculating the spatial average of the solution (see section 2.3) (Fig. 1.2(c)).

However, the stochastic and continuum approaches have their limitations. Firstly, computing $\mathcal{P}(t)$ using the stochastic approach can be time-consuming and computationally expensive. Furthermore, there is limited insight that can be obtained into the effect of physical parameters (e.g. dimension, diffusivity, geometry and boundary conditions) on the release profile¹. Moreover, the continuum approach yields complicated infinite series solutions for $\mathcal{P}(t)$ [18, 22, 23]. Although these continuum expressions are analytical, their use requires truncation and repeated

¹The term ‘release profile’ refers to the quantity $\mathcal{P}(t)$.

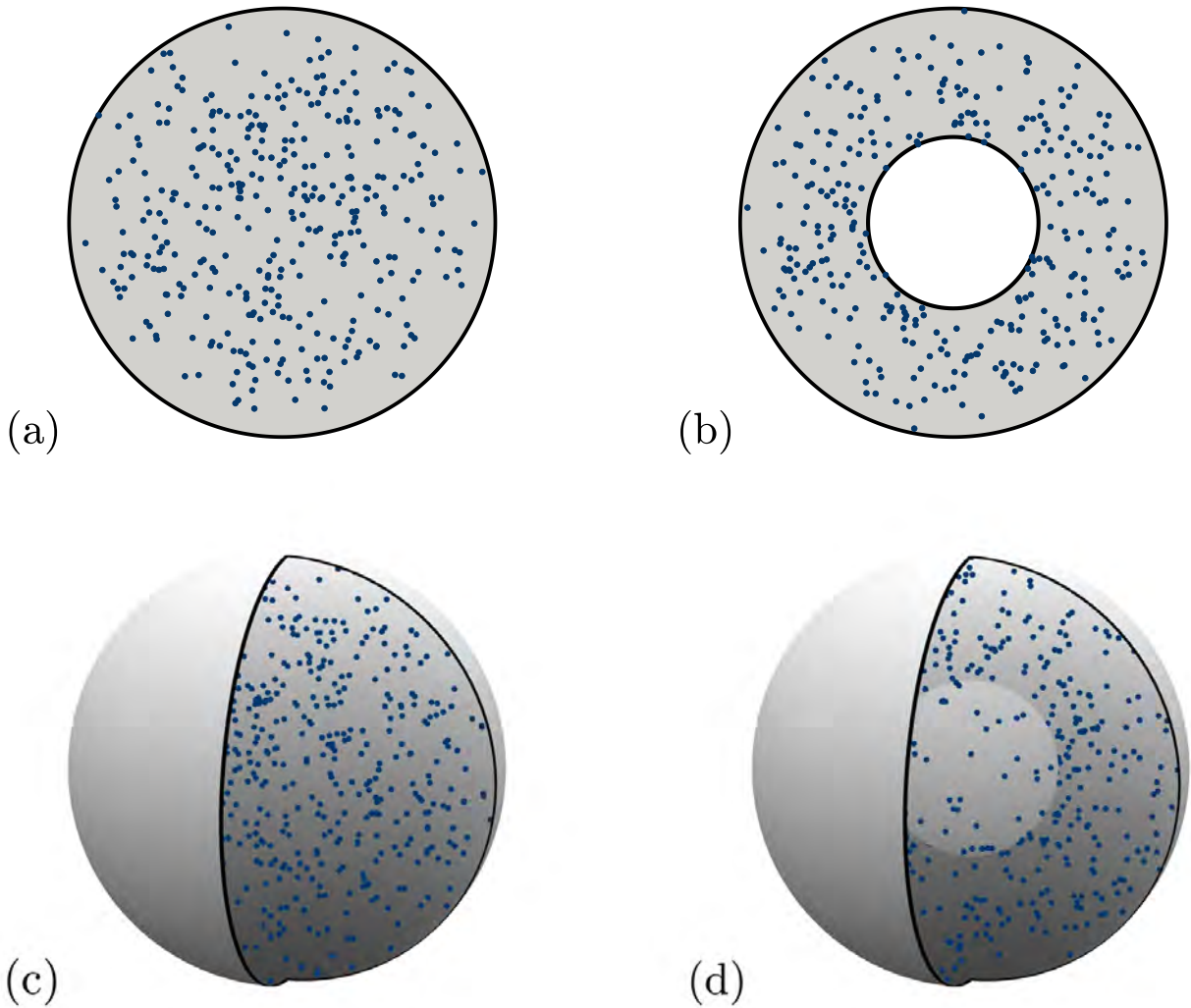


Figure 1.1: Diffusion-controlled release of particles from homogeneous (a) circular, (b) annular, (c) spherical and (d) spherical shell geometries. Here, particles are initially uniformly distributed and diffuse until they are absorbed at a boundary (see section 2.2).

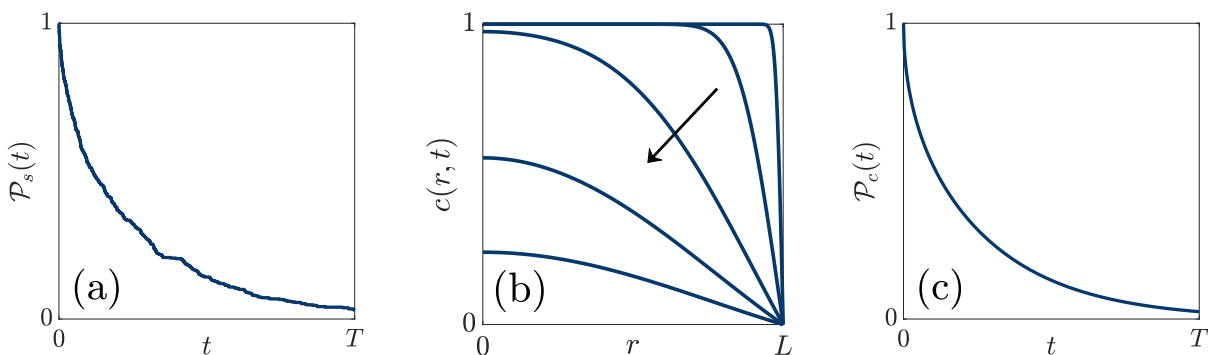


Figure 1.2: Stochastic and continuum models of particle release from a homogeneous annular geometry with a fixed radius L , reflecting inner boundary and absorbing outer boundary. (a) stochastic analogue of $\mathcal{P}(t)$, denoted as $\mathcal{P}_s(t)$, obtained from a single simulation of the random walk model (see section 2.2). (b) dimensionless particle concentration $c(r, t)$ obtained by solving the continuum analogue of the stochastic diffusion model (see section 2.3), where the arrow indicates the direction of increasing time. (c) continuum description of $\mathcal{P}(t)$, denoted as $\mathcal{P}_c(t)$, obtained by calculating the spatial average of $c(r, t)$ (see section 2.3).

numerical calculations (see section 3.1). This complexity obscures the precise influence of each physical parameter on $\mathcal{P}(t)$ and complicates the fitting of experimental release data [18, 22]. To address these issues, we develop surrogate models that provide simple closed-form analytical approximations of $\mathcal{P}(t)$ [24]. In comparison to the stochastic and continuum approaches, these models are computationally inexpensive to compute and provide meaningful analytical insight into the effect of key physical parameters on $\mathcal{P}(t)$.

1.1.1 Application to drug delivery and food drying

Surrogate models are utilised in numerous disciplines, including in the design and optimisation of drug delivery capsules [12, 25]. Typically, surrogate models within this scope are developed to describe the normalised drug mass released or remaining over time, which is a quantity analogous to $\mathcal{P}(t)$ [12, 17, 22, 23, 26, 27]. In general, mathematical models of drug release can provide meaningful insight into the effect of physical parameters, such as the radius, geometry, diffusivity and boundary conditions, on the drug release profile. The physical properties of a device can then be optimised to achieve a desired release profile while reducing experimental testing [22, 23, 26, 28]. The most influential mechanism in controlling drug release rates is diffusion, among other effects such as device erosion [23, 26, 29, 30]. In the literature, significant research has been presented on modelling diffusion-controlled drug release from single or multi-layered spherical microcapsules [25, 28, 29, 31] and other radially-symmetric devices [11, 12, 22, 23, 32–34]. The benefits include potential enhancement of disease treatment effectiveness [17], improvements in the safety and efficacy of drug delivery [11] and greater control over release rates and duration for drug absorption into the blood or tissues [27, 35, 36].

Moreover, surrogate models are frequently used to obtain insight into the kinetics of drying processes for thin slices of fruits or vegetables. A mathematical understanding of the moisture release, controlled by diffusion [37], that occurs during the drying of thin-layered agricultural products is critical for the improvement and optimisation of drying environment design and product quality [38, 39], while avoiding extensive experimentation [40]. In other words, a purely experimental approach to food drying that disregards a mathematical interpretation of drying kinetics can have a negative impact on drying efficiency and the cost of production [39]. Many simple surrogate models have been developed to describe the average moisture content, analogous to $\mathcal{P}(t)$, of a thin-layered product over time subject to different drying conditions [39, 41, 42].

1.1.2 Surrogate models

Surrogate models describing $\mathcal{P}(t)$ and analogous quantities can typically be separated into three distinct categories: theoretical, semi-theoretical and empirical [41, 43]. The most common theoretical model is Fick’s second law of diffusion (see section 2.3) [39, 41, 42, 44]. However, as previously discussed, this model yields infinite series solutions which obscure the precise influence of each physical parameter on the release profile [18, 22]. Rather, the most widely

applied surrogate models are semi-theoretical and empirical [39, 45]. However, the primary issue associated with empirical models is their sole reliance on experimental data and statistical methods to estimate the model parameters [18, 27, 46]. Although these models provide a good fit with data, there is limited potential for useful analytical insight into the mass transfer process [25, 45, 46] as the parameters have no physical meaning [41, 42].

Semi-theoretical models can be considered as a compromise between theoretical and empirical models [47] and are of primary interest in this thesis. These models have the potential to provide meaningful analytical insight into the precise influence of physical parameters on $\mathcal{P}(t)$. In the literature, exponential, Weibull and other exponential-like functions are commonly utilised as surrogate models for $\mathcal{P}(t)$ and related quantities [48, 49]. These models are generally derived by simplifying the infinite series solutions of Fick's second law or using Newton's law of cooling [39, 41, 42, 46]. In drug delivery literature, previous work includes surrogate models for homogeneous slab, circular and spherical geometries with radial symmetry [12, 18, 22, 23, 26, 33, 50]. Moreover, there exist several semi-theoretical surrogate models for the average moisture ratio in food drying applications, as summarised by Akpinar [41], Ertekin et al. [42] and Onwude et al. [39]. Examples include exponential models for the drying of strawberry [51], mushroom [43] and pumpkin [52], Weibull models for quince drying [53], and other exponential-like models for the drying of banana [54] and chickpea [55].

Recently, Carr [18] presented several one-term exponential and Weibull models for $\mathcal{P}(t)$ obtained by matching moments² with the continuum analogue (see section 2.3) of the stochastic diffusion model (see section 2.2) for $\mathcal{P}(t)$. The work considers homogeneous slab, circular, annular, spherical and spherical shell geometries. The moment-matching approach is attractive as it captures key temporal behaviour of $\mathcal{P}(t)$ yields relatively simple closed-form expressions that depend explicitly on known physical parameters of the system, including the radius, diffusivity, dimension and boundary conditions. Hence, meaningful analytical insight into the influence of key physical parameters on $\mathcal{P}(t)$ is able to be obtained. This approach is inspired by previous work which shows that simple closed-form expressions can be obtained for the temporal moments of particle exit time for homogeneous and heterogeneous radially-symmetric geometries [56, 57]. The main drawback of the one-term exponential model is that it tends to overestimate the early decay, and underestimate the later stages of decay, of $\mathcal{P}(t)$ [42]. Moreover, the one-term Weibull model offers a more accurate description of $\mathcal{P}(t)$, but sacrifices model simplicity and reduces meaningful analytical insight by introducing approximations for model parameters. Additionally, the surrogate models are developed under the assumption of a constant diffusivity. However, surrogate models have the potential to provide meaningful analytical insight into the influence of heterogeneous diffusion on the release profile. This is particularly important in drug delivery applications, where multi-layered spherical capsules are designed to give greater control over the drug release rate [17, 25, 56].

²Strictly speaking, the term ‘matching moments’ in this thesis refers to matching *temporal* moments with the continuum analogue of $\mathcal{P}(t)$, not *spatial* moments.

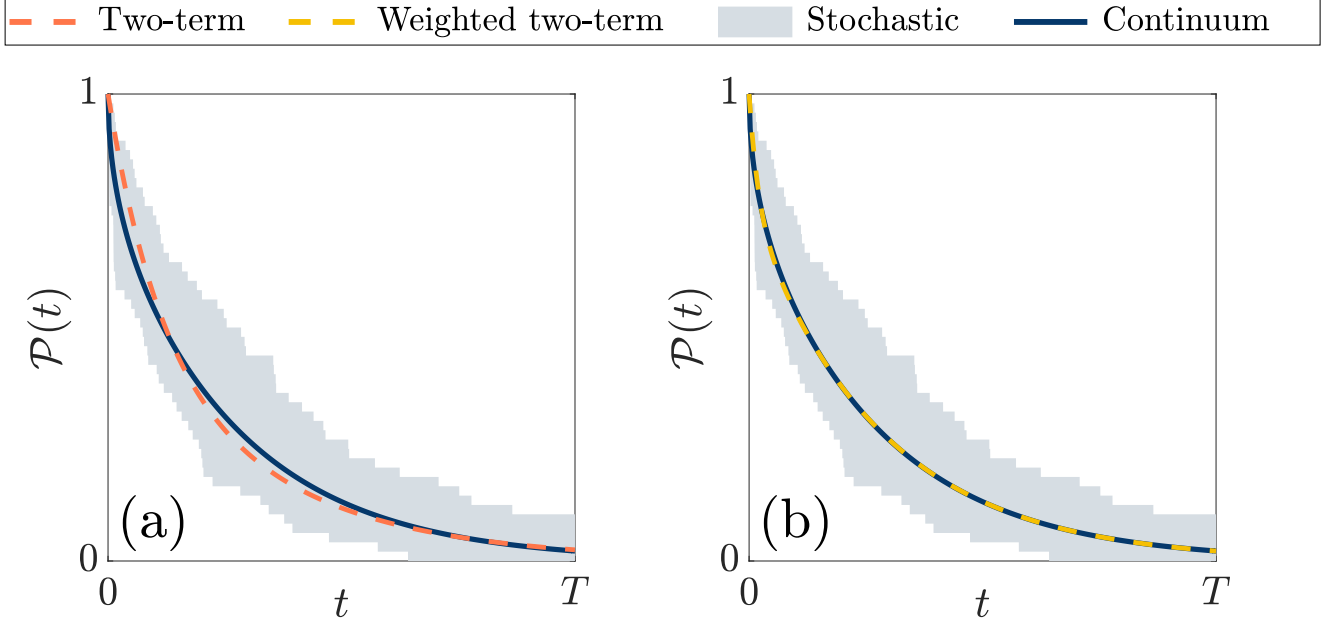


Figure 1.3: Stochastic and continuum values for the proportion of particles remaining over time, $\mathcal{P}(t)$, compared with example (a) two-term and (b) weighted two-term exponential models (see sections 2.4.3–2.4.5). Here, particles are released from a homogeneous annular geometry with a reflecting inner boundary and absorbing outer boundary.

1.1.3 Thesis contributions

In this thesis, motivated by Carr [18] and models in the thin-layer drying literature [39, 41, 42], we develop two-term and weighted two-term exponential models for $\mathcal{P}(t)$ (Fig. 1.3). These novel surrogate models accurately capture the early and late-time decay of $\mathcal{P}(t)$ for a collection of test cases and are simpler in construction than the one-term Weibull model of Carr [18]. We assume that $\mathcal{P}(t)$ takes a functional form with parameters determined by matching moments with the continuum analogue (see section 2.3) of the stochastic diffusion model (see section 2.2). First, we reproduce the work of Carr [18] and present one-term models for $\mathcal{P}(t)$ obtained by matching the zeroth moment with the continuum analogue (see section 2.4.3). Secondly, we develop two-term models for $\mathcal{P}(t)$ by matching the zeroth and first moments with the continuum analogue (see section 2.4.4). Thirdly, we explore weighted two-term models for $\mathcal{P}(t)$ by matching the zeroth, first and second moments with the continuum analogue (see section 2.4.5). In this work, we consider three distinct cases: (i) homogeneous slab, circular and spherical geometries, (ii) homogeneous slab, annular or spherical shell geometries and (iii) heterogeneous slab, circular and spherical geometries. Here, the heterogeneous geometries are comprised of two distinct homogeneous layers.

1.2 Objectives and structure

There are two main research objectives that motivate this thesis:

1. Develop novel accurate surrogate models for diffusion-controlled release from homoge-

neous radially-symmetric geometries.

2. Develop novel accurate surrogate models for diffusion-controlled release from heterogeneous radially-symmetric geometries.

The main body of this thesis is comprised of a publication (chapter 2) and supporting information (chapter 3). In chapter 2, we present the manuscript published in *Physica A* (July 2023) which addresses both objectives. This chapter provides several novel surrogate models for diffusion-controlled release from radially-symmetric geometries. We consider three different types of boundary conditions and develop surrogate models for seven distinct cases. The first five cases pertain to homogeneous geometries and the later two are for heterogeneous geometries. Finally, the surrogate models, for two-dimensional radially-symmetric geometries, are compared to stochastic and continuum values for $\mathcal{P}(t)$ for seven test cases. The published manuscript is available online (<https://doi.org/10.1016/j.physa.2023.129067>) and code implementing the stochastic, continuum and surrogate models and reproducing the results of the paper is available on GitHub (https://github.com/lukefilippini/Filippini_2023.git). Additionally, the candidate has also disseminated the work presented in chapter 2 on several occasions:

1. QANZIAM Conference (Brisbane, July 2022)
2. CTAC (Brisbane, Nov-Dec 2022)
3. AMSI Summer School (Melbourne, Jan 2023) [Best presentation prize winner]
4. ANZIAM (Cairns, Feb 2023)

Chapter 3 includes supporting details on project conceptualisation, methodology and results that were not included in the submitted manuscript. Firstly, we discuss in greater detail exact solutions of the continuum analogue of $\mathcal{P}(t)$ and the limitations associated with this approach. Secondly, we provide a detailed derivation of the three general surrogate models and consider solutions for three specific cases. Thirdly, we outline the finite volume and time-stepping schemes used to compute numerical solutions of the continuum model for homogeneous and heterogeneous geometries. Additionally, we present comparisons, for one- and three-dimensional radially-symmetric geometries, between the surrogate models and stochastic and continuum values for $\mathcal{P}(t)$. We consider the same seven test cases as in chapter 2. Finally, we discuss additional project ideas that we were discontinued but could potentially be explored as future work.

In Chapter 4, we summarise the key aspects and findings of the thesis and discuss avenues for potential future research in this area.

Statement of Contribution of Co-Authors

Chapter 2 consists of the following published paper:

Luke P. Filippini, Matthew J. Simpson and Elliot J. Carr. (2023). Simplified models of diffusion in radially-symmetric geometries. *Physica A: Statistical Mechanics and its Applications*, 626, 129067. doi: [10.1016/j.physa.2023.129067](https://doi.org/10.1016/j.physa.2023.129067)

The authors listed below have certified that:

1. they meet the criteria for authorship and that they have participated in the conception, execution, or interpretation, of at least that part of the publication in their field of expertise;
2. they take public responsibility for their part of the publication, except for the responsible author who accepts overall responsibility for the publication;
3. there are no other authors of the publication according to these criteria;
4. potential conflicts of interest have been disclosed to (a) granting bodies, (b) the editor or publisher of journals or other publications, and (c) the head of the responsible academic unit, and
5. they agree to the use of the publication in the student's thesis and its publication on the QUT's ePrints site consistent with any limitations set by publisher requirements.

Publication title: Simplified models of diffusion in radially-symmetric geometries

Publication status: Published in *Physica A*

Contributor	Statement of contribution
Luke Filippini	developed the surrogate models, implemented the stochastic and continuum models, performed all stochastic and numerical simulations, generated the figures, analysed the results, drafted the manuscript
Elliot Carr	conceptualised the research project, supervised the development and implementation of all models, guided model simulations, assisted with figure generation, assisted with surrogate model analysis, critically reviewed and edited the manuscript
Matthew Simpson	supervised the development and implementation of all models, guided model simulations, assisted with surrogate model analysis, assisted with figure generation, critically reviewed the manuscript

Chapter 2

Simplified models of diffusion in radially-symmetric geometries

2.1 Introduction

Mathematical modelling of diffusion-controlled transport is applied across many disciplines, including biology [3, 4, 58], ecology [4], medicine [12, 26, 27] and physics [10, 59]. Important applications include drug delivery from cylindrical [11, 23] and spherical [23, 25–27, 29] devices and the drying of fruit and vegetable products [38, 39, 43, 60]. Motivated by such applications, in this paper, we explore diffusion-controlled release from d -dimensional radially-symmetric geometries (Fig. 2.1(a)). Here, particles diffuse within the geometry until they are absorbed at a boundary (Fig. 2.1(b)). A key quantity commonly used to characterise such diffusion processes is the proportion of particles remaining within the geometry over time, denoted as $\mathcal{P}(t)$. This quantity is equivalent to the survival probability [20, 21] of an arbitrary particle and decreases over time as the number of absorbed particles increases. The shape and slope of $\mathcal{P}(t)$ (Fig. 2.1(d)) is influenced by key parameters such as the dimension, diffusivity, geometry and boundary conditions of the diffusive transport system [18].

Traditionally, $\mathcal{P}(t)$ is calculated using a stochastic or continuum approach. In the stochastic approach, computing $\mathcal{P}(t)$ involves repeated simulations of a random walk model governing the motion of each individual particle. In the continuum approach, computing $\mathcal{P}(t)$ involves solving the continuum analogue of the stochastic model for the particle concentration (Fig. 2.1(c)). Both of these approaches have their drawbacks. Firstly, the stochastic approach is time-consuming and lacks analytical insight into key parameters. Secondly, the continuum approach yields complicated expressions for $\mathcal{P}(t)$ [22, 23] that obscure the influence of key parameters and complicate the process of fitting experimental release data [18, 22]. To address these issues, surrogate modelling aims to develop a simplified model that accurately approximates $\mathcal{P}(t)$ and is computationally inexpensive (Fig. 2.1(d)). Previous work includes exponential, Weibull and other exponential-like models for $\mathcal{P}(t)$ and related quantities [48, 49] for slab, circular, and spherical geometries with radial symmetry [19, 22, 23, 26, 27, 39, 58].

In this paper, we develop several new accurate surrogate models for $\mathcal{P}(t)$ by matching mo-

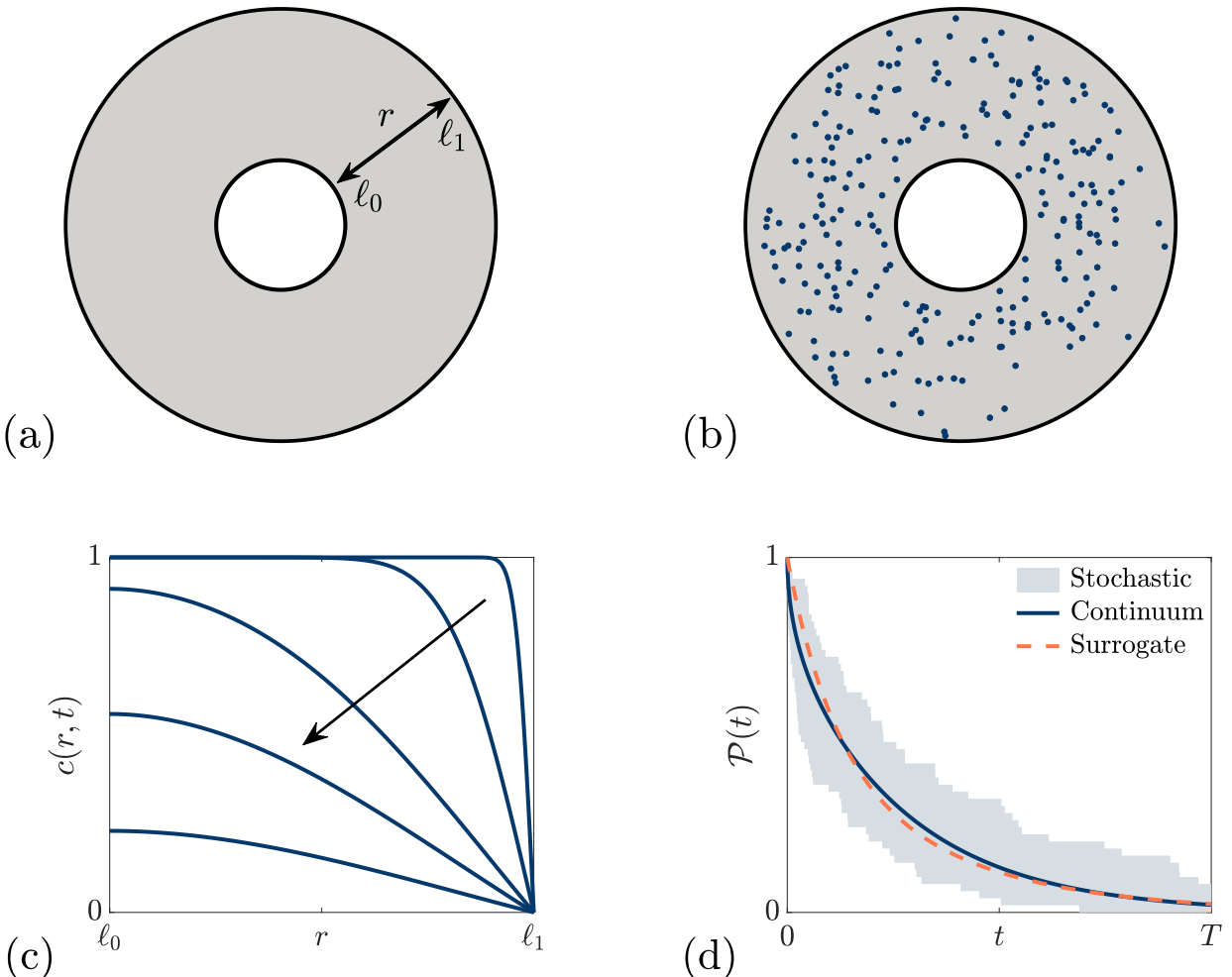


Figure 2.1: (a)–(b) Diffusion-controlled release of particles from a homogeneous annular geometry with a reflecting inner boundary and absorbing outer boundary. Here, particles diffuse until they are absorbed out of the system (see section 2.2). (c) dimesionless particle concentration $c(r,t)$ obtained by solving the continuum analogue of the stochastic diffusion model (see section 2.3) with the arrow indicating the direction of increasing time. (d) stochastic and continuum calculations for the proportion of particles remaining over time, $\mathcal{P}(t)$, with an example surrogate model (see sections 2.4.3–2.4.5) providing a simple accurate approximation to $\mathcal{P}(t)$.

ments with the continuum analogue of the stochastic diffusion model. This approach yields surrogate models that explicitly depend on, and provide analytical insight into, key parameters of the diffusive transport system. Firstly, we revisit the work of Carr [18] and present one-term exponential models to approximate $\mathcal{P}(t)$, obtained by matching the zeroth moments. Secondly, we present new two-term exponential models to approximate $\mathcal{P}(t)$, obtained by matching the zeroth and first moments. Finally, we present new weighted two-term exponential models involving an arbitrary weighting of the two exponential terms, obtained by matching the zeroth, first and second moments. Our scope includes both homogeneous geometries with a constant particle movement probability and heterogeneous geometries comprised of two concentric layers with different particle movement probabilities. In addition to standard absorbing and reflecting boundary conditions, we also consider semi-absorbing boundary conditions, where particles are

either absorbed or reflected with specified probabilities. Both semi-absorbing boundaries and heterogeneous geometries find application to drug delivery applications, where heterogeneous multi-layer spherical capsules encapsulated with semi-absorbing permeable outer shells are designed to better control the drug release rate [17, 25, 29]. In total, we present new surrogate models for three main problems: (i) homogeneous slab, circular and spherical geometries with an absorbing or semi-absorbing boundary, (ii) homogeneous slab, annular and spherical shell geometries with absorbing, reflecting and/or semi-absorbing boundaries and (iii) heterogeneous slab, circular and spherical geometries with an absorbing or semi-absorbing boundary. Each model is easy to evaluate, agrees well with both stochastic and continuum calculations of $\mathcal{P}(t)$ and provides analytical insight into the physical parameters of the diffusive transport system: dimension, diffusivity, geometry and boundary conditions.

The remaining sections of this work is structured as follows. Firstly, we discuss the stochastic (section 2.2) and continuum (section 2.3) models and outline how $\mathcal{P}(t)$ is calculated in each case. Secondly, we develop the new one-term (section 2.4.3), two-term (section 2.4.4) and weighted two-term (section 2.4.5) surrogate models for $P(t)$. Thirdly, we assess the accuracy of the surrogate models against $\mathcal{P}(t)$ obtained from the stochastic and continuum models (section 2.5). Finally, we summarise the main elements of the work and suggest avenues for future research (section 2.6).

2.2 Stochastic model

We now describe the stochastic approach for calculating $\mathcal{P}(t)$ using a random walk model for diffusive transport in d -dimensional radially-symmetry geometries. We consider both a homogeneous geometry ($\ell_0 < r < \ell_1$) with constant particle movement probability, P , and a heterogeneous geometry ($\ell_0 < r < \ell_2$) comprised of two concentric layers ($\ell_0 < r < \ell_1$ and $\ell_1 < r < \ell_2$) with different movement probabilities, P_1 and P_2 . Our analysis allows for slab geometries with both an inner (left) and outer (right) boundary, circular/spherical geometries ($\ell_0 = 0$) with an outer boundary only and annular/spherical-shell geometries ($\ell_0 > 0$) with both an inner and outer boundary.

Consider N_p non-interacting particles and let $\mathbf{x}_j(t)$ denote the position of the j th particle at time t . Initially, the particles are uniformly distributed across the geometry:

$$\mathbf{x}_j(0) = \begin{cases} r_j, & \text{if } d = 1, \\ r_j[\cos(\theta_j), \sin(\theta_j)], & \text{if } d = 2, \\ r_j[\cos(\theta_j)\sin(\phi_j), \sin(\theta_j)\sin(\phi_j), \cos(\phi_j)], & \text{if } d = 3, \end{cases} \quad (2.1)$$

where $r_j = (\ell_m^d + u_j(\ell_m^d - \ell_0^d))^{1/d}$ ($m = 1$ for homogeneous geometry and $m = 2$ for heterogeneous geometry), $\phi_j = \cos^{-1}(1 - 2v_j)$, $\theta_j \sim \mathcal{U}(0, 2\pi)$, $u_j \sim \mathcal{U}(0, 1)$ and $v_j \sim \mathcal{U}(0, 1)$ [18]. Thereafter, each particle participates in a random walk with constants steps of distance $\delta > 0$ and duration $\tau > 0$, where during each time step, each particle undergoes a movement or rest event with

probabilities depending on the geometry under consideration.

2.2.1 Homogeneous geometry

For a homogeneous geometry, the j th particle moves to a new position

$$\mathbf{x}_j(t + \tau) = \mathbf{x}_j(t) + \begin{cases} \delta \operatorname{sign}(u_j - 0.5), & \text{if } d = 1, \\ \delta[\cos(\theta_j), \sin(\theta_j)], & \text{if } d = 2, \\ \delta[\cos(\theta_j) \sin(\phi_j), \sin(\theta_j) \sin(\phi_j), \cos(\phi_j)], & \text{if } d = 3, \end{cases} \quad (2.2)$$

with probability P , or remains at its current position, implying $\mathbf{x}_j(t + \tau) = \mathbf{x}_j(t)$, with probability $1 - P$. Here, $\phi_j = \cos^{-1}(1 - 2v_j)$, $\theta_j \sim \mathcal{U}(0, 2\pi)$, $u_j \sim \mathcal{U}(0, 1)$ and $v_j \sim \mathcal{U}(0, 1)$.

2.2.2 Heterogeneous geometry

For a heterogeneous geometry, we follow [57], where the j th particle undergoes a movement or rest event depending on the possible new movement positions described by $\mathcal{S}_d(\mathbf{x}_j(t); \delta)$, the line ($d = 1$), circle ($d = 2$) or sphere ($d = 3$) of radius δ centred on $\mathbf{x}_j(t)$. During each time step, there are three possibilities.

1. If $\mathcal{S}_d(\mathbf{x}_j(t); \delta)$ does not intersect the interface ($r = \ell_1$) and $\mathbf{x}_j(t)$ is located in the inner layer ($\ell_0 < r < \ell_1$), then the j th particle moves to a new position (2.2) with probability P_1 or remains at its current position with probability $1 - P_1$.
2. If $\mathcal{S}_d(\mathbf{x}_j(t); \delta)$ does not intersect the interface ($r = \ell_1$) and $\mathbf{x}_j(t)$ is located in the outer layer ($\ell_1 < r < \ell_2$) then the j th particle moves to a new position (2.2) with probability P_2 or remains at its current position with probability $1 - P_2$.
3. If $\mathcal{S}_d(\mathbf{x}_j(t); \delta)$ intersects the interface $r = \ell_1$, then the j th particle moves to a new position or remains at its current position with probabilities depending on the dimension d . For $d = 1$, the j th particle moves to a new position

$$\mathbf{x}_j(t + \tau) = \mathbf{x}_j(t) + \begin{cases} -\delta, & \text{with probability } \mathcal{P}_1/2, \\ \delta, & \text{with probability } \mathcal{P}_2/2, \end{cases}$$

or remains at its current position with probability $1 - \mathcal{P}_1/2 - \mathcal{P}_2/2$. Here, \mathcal{P}_k is the probability associated with the layer in which the position $\mathbf{x}_j(t) + \delta/2(-1)^k$ is located. For $d = 2$, the j th particle moves to a new position

$$\mathbf{x}_j(t + \tau) = \mathbf{x}_j(t) + \begin{cases} \delta[\cos(\theta_1), \sin(\theta_1)], & \text{with probability } \mathcal{P}_1/n, \\ \delta[\cos(\theta_2), \sin(\theta_2)], & \text{with probability } \mathcal{P}_2/n, \\ \vdots & \vdots \\ \delta[\cos(\theta_n), \sin(\theta_n)], & \text{with probability } \mathcal{P}_n/n, \end{cases}$$

or remains at its current position with probability $1 - \sum_{k=1}^n \mathcal{P}_k/n$. Here, n is a specified integer (see section 2.5), $\theta_k = 2\pi(k-1)/n$ and \mathcal{P}_k is the probability associated with the layer in which the position $\mathbf{x}_j(t) + \delta/2[\cos(\theta_k), \sin(\theta_k)]$ is located [57]. For $d = 3$, the j th particle moves to a new position

$$\mathbf{x}_j(t + \tau) = \mathbf{x}_j(t) + \begin{cases} \delta[\cos(\theta_1) \sin(\phi_1), \sin(\theta_1) \sin(\phi_1), \cos(\phi_1)], & \text{with probability } \mathcal{P}_{1,1}/n, \\ \delta[\cos(\theta_1) \sin(\phi_2), \sin(\theta_1) \sin(\phi_2), \cos(\phi_2)], & \text{with probability } \mathcal{P}_{1,2}/n, \\ \vdots & \vdots \\ \delta[\cos(\theta_1) \sin(\phi_{n_2}), \sin(\theta_1) \sin(\phi_{n_2}), \cos(\phi_{n_2})], & \text{with probability } \mathcal{P}_{1,n_2}/n, \\ \delta[\cos(\theta_2) \sin(\phi_1), \sin(\theta_2) \sin(\phi_1), \cos(\phi_1)], & \text{with probability } \mathcal{P}_{2,1}/n, \\ \vdots & \vdots \\ \delta[\cos(\theta_{n_1}) \sin(\phi_{n_2}), \sin(\theta_{n_1}) \sin(\phi_{n_2}), \cos(\phi_{n_2})], & \text{with probability } \mathcal{P}_{n_1,n_2}/n, \end{cases}$$

or remains at its current position with probability $1 - \sum_{k=1}^{n_1} \sum_{m=1}^{n_2} \mathcal{P}_{k,m}/n$, where $n = n_1 n_2$. Here, n_1 and n_2 are specified integers (see section 2.5), $\theta_k = 2\pi(k-1)/n_1$, $\phi_m = \cos^{-1}(1 - 2(m-1)/n_2)$ and $\mathcal{P}_{k,m}$ is the probability associated with the layer in which the position $\mathbf{x}_j(t) + \delta/2 [\cos(\theta_k) \sin(\phi_m), \cos(\theta_k) \sin(\phi_m), \cos(\phi_m)]$ is located [57].

2.2.3 Boundary conditions

In our stochastic model, boundaries are designated as absorbing, reflecting or semi-absorbing. If a particle attempts to pass through an absorbing boundary, it is removed from the system, whereas, if it attempts to pass through a reflecting boundary, it is returned to its previous position, implying $\mathbf{x}_j(t+\tau) = \mathbf{x}_j(t)$. On the other hand, if a particle attempts to pass through a semi-absorbing inner boundary, it is absorbed with probability P_I and reflected with probability $1 - P_I$, while if a particle attempts to pass through a semi-absorbing outer boundary, it is absorbed with probability P_O and reflected with probability $1 - P_O$ [18, 61].

2.2.4 Calculation of $\mathcal{P}(t)$

For the stochastic model, $\mathcal{P}(t)$ is defined as [17]

$$\mathcal{P}_s(t) = \frac{N(t)}{N_p}, \quad (2.3)$$

where $N(t)$ is the number of particles in the system at time t .

2.3 Continuum model

We now describe the continuum approach for calculating $\mathcal{P}(t)$ using the continuum analogue of the stochastic model. For both the homogeneous and heterogeneous geometries, the contin-

uum model takes the form of an initial-boundary value problem for the dimensionless particle concentration, $c(r, t)$, and is a valid approximation of the stochastic model in the regime of small δ and τ [3, 4].

2.3.1 Homogeneous geometry

For the homogeneous geometry, $c(r, t)$ satisfies the d -dimensional radially-symmetric diffusion equation [4, 20, 22, 31, 44, 59],

$$\frac{\partial c}{\partial t} = \frac{D}{r^{d-1}} \frac{\partial}{\partial r} \left(r^{d-1} \frac{\partial c}{\partial r} \right), \quad \ell_0 < r < \ell_1, \quad t > 0, \quad (2.4)$$

subject to the initial and boundary conditions,

$$c(r, 0) = 1, \quad \ell_0 \leq r \leq \ell_1, \quad (2.5)$$

$$a_0 c(\ell_0, t) - b_0 \frac{\partial c}{\partial r}(\ell_0, t) = 0, \quad t > 0, \quad (2.6)$$

$$a_1 c(\ell_1, t) + b_1 \frac{\partial c}{\partial r}(\ell_1, t) = 0, \quad t > 0, \quad (2.7)$$

where $D = P\delta^2/(2d\tau)$ is the diffusivity. Note that $c(r, t) = \tilde{c}(r, t)/\tilde{c}_0$, where the particle concentration $\tilde{c}(r, t)$ is initially uniform, $\tilde{c}(r, 0) = \tilde{c}_0$. Here, $\tilde{c}(r, t)$ and \tilde{c}_0 are dimensional quantities that represent the number of particles and initial number of particles per unit length/area/volume [18].

2.3.2 Heterogeneous geometry

For the heterogeneous geometry, the dimensionless particle concentration is a piecewise function

$$c(r, t) = \begin{cases} c_1(r, t), & \ell_0 \leq r \leq \ell_1, \\ c_2(r, t), & \ell_1 \leq r \leq \ell_2, \end{cases}$$

where $c_1(r, t)$ and $c_2(r, t)$ satisfy the d -dimensional radially-symmetric diffusion equation in the inner and outer layers respectively [25, 29, 62, 63]

$$\frac{\partial c_1}{\partial t} = \frac{D_1}{r^{d-1}} \frac{\partial}{\partial r} \left(r^{d-1} \frac{\partial c_1}{\partial r} \right), \quad \ell_0 < r < \ell_1, \quad t > 0, \quad (2.8)$$

$$\frac{\partial c_2}{\partial t} = \frac{D_2}{r^{d-1}} \frac{\partial}{\partial r} \left(r^{d-1} \frac{\partial c_2}{\partial r} \right), \quad \ell_1 < r < \ell_2, \quad t > 0, \quad (2.9)$$

subject to the initial, boundary and interface conditions,

$$c_1(r, 0) = 1, \quad \ell_0 \leq r \leq \ell_1, \quad c_2(r, 0) = 1, \quad \ell_1 \leq r \leq \ell_2, \quad (2.10)$$

$$a_0 c_1(\ell_0, t) - b_0 \frac{\partial c_1}{\partial r}(\ell_0, t) = 0, \quad t > 0, \quad (2.11)$$

$$a_1 c_2(\ell_2, t) + b_1 \frac{\partial c_2}{\partial r}(\ell_2, t) = 0, \quad t > 0, \quad (2.12)$$

$$c_1(\ell_1, t) = c_2(\ell_1, t), \quad t > 0, \quad (2.13)$$

$$D_1 \frac{\partial c_1}{\partial r}(\ell_1, t) = D_2 \frac{\partial c_2}{\partial r}(\ell_1, t), \quad t > 0. \quad (2.14)$$

Here, $D_1 = P_1 \delta^2 / (2d\tau)$ and $D_2 = P_2 \delta^2 / (2d\tau)$ are the diffusivities for the inner and outer layers, respectively. The interface conditions (2.13) and (2.14) specify continuity of concentration and flux at the interface, which assumes perfect contact between the layers [62, 63]. Note that $c_1(r, t) = \tilde{c}_1(r, t)/\tilde{c}_0$ and $c_2(r, t) = \tilde{c}_2(r, t)/\tilde{c}_0$, where the quantities $\tilde{c}_1(r, t)$ and $\tilde{c}_2(r, t)$ represent the number of particles per unit length/area/volume in the inner and outer layers, respectively.

2.3.3 Boundary conditions

The coefficients in the boundary conditions (2.6)–(2.7) and (2.11)–(2.12) depend on whether the boundaries are absorbing, reflecting or semi-absorbing:

$$[a_0, b_0] = \begin{cases} [1, 0], & \text{if the inner boundary is absorbing,} \\ [0, 1], & \text{if the inner boundary is reflecting,} \\ [1, \beta_0], & \text{if the inner boundary is semi-absorbing,} \end{cases} \quad (2.15)$$

$$[a_1, b_1] = \begin{cases} [1, 0], & \text{if the outer boundary is absorbing,} \\ [0, 1], & \text{if the outer boundary is reflecting,} \\ [1, \beta_1], & \text{if the outer boundary is semi-absorbing,} \end{cases} \quad (2.16)$$

with $\beta_0 = \delta/P_I$ and $\beta_1 = \delta/P_O$ [18]. Note that for the case of the circular or spherical geometry with no inner boundary ($\ell_0 = 0$), we set $[a_0, b_0] = [0, 1]$ for radial symmetry at the origin.

2.3.4 Calculation of $\mathcal{P}(t)$

For both the homogeneous continuum model (2.4)–(2.7) and the heterogeneous continuum model (2.8)–(2.14), $\mathcal{P}(t)$ is defined as [18, 19]

$$\mathcal{P}_c(t) = \frac{\int_{\Omega_d} c(r, t) dV}{\int_{\Omega_d} c(r, 0) dV},$$

where $\Omega_1 = \{\mathbf{x} \in \mathbb{R} \mid \ell_0 < x < \ell_m\}$ and $\Omega_d = \{\mathbf{x} \in \mathbb{R}^d \mid \ell_0 < \|\mathbf{x}\|_2 < \ell_m\}$ for $d = 2, 3$ ($m = 1$ for homogeneous geometry and $m = 2$ for heterogeneous geometry). Using radial symmetry and

the constant initial conditions (2.5) and (2.10), $\mathcal{P}_c(t)$ simplifies to [18, 19]:

$$\mathcal{P}_c(t) = \frac{d}{\ell_1^d - \ell_0^d} \int_{\ell_0}^{\ell_1} r^{d-1} c(r, t) dr, \quad (2.17)$$

$$\mathcal{P}_c(t) = \frac{d}{\ell_2^d - \ell_0^d} \left[\int_{\ell_0}^{\ell_1} r^{d-1} c_1(r, t) dr + \int_{\ell_1}^{\ell_2} r^{d-1} c_2(r, t) dr \right], \quad (2.18)$$

for the homogeneous and heterogeneous geometries, respectively.

Clearly, calculating $\mathcal{P}_c(t)$ requires solving the homogeneous continuum model (2.4)–(2.7) and heterogeneous continuum model (2.8)–(2.14). Alternatively, one may think of applying the averaging operators (2.17) or (2.18) to the homogeneous or heterogeneous continuum model to derive an initial value problem for $\mathcal{P}_c(t)$. Unfortunately, this initial value problem involves $c(r, t)$ itself except for the special case of reflecting boundary conditions, where trivially, $\mathcal{P}_c(t) = 1$ for all time as no particles exit the system [18] (see section 3.1.3).

2.4 Surrogate models

2.4.1 Motivation

Exact expressions for $\mathcal{P}_c(t)$ can be obtained by solving the homogeneous continuum model (2.4)–(2.7) or heterogeneous continuum model (2.8)–(2.14) using separation of variables [25, 62, 63] and then averaging the solution by applying (2.17) or (2.18) (see section 3.1.1). For example, for the case of a homogeneous disc ($d = 2$) with $\ell_0 = 0$, $\ell_1 = L$, radial symmetry at the origin ($[a_0, b_0] = [0, 1]$) and a semi-absorbing boundary ($[a_1, b_1] = [1, \beta_1]$), we obtain

$$\mathcal{P}_c(t) = \frac{2}{L^2} \sum_{n=1}^{\infty} \frac{[\int_0^L r J_0(\eta_n r) dr]^2}{\int_0^L r J_0(\eta_n r)^2 dr} e^{-\eta_n^2 D t}, \quad (2.19)$$

where η_n for $n \in \mathbb{N}^+$ are the positive roots of the transcendental equation

$$\eta_n \frac{J_1(\eta_n L)}{J_0(\eta_n L)} = \frac{1}{\beta_1}, \quad (2.20)$$

and $J_\nu(\cdot)$ is the Bessel function of the first kind of order ν . The problem, however, is that (2.19) takes the form of an infinite series of exponential terms with complicated coefficients and the values of η_n have to be determined numerically since closed-form expressions for the roots of (2.20) are not able to be determined. Moreover, to achieve sufficient accuracy for small values of time, a large number of terms need to be taken in the series (2.19) (see section 3.1.2). All of these issues complicate both fitting experimental release data and interpreting the effect of known physical parameters, such as L , D and β_1 , on $\mathcal{P}_c(t)$ [18, 22], motivating the need for surrogate modelling [18, 22].

2.4.2 Moments

In this work, we develop surrogate models for $\mathcal{P}(t)$ by matching moments with the continuum model. As we will see later in sections 2.4.3–2.4.5, this process defines surrogate models in terms of spatially-averaged moments of the continuum model. We now outline how exact expressions for these spatially-averaged moments can be calculated for both the homogeneous and heterogeneous continuum models.

Homogeneous geometry

For the homogeneous continuum model (2.4)–(2.7), the k th moment is defined by

$$M_k(r) = \int_0^\infty t^k c(r, t) dt, \quad k = 0, 1, 2, \dots \quad (2.21)$$

Closed-form solutions for $M_k(r)$ can be obtained, without prior calculation of $c(r, t)$, since $M_k(r)$ satisfies the differential equation [56, 57]:

$$\frac{D}{r^{d-1}} \frac{d}{dr} \left(r^{d-1} \frac{dM_k}{dr} \right) = \begin{cases} -1, & k = 0, \\ -kM_{k-1}(r), & k = 1, 2, \dots, \end{cases} \quad (2.22)$$

subject to the boundary conditions,

$$a_0 M_k(\ell_0) - b_0 \frac{dM_k}{dr}(\ell_0) = 0, \quad (2.23)$$

$$a_1 M_k(\ell_1) + b_1 \frac{dM_k}{dr}(\ell_1) = 0. \quad (2.24)$$

Note that this is the same boundary value problem satisfied by the mean particle lifetime for a particle initially located at a distance r from the origin [20, 57]. Given $M_k(r)$, the spatial average of the k th moment is then defined as

$$\langle M_k(r) \rangle = \frac{d}{\ell_1^d - \ell_0^d} \int_{\ell_0}^{\ell_1} r^{d-1} M_k(r) dr. \quad (2.25)$$

Heterogeneous geometry

For the heterogeneous continuum model (2.8)–(2.14), the k th moment is defined by

$$M_k(r) = \begin{cases} M_k^{(1)}(r), & \ell_0 < r < \ell_1, \\ M_k^{(2)}(r), & \ell_1 < r < \ell_2, \end{cases} \quad (2.26)$$

$$M_k^{(1)}(r) = \int_0^\infty t^k c_1(r, t) dt, \quad M_k^{(2)}(r) = \int_0^\infty t^k c_2(r, t) dt. \quad (2.27)$$

Closed-form solutions for $M_k^{(1)}(r)$ and $M_k^{(2)}(r)$ can be obtained without prior calculation of $c_1(r, t)$ and $c_2(r, t)$, since $M_k^{(1)}(r)$ and $M_k^{(2)}(r)$ satisfy the differential equations [56, 57]:

$$\frac{D_1}{r^{d-1}} \frac{d}{dr} \left(r^{d-1} \frac{dM_k^{(1)}}{dr} \right) = \begin{cases} -1, & k = 0, \\ -k M_{k-1}^{(1)}(r), & k = 1, 2, \dots, \end{cases} \quad (2.28)$$

$$\frac{D_2}{r^{d-1}} \frac{d}{dr} \left(r^{d-1} \frac{dM_k^{(2)}}{dr} \right) = \begin{cases} -1, & k = 0, \\ -k M_{k-1}^{(2)}(r), & k = 1, 2, \dots, \end{cases} \quad (2.29)$$

subject to the boundary and interface conditions

$$a_0 M_k^{(1)}(\ell_0) - b_0 \frac{dM_k^{(1)}}{dr}(\ell_0) = 0, \quad (2.30)$$

$$a_1 M_k^{(2)}(\ell_2) + b_1 \frac{dM_k^{(2)}}{dr}(\ell_2) = 0, \quad (2.31)$$

$$M_k^{(1)}(\ell_1) = M_k^{(2)}(\ell_1), \quad (2.32)$$

$$D_1 \frac{dM_k^{(1)}}{dr}(\ell_1) = D_2 \frac{dM_k^{(2)}}{dr}(\ell_1). \quad (2.33)$$

Given $M_k^{(1)}(r)$ and $M_k^{(2)}(r)$, the spatial average of the k th moment is then defined as

$$\langle M_k(r) \rangle = \frac{d}{\ell_2^d - \ell_0^d} \left[\int_{\ell_0}^{\ell_1} r^{d-1} M_k^{(1)}(r) dr + \int_{\ell_1}^{\ell_2} r^{d-1} M_k^{(2)}(r) dr \right]. \quad (2.34)$$

2.4.3 Surrogate model 1: One-term exponential model

We now consider a surrogate model for $\mathcal{P}_c(t)$ consisting of a single exponential term [18],

$$S_1(t) = e^{-\lambda t}, \quad (2.35)$$

where $\lambda > 0$ is a constant which depends on the dimension, diffusivity, geometry and boundary conditions. Note that (2.35) is a sensible candidate model since it agrees with $\mathcal{P}_c(t)$ at initial time ($t = 0$) and has the correct limiting behaviour at large times ($t \rightarrow \infty$) (see, e.g., $\mathcal{P}_c(t)$ in equation (2.19)). To determine λ , we follow [18] and match the zeroth moments of $S_1(t)$ (2.35) and $\mathcal{P}_c(t)$ (2.17),

$$\int_0^\infty S_1(t) dt = \int_0^\infty \mathcal{P}_c(t) dt. \quad (2.36)$$

Substituting $S_1(t)$ (2.35) and $\mathcal{P}_c(t)$ ((2.17) or (2.18)) into equation (2.36), integrating exactly on the left hand side, reversing the order of integration on the right hand side and rearranging yields

$$\lambda = \frac{1}{\langle M_0(r) \rangle}, \quad (2.37)$$

Case	Geometry	Inner Boundary	Outer Boundary	a_0	b_0	a_1	b_1
A	homogeneous	–	absorbing	0	1	1	0
B	homogeneous	–	semi-absorbing	0	1	1	β_1
C	homogeneous	reflecting	absorbing	0	1	1	0
D	homogeneous	reflecting	semi-absorbing	0	1	1	β_1
E	homogeneous	absorbing	absorbing	1	0	1	0
F	heterogeneous	–	absorbing	0	1	1	0
G	heterogeneous	–	semi-absorbing	0	1	1	β_1

Table 2.1: Geometry and boundary parameters for Cases A–G. Note that for Cases A, B, F and G there is no inner boundary ($\ell_0 = 0$), so we set $[a_0, b_0] = [0, 1]$ for radial symmetry at the origin.

where $\langle M_0(r) \rangle$ is defined in section 2.4.2.

We now present several one-term exponential models for $\mathcal{P}(t)$. The models are developed for the seven distinct cases outlined in Table 2.1 involving both homogeneous (Cases A–E) and heterogeneous (Cases F–G) geometries and various combinations of boundary conditions. Each model is presented by providing a closed-form expression for λ appearing in the one-term exponential model (2.35). For the homogeneous geometries, λ is calculated by solving the boundary value problem (2.22)–(2.24) for $M_0(r)$, calculating $\langle M_0(r) \rangle$ (2.25) and then computing λ (2.37). For the heterogeneous geometries, λ is calculated by solving the boundary value problem (2.28)–(2.33) for $M_0^{(1)}(r)$ and $M_0^{(2)}(r)$, calculating $\langle M_0(r) \rangle$ (2.34) and then computing λ (2.37) (see section 3.2.1). For Cases C–E, we note that λ is expressed generally for any dimension d using the definite integral $\int_{\ell_0}^{\ell_1} r^{1-d} dr$, which is equal to $\ell_1 - \ell_0, \ln(\ell_1/\ell_0), 1/\ell_0 - 1/\ell_1$ for $d = 1, 2, 3$, respectively.

Case A: homogeneous slab, circular or spherical geometry ($\ell_0 = 0$ and $\ell_1 = L$) with radial symmetry at the origin ($[a_0, b_0] = [0, 1]$) and an absorbing outer boundary ($[a_1, b_1] = [1, 0]$)

$$\lambda = \frac{d(d+2)D}{L^2}. \quad (2.38)$$

Case B: homogeneous slab, circular or spherical geometry ($\ell_0 = 0$ and $\ell_1 = L$) with radial symmetry at the origin ($[a_0, b_0] = [0, 1]$) and a semi-absorbing outer boundary ($[a_1, b_1] = [1, \beta_1]$)

$$\lambda = \frac{d(d+2)D}{L^2 + \beta_1 L(d+2)}. \quad (2.39)$$

Case C: homogeneous slab, annular or spherical shell geometry ($\ell_0 > 0$) with a reflecting inner boundary ($[a_0, b_0] = [0, 1]$) and an absorbing outer boundary ($[a_1, b_1] = [1, 0]$)

$$\lambda = \frac{d(d+2)(\ell_1^d - \ell_0^d)D}{\ell_1^{d+2} + (d+2)[\ell_0^{2d} \int_{\ell_0}^{\ell_1} r^{1-d} dr - \ell_0^d(\ell_1^2 - \ell_0^2)] - \ell_0^{d+2}}. \quad (2.40)$$

Case D: homogeneous slab, annular or spherical shell geometry ($\ell_0 > 0$) with a reflecting inner

boundary ($[a_0, b_0] = [0, 1]$) and a semi-absorbing outer boundary ($[a_1, b_1] = [1, \beta_1]$)

$$\lambda = \frac{d(d+2)(\ell_1^d - \ell_0^d)D}{\ell_1^{d+2} + (d+2)[\ell_0^{2d} \int_{\ell_0}^{\ell_1} r^{1-d} dr - \ell_0^d(\ell_1^2 - \ell_0^2) + \beta_1 \ell_1^{1-d}(\ell_1^d - \ell_0^d)^2] - \ell_0^{d+2}}. \quad (2.41)$$

Case E: homogeneous slab, annular or spherical shell geometry with absorbing inner ($[a_0, b_0] = [1, 0]$) and outer ($[a_1, b_1] = [1, 0]$) boundaries

$$\lambda = \frac{4d(d+2)(\ell_1^d - \ell_0^d)D}{4(\ell_1^{d+2} - \ell_0^{d+2}) - (d+2)(\ell_1^2 - \ell_0^2)^2[\int_{\ell_0}^{\ell_1} r^{1-d} dr]^{-1}}. \quad (2.42)$$

Case F: heterogeneous slab, circular or spherical geometry ($\ell_0 = 0, \ell_2 = L$) with radial symmetry at the origin ($[a_0, b_0] = [0, 1]$) and an absorbing boundary ($[a_1, b_1] = [1, 0]$)

$$\lambda = \frac{d(d+2)D_1 D_2}{L^2 D_1 + \ell_1^{d+2}(D_2 - D_1)/L^d}. \quad (2.43)$$

Case G: heterogeneous slab, circular or spherical geometry ($\ell_0 = 0, \ell_2 = L$) with radial symmetry at the origin ($[a_0, b_0] = [0, 1]$) and a semi-absorbing boundary ($[a_1, b_1] = [1, \beta_1]$)

$$\lambda = \frac{d(d+2)D_1 D_2}{(L^2 + \beta_1 L(d+2))D_1 + \ell_1^{d+2}(D_2 - D_1)/L^d}. \quad (2.44)$$

The above results yield easy-to-evaluate surrogate models that provide analytical insight into the role of dimension, diffusivity, geometry and boundary conditions on the proportion of particles remaining over time, $\mathcal{P}(t)$. For Case A (2.38), we observe that increasing the dimension d , increasing the diffusivity D or decreasing the radius L increases the decay rate λ . For Case B (2.39), decreasing β_1 (i.e. increasing the absorption probability P_O) also increases the decay rate λ . All these observations make physical sense when considering the homogeneous stochastic model (section 2.2) as particles are more likely to move outward than inward when the number of dimensions d is increased, particles jump more frequently or jump further when D is increased, particles have less distance to reach the absorbing boundary when L is decreased and particles are more likely to be absorbed when reaching the outer boundary when β_1 is decreased. For Case F (2.43) and Case G (2.44), moving the interface ($r = \ell_1$) closer to the outer boundary ($r = L$) increases λ if $D_2 < D_1$ while moving the interface ($r = \ell_1$) closer to the origin ($r = 0$) increases λ if $D_2 > D_1$. Both observations are consistent with the heterogeneous stochastic model (section 2.2).

2.4.4 Surrogate model 2: Two-term exponential model

The one-term exponential model (2.35) fails to accurately capture the fast early decay and slow late decay of $\mathcal{P}(t)$ [18]. To address this, we explore a surrogate model for $\mathcal{P}_c(t)$ consisting of

two exponential terms,

$$S_2(t) = \frac{1}{2} [e^{-\lambda_1 t} + e^{-\lambda_2 t}], \quad (2.45)$$

where $\lambda_1 > 0$ and $\lambda_2 > 0$ are constants that depend on the dimension, diffusivity, geometry and boundary conditions. The two-term exponential model (2.45) represents the simplest possible extension to two exponential terms with the factor of 1/2 ensuring that $S_2(0) = 1$. The inclusion of a second exponential term in (2.45) yields a time-dependent decay rate $\tilde{\lambda}_2(t) = -S'_2(t)/S_2(t)$, which decreases monotonically from $(\lambda_1 + \lambda_2)/2$ at $t = 0$ to $\min(\lambda_1, \lambda_2)$ as $t \rightarrow \infty$. The two-term exponential model therefore accommodates faster early decay and slower late decay that cannot be captured by the constant decay rate of the one-term exponential model (2.35).

To obtain λ_1 and λ_2 , we match the zeroth and first moments of $S_2(t)$ and $\mathcal{P}_c(t)$,

$$\int_0^\infty S_2(t) dt = \int_0^\infty \mathcal{P}_c(t) dt, \quad (2.46)$$

$$\int_0^\infty t S_2(t) dt = \int_0^\infty t \mathcal{P}_c(t) dt. \quad (2.47)$$

Substituting $S_2(t)$ (2.45) and $\mathcal{P}_c(t)$ ((2.17) or (2.18)) into equations (2.46) and (2.47), integrating exactly on the left hand side and reversing the order of integration on the right hand side yields

$$\frac{1}{2} \left[\frac{1}{\lambda_1} + \frac{1}{\lambda_2} \right] = \langle M_0(r) \rangle, \quad (2.48)$$

$$\frac{1}{2} \left[\frac{1}{\lambda_1^2} + \frac{1}{\lambda_2^2} \right] = \langle M_1(r) \rangle, \quad (2.49)$$

where $\langle M_0(r) \rangle$ and $\langle M_1(r) \rangle$ are defined in section 2.4.2. The exact solution of equations (2.48) and (2.49) is given by

$$\lambda_{1,2} = \frac{1}{\langle M_0(r) \rangle \pm \sqrt{\langle M_1(r) \rangle - \langle M_0(r) \rangle^2}}, \quad (2.50)$$

which is easily verified by substitution.

We now present several two-term exponential models for $\mathcal{P}(t)$. The models are again developed for the seven cases outlined in Table 2.1, with each model presented by providing closed-form expressions for λ_1 and λ_2 appearing in the two-term exponential model (2.45). For the homogeneous geometries (Cases A–E), λ_1 and λ_2 are calculated by solving the boundary value problem (2.22)–(2.24) for $k = 0, 1$, calculating $\langle M_k(r) \rangle$ (2.25) for $k = 0, 1$ and then computing λ_1 and λ_2 (2.50). For the heterogeneous geometries (Cases F–G), λ_1 and λ_2 are calculated by solving the boundary value problem (2.28)–(2.33) for $k = 0, 1$, calculating $\langle M_k(r) \rangle$ (2.34) for $k = 0, 1$ and then computing λ_1 and λ_2 (2.50) (see section 3.2.2). Results for Cases C/D and Cases F/G are combined for succinctness. In these cases, the formulas are given for Case D and G only, with the formulas for Case C and F obtained by setting $\beta_1 = 0$.

Case A: homogeneous slab, circular or spherical geometry ($\ell_0 = 0$, $\ell_1 = L$) with radial symmetry at the origin ($[a_0, b_0] = [0, 1]$) and an absorbing boundary ($[a_1, b_1] = [1, 0]$)

$$\lambda_{1,2} = \frac{d(d+2)D}{L^2(1 \pm \sqrt{d/(d+4)})}. \quad (2.51)$$

Case B: homogeneous slab, circular or spherical geometry ($\ell_0 = 0$, $\ell_1 = L$) with radial symmetry at the origin ($[a_0, b_0] = [0, 1]$) and a semi-absorbing boundary ($[a_1, b_1] = [1, \beta_1]$)

$$\lambda_{1,2} = \frac{d(d+2)D}{L^2(1 \pm \sqrt{d/(d+4)}) + \beta_1 L(d+2)}. \quad (2.52)$$

Case C/D: homogeneous slab, annular or spherical shell geometry ($\ell_0 > 0$) with a reflecting inner boundary ($[a_0, b_0] = [0, 1]$) and a semi-absorbing outer boundary ($[a_1, b_1] = [1, \beta_1]$)

Slab ($d = 1$)

$$\lambda_{1,2} = \frac{3D}{(\ell_1 - \ell_0)^2(1 \pm 1/\sqrt{5}) + 3\beta_1(\ell_1 - \ell_0)}.$$

Annular ($d = 2$)

$$\begin{aligned} \lambda_{1,2} &= \frac{8D(\ell_1^2 - \ell_0^2)}{(\ell_1^2 - \ell_0^2)(\ell_1^2 - 3\ell_0^2) + 4\ell_0^4 \log(\ell_1/\ell_0) + 4\beta_1(\ell_1^2 - \ell_0^2)^2/\ell_1 \pm \sqrt{\kappa_2/3}}, \\ \kappa_2 &= (\ell_1^2 - \ell_0^2)^3(\ell_1^2 - 7\ell_0^2) - 24\ell_0^4\ell_1^2 \log(\ell_1/\ell_0)(2\ell_0^2 \log(\ell_1/\ell_0) + \ell_0^2 - \ell_1^2). \end{aligned}$$

Spherical shell ($d = 3$)

$$\begin{aligned} \lambda_{1,2} &= \frac{15D(\ell_1^3 - \ell_0^3)}{(\ell_1 - \ell_0)^3(\ell_1^2 + 3\ell_0\ell_1 + 6\ell_0^2 + 5\ell_0^3/\ell_1 \pm \sqrt{3\kappa_3/7}) + 5\beta_1(\ell_1^3 - \ell_0^3)^2/\ell_1^2}, \\ \kappa_3 &= \ell_1^4 + 6\ell_0\ell_1^3 + 21\ell_0^2\ell_1^2 + 41\ell_0^3\ell_1 + 36\ell_0^4. \end{aligned}$$

Case E: homogeneous slab, annular or spherical shell geometry ($\ell_0 > 0$) with absorbing inner ($[a_0, b_0] = [1, 0]$) and outer ($[a_1, b_1] = [1, 0]$) boundaries

Slab ($d = 1$)

$$\lambda_{1,2} = \frac{12D}{(\ell_1 - \ell_0)^2(1 \pm 1/\sqrt{5})}. \quad (2.53)$$

Annular ($d = 2$)

$$\lambda_{1,2} = \frac{8D \log(\ell_1/\ell_0)}{(\ell_0^2 + \ell_1^2) \log(\ell_1/\ell_0) - (\ell_1^2 - \ell_0^2) \pm \sqrt{\xi_{2,1}/3}}, \quad (2.54)$$

$$\xi_{2,1} = 3(\ell_1^2 - \ell_0^2)^2 - 3(\ell_1^4 - \ell_0^4) \log(\ell_1/\ell_0) + (\ell_1^2 - \ell_0^2)^2 \log^2(\ell_1/\ell_0). \quad (2.55)$$

Spherical shell ($d = 3$)

$$\lambda_{1,2} = \frac{60D(\ell_1^3 - \ell_0^3)}{(\ell_1 - \ell_0)^3(4\ell_0^2 + 7\ell_0\ell_1 + 4\ell_1^2 \pm \sqrt{3\xi_{3,1}/7})}, \quad (2.56)$$

$$\xi_{3,1} = 16\ell_1^4 + 26\ell_0\ell_1^3 + 21\ell_0^2\ell_1^2 + 26\ell_0^3\ell_1 + 16\ell_0^4. \quad (2.57)$$

Case F/G: heterogeneous slab, circular or spherical geometry ($\ell_0 = 0, \ell_2 = L$), radial symmetry at the origin ($[a_0, b_0] = [0, 1]$) and a semi-absorbing boundary ($[a_1, b_1] = [1, \beta_1]$)

$$\lambda_{1,2} = \frac{d(d+2)D_1D_2}{[L^2 + \beta_1L(d+2)]D_1 + [\ell_1^{d+2}(D_2 - D_1) \pm \sqrt{\sigma_d/(d+4)}]/L^d}, \quad (2.58)$$

$$\begin{aligned} \sigma_d = & d(d+4)(D_2 - D_1)D_1L^{d+2}\ell_1^{d+2} - (d+4)(D_1 - D_2)^2\ell_1^{2d+4} + \\ & (d+2)((d+2)D_1^2 - (d+4)D_1D_2 + 2D_2^2)L^d\ell_1^{d+4} + dD_1^2L^{2d+4}. \end{aligned} \quad (2.59)$$

The above results yield easy-to-evaluate surrogate models that provide analytical insight into the role of dimension, diffusivity, geometry and boundary conditions on the proportion of particles remaining over time, $\mathcal{P}(t)$. As mentioned earlier, the two-term exponential model (2.45) accommodates faster early decay and slower late decay that cannot be captured by the constant decay rate of the one-term exponential model (2.35). This behaviour is clearly evident for Case A, where the expressions for λ_1 and λ_2 in the two-term exponential model (2.51) take a similar form to the expression for λ in the one-term exponential model (2.38), with the exception of correction terms in the denominator depending on the dimension d . Using these expressions for λ_1 and λ_2 , we see that the two-term exponential model exhibits an initial decay rate of $(\lambda_1 + \lambda_2)/2 = d(d+2)(d+4)D/(4L^2)$, which exceeds its late decay rate of $\lambda_1 = d(d+2)D/[L^2(1 + \sqrt{d/(d+4)})]$ for all $d = 1, 2, 3$. Comparing these decay rates to the constant decay rate of $\lambda = d(d+2)D/L^2$ for the one-term exponential model (2.38), it is clear that the two-term exponential model exhibits a larger initial decay rate and a smaller late decay rate. For Case A, we also observe that the early decay rate for the two-term exponential model is fastest for $d = 3$ and slowest for $d = 1$, and the later decay rate is slowest for $d = 3$ and fastest for $d = 1$, both of which are consistent with the behaviour of $\mathcal{P}(t)$ [18].

2.4.5 Surrogate model 3: Weighted two-term exponential model

Finally, we consider a surrogate model for $\mathcal{P}(t)$ which generalizes the two-term model (2.45) to an arbitrary weighting of the two exponential terms:

$$S_3(t) = \theta e^{-\lambda_1 t} + (1 - \theta)e^{-\lambda_2 t}, \quad (2.60)$$

where $\lambda_1 > 0, \lambda_2 > 0$ and $\theta \in (0, 1)$ are constants that depend on the dimension, diffusivity, geometry and boundary conditions. In a similar manner to the two-term exponential model (2.45), the weighted two-term exponential model (2.60) exhibits a time-dependent decay rate

$\tilde{\lambda}_3(t) = -S'_3(t)/S_3(t)$, however, the decay rate now decreases monotonically from $\theta\lambda_1 + (1-\theta)\lambda_2$ at $t = 0$ to $\min(\lambda_1, \lambda_2)$ as $t \rightarrow \infty$.

To obtain λ_1 , λ_2 and θ , we match the zeroth, first and second moments of $S_3(t)$ and $\mathcal{P}_c(t)$,

$$\int_0^\infty S_3(t) dt = \int_0^\infty \mathcal{P}_c(t) dt, \quad (2.61)$$

$$\int_0^\infty t S_3(t) dt = \int_0^\infty t \mathcal{P}_c(t) dt, \quad (2.62)$$

$$\int_0^\infty t^2 S_3(t) dt = \int_0^\infty t^2 \mathcal{P}_c(t) dt. \quad (2.63)$$

Substituting $S_3(t)$ (2.60) and $\mathcal{P}_c(t)$ ((2.17) or (2.18)) into equations (2.61)–(2.63), integrating exactly on the left hand side and reversing the order of integration on the right hand side yields

$$\frac{\theta}{\lambda_1} + \frac{1-\theta}{\lambda_2} = \langle M_0(r) \rangle, \quad (2.64)$$

$$\frac{\theta}{\lambda_1^2} + \frac{1-\theta}{\lambda_2^2} = \langle M_1(r) \rangle, \quad (2.65)$$

$$2 \left[\frac{\theta}{\lambda_1^3} + \frac{1-\theta}{\lambda_2^3} \right] = \langle M_2(r) \rangle, \quad (2.66)$$

where $\langle M_0(r) \rangle$, $\langle M_1(r) \rangle$ and $\langle M_2(r) \rangle$ are defined in section 2.4.2. The appropriate exact solution of equations (2.64)–(2.66) is given by

$$\lambda_1 = \frac{1}{\langle M_0(r) \rangle + \sqrt{(1-\theta)[\langle M_1(r) \rangle - \langle M_0(r) \rangle^2]/\theta}}, \quad (2.67)$$

$$\lambda_2 = \frac{1}{\langle M_0(r) \rangle - \sqrt{\theta[\langle M_1(r) \rangle - \langle M_0(r) \rangle^2]/(1-\theta)}}, \quad (2.68)$$

$$\theta = \frac{1}{2} + \frac{1}{2} \sqrt{\frac{\omega}{\omega+4}}, \quad (2.69)$$

$$\omega = \left[\frac{6\langle M_0(r) \rangle (\langle M_1(r) \rangle - \langle M_0(r) \rangle^2) + 2\langle M_0(r) \rangle^3 - \langle M_2(r) \rangle}{2(\langle M_1(r) \rangle - \langle M_0(r) \rangle^2)^{3/2}} \right]^2. \quad (2.70)$$

Note that the expressions for λ_1 and λ_2 here are different from those given for the two-term exponential model (2.50) expect for the special case when $\theta = 1/2$ ($\omega = 0$).

We now present weighted two-term exponential models of $\mathcal{P}(t)$ for Cases A–E outlined in Table 2.1. Each model is presented by providing closed-form expressions for λ_1 , λ_2 and ω , which when combined with the expression for θ (2.69) fully defines the weighted two-term exponential model (2.60). In each case, λ_1 , λ_2 and ω are calculated by solving the boundary value problem (2.22)–(2.24) for $k = 0, 1, 2$, calculating $\langle M_k(r) \rangle$ (2.25) for $k = 0, 1, 2$ and then processing (2.67)–(2.70) (see section 3.2.3). Results for Cases C/D are again combined for succinctness with the formulas given for Case D only and the formulas for Case C obtained by setting $\beta_1 = 0$.

Case A: homogeneous slab, circular or spherical geometry ($\ell_0 = 0$, $\ell_1 = L$) with radial

symmetry at the origin ($[a_0, b_0] = [0, 1]$) and an absorbing boundary ($[a_1, b_1] = [1, 0]$)

$$\lambda_1 = \frac{d(d+2)D}{L^2(1 + \sqrt{d(1-\theta)/(\theta(d+4))})}, \quad (2.71)$$

$$\lambda_2 = \frac{d(d+2)D}{L^2(1 - \sqrt{d\theta/((1-\theta)(d+4))})}, \quad (2.72)$$

$$\omega = \frac{d+4}{d} \left[\frac{6-d}{d+6} \right]^2. \quad (2.73)$$

Case B: homogeneous slab, circular or spherical geometry ($\ell_0 = 0, \ell_1 = L$) with radial symmetry at the origin ($[a_0, b_0] = [0, 1]$) and a semi-absorbing boundary ($[a_1, b_1] = [1, \beta_1]$)

$$\lambda_1 = \frac{d(d+2)D}{L^2(1 + \sqrt{d(1-\theta)/(\theta(d+4))}) + \beta_1 L(d+2)}, \quad (2.74)$$

$$\lambda_2 = \frac{d(d+2)D}{L^2(1 - \sqrt{d\theta/((1-\theta)(d+4))}) + \beta_1 L(d+2)}, \quad (2.75)$$

$$\omega = \frac{d+4}{dL^4} \left[\frac{(6-d)L^2 + (d+2)(d+6)\beta_1 L}{d+6} \right]^2. \quad (2.76)$$

Case C/D: homogeneous slab, annular or spherical shell geometry ($\ell_0 > 0$) with a reflecting inner boundary ($[a_0, b_0] = [0, 1]$) and a semi-absorbing outer boundary ($[a_1, b_1] = [1, \beta_1]$)

Slab ($d = 1$)

$$\begin{aligned} \lambda_1 &= \frac{3D}{(\ell_1 - \ell_0)^2(1 + \sqrt{(1-\theta)/(5\theta)}) + 3\beta_1(\ell_1 - \ell_0)}, \\ \lambda_2 &= \frac{3D}{(\ell_1 - \ell_0)^2(1 - \sqrt{\theta/(5(1-\theta))}) + 3\beta_1(\ell_1 - \ell_0)}, \\ \omega &= \frac{5(5(\ell_1 - \ell_0) + 21\beta_1)^2}{49(\ell_1 - \ell_0)^2}. \end{aligned}$$

Annular ($d = 2$)

$$\lambda_1 = \frac{8D(\ell_1^2 - \ell_0^2)}{(\ell_1^2 - \ell_0^2)(\ell_1^2 - 3\ell_0^2) + 4\ell_0^4 \log(\ell_1/\ell_0) + 4\beta_1(\ell_1^2 - \ell_0^2)^2/\ell_1 + \sqrt{(1-\theta)\kappa_{2,1}/(3\theta)}},$$

$$\lambda_2 = \frac{8D(\ell_1^2 - \ell_0^2)}{(\ell_1^2 - \ell_0^2)(\ell_1^2 - 3\ell_0^2) + 4\ell_0^4 \log(\ell_1/\ell_0) + 4\beta_1(\ell_1^2 - \ell_0^2)^2/\ell_1 - \sqrt{\theta\kappa_{2,1}/(3(1-\theta))}},$$

$$\omega = \frac{(288\kappa_{2,2} \log^2(\ell_1/\ell_0) - 1152\ell_0^8\ell_1^3(\ell_0^2 + \ell_1^2) \log^3(\ell_1/\ell_0) + 24\kappa_{2,3} \log(\ell_1/\ell_0) + \kappa_{2,4})}{12\ell_1^2\kappa_{2,1}^3},$$

$$\kappa_{2,1} = (\ell_1^2 - \ell_0^2)^3(\ell_1^2 - 7\ell_0^2) - 24\ell_0^4\ell_1^2 \log(\ell_1/\ell_0)(2\ell_0^2 \log(\ell_1/\ell_0) + \ell_0^2 - \ell_1^2),$$

$$\kappa_{2,2} = \ell_0^6\ell_1^2(\ell_1^2 - \ell_0^2)[\ell_1(5\ell_0^2 + \ell_1^2) - 4\beta_1(\ell_1^2 - \ell_0^2)],$$

$$\kappa_{2,3} = \ell_0^4\ell_1(\ell_1^2 - \ell_0^2)^2[7\ell_0^4 - 12\ell_0^2\ell_1^2 + 24\beta_1\ell_1(\ell_1^2 - \ell_0^2)],$$

$$\kappa_{2,4} = (\ell_1^2 - \ell_0^2)^3[\ell_1(3\ell_1^6 - 25\ell_0^2\ell_1^4 + 83\ell_0^4\ell_1^2 - 145\ell_0^6) - 24\beta_1(7\ell_0^2 - \ell_1^2)(\ell_1^2 - \ell_0^2)^2].$$

Spherical shell ($d = 3$)

$$\begin{aligned}\lambda_1 &= \frac{15D(\ell_1^3 - \ell_0^3)}{(\ell_1 - \ell_0)^3(\ell_1^2 + 3\ell_0\ell_1 + 6\ell_0^2 + 5\ell_0^3/\ell_1 + \sqrt{3\kappa_{3,1}(1-\theta)/(7\theta)}) + 5\beta_1(\ell_1^3 - \ell_0^3)^2/\ell_1^2}, \\ \lambda_2 &= \frac{15D(\ell_1^3 - \ell_0^3)}{(\ell_1 - \ell_0)^3(\ell_1^2 + 3\ell_0\ell_1 + 6\ell_0^2 + 5\ell_0^3/\ell_1 - \sqrt{3\kappa_{3,1}\theta/(7(1-\theta))}) + 5\beta_1(\ell_1^3 - \ell_0^3)^2/\ell_1^2}, \\ \omega &= \frac{7(\ell_1\kappa_{3,2}(\ell_1 - \ell_0)^3(\ell_1^2 + 4\ell_0\ell_1 + 10\ell_0^2) + 15\kappa_{3,1}\beta_1(\ell_1^3 - \ell_0^3)^2)^2}{27\kappa_{3,1}^3\ell_1^4(\ell_1 - \ell_0)^6}, \\ \kappa_{3,1} &= \ell_1^4 + 6\ell_0\ell_1^3 + 21\ell_0^2\ell_1^2 + 41\ell_0^3\ell_1 + 36\ell_0^4, \\ \kappa_{3,2} &= \ell_1^5 + 5\ell_0\ell_1^4 + 15\ell_0^2\ell_1^3 + 50\ell_0^3\ell_1^2 + 100\ell_0^4\ell_1 + 54\ell_0^5.\end{aligned}$$

Case E: homogeneous slab, annular or spherical shell geometry ($\ell_0 > 0$) with absorbing inner ($[a_0, b_0] = [1, 0]$) and outer ($[a_1, b_1] = [1, 0]$) boundaries

Slab ($d = 1$)

$$\lambda_1 = \frac{12D}{(\ell_1 - \ell_0)^2 + \sqrt{(1-\theta)/(5\theta)}}, \quad (2.77)$$

$$\lambda_2 = \frac{12D}{(\ell_1 - \ell_0)^2 - \sqrt{\theta/(5(1-\theta))}}, \quad (2.78)$$

$$\theta = \frac{1}{2} + \frac{1}{2}\sqrt{125/321}. \quad (2.79)$$

Annular ($d = 2$)

$$\lambda_1 = \frac{8D \log(\ell_1/\ell_0)}{(\ell_0^2 + \ell_1^2) \log(\ell_1/\ell_0) - (\ell_1^2 - \ell_0^2) + \sqrt{\xi_{2,1}(1-\theta)/(3\theta)}}, \quad (2.80)$$

$$\lambda_2 = \frac{8D \log(\ell_1/\ell_0)}{(\ell_0^2 + \ell_1^2) \log(\ell_1/\ell_0) - (\ell_1^2 - \ell_0^2) - \sqrt{\xi_{2,1}\theta/(3(1-\theta))}}, \quad (2.81)$$

$$\omega = \frac{\log^2(\ell_1/\ell_0)(18(\ell_0^2 + \ell_1^2)(\ell_1^2 - \ell_0^2)^2 + 6(\ell_0^2 + \ell_1^2)(\ell_0^4 + \ell_1^4) \log^2(\ell_1/\ell_0) - \xi_{2,2} \log(\ell_1/\ell_0))^2}{48\xi_{2,1}^3}, \quad (2.82)$$

$$\xi_{2,1} = 3(\ell_1^2 - \ell_0^2)^2 - 3(\ell_1^4 - \ell_0^4) \log(\ell_1/\ell_0) + (\ell_1^2 - \ell_0^2)^2 \log^2(\ell_1/\ell_0), \quad (2.83)$$

$$\xi_{2,2} = (\ell_1^2 - \ell_0^2)(19\ell_0^4 + 46\ell_0^2\ell_1^2 + 19\ell_1^4). \quad (2.84)$$

Spherical shell ($d = 3$)

$$\lambda_1 = \frac{60D(\ell_1^3 - \ell_0^3)}{(\ell_1 - \ell_0)^3(4\ell_0^2 + 7\ell_0\ell_1 + 4\ell_1^2 + \sqrt{3\xi_{3,1}(1-\theta)/(7\theta)})}, \quad (2.85)$$

$$\lambda_2 = \frac{60D(\ell_1^3 - \ell_0^3)}{(\ell_1 - \ell_0)^3(4\ell_0^2 + 7\ell_0\ell_1 + 4\ell_1^2 - \sqrt{3\xi_{3,1}\theta/(7(1-\theta))})}, \quad (2.86)$$

$$\omega = \frac{7(64\ell_0^6 + 471\ell_0^5\ell_1 + 780\ell_0^4\ell_1^2 + 745\ell_0^3\ell_1^3 + 780\ell_0^2\ell_1^4 + 471\ell_0\ell_1^5 + 64\ell_1^6)^2}{27\xi_{3,1}^3}, \quad (2.87)$$

$$\xi_{3,1} = 16\ell_1^4 + 26\ell_0\ell_1^3 + 21\ell_0^2\ell_1^2 + 26\ell_0^3\ell_1 + 16\ell_0^4. \quad (2.88)$$

The above results yield easy-to-evaluate surrogate models that provide analytical insight into the role of dimension, diffusivity, geometry and boundary conditions on the proportion of particles remaining over time, $\mathcal{P}(t)$. For Case A, the expressions for λ_1 (2.71) and λ_2 (2.72) in the weighted two-term exponential model take a similar form to the expression for λ_1 and λ_2 in the two-term exponential model (2.51), with the exception of correction terms in the denominator depending on the weighting θ . Using these expressions for λ_1 and λ_2 , we see that the weighted two-term exponential model exhibits initial decay rates of $\theta\lambda_1 + (1-\theta)\lambda_2 = 10D/L^2, 24D/L^2, 42D/L^2$ for $d = 1, 2, 3$, each of which exceed the initial decay rate of the two-term exponential model.

2.5 Results

We now investigate the accuracy of the three surrogate models (2.35), (2.45) and (2.60). Here, we consider the seven test cases outlined previously in Table 2.1 but with specific choices for the parameters as detailed in Table 2.2. For the homogeneous geometries (Cases A–E), we choose $P = \delta = \tau = 1$ giving $D = P\delta^2/(2d\tau) = 1/(2d)$ while for the heterogeneous geometries (Cases F–G) we choose $P_1 = 0.3$ and $P_2 = \delta = \tau = 1$ giving $D_1 = P_1\delta^2/(2d\tau) = 0.3/(2d)$ and $D_2 = P_2\delta^2/(2d\tau) = 1/(2d)$. The surrogate models for Cases A–E are given in sections 2.4.3–2.4.5 while the surrogate models for Cases F–G are given in sections 2.4.3–2.4.4. Surrogate model parameter values for Cases A–G in either one ($d = 1$), two ($d = 2$) or three ($d = 3$) dimensions can be found in Appendix A. All simulations are performed over a specified time interval $0 < t < T = 2 \log(10)/\lambda$, where λ is the decay rate in the one-term exponential model (section 2.4.3). This choice of T corresponds to the value of time satisfying $S_1(t) = 10^{-2}$ and captures the main region of decay of $\mathcal{P}(t)$ to easily detect differences between the surrogate models.

Case	Geometry	ℓ_0	ℓ_1	ℓ_2	Inner Boundary	Outer Boundary	a_0	b_0	a_1	b_1
A	homogeneous	0	100	—	—	absorbing	0	1	1	0
B	homogeneous	0	100	—	—	semi-absorbing ($P_O = 0.5$)	0	1	1	2
C	homogeneous	50	100	—	reflecting	absorbing	0	1	1	0
D	homogeneous	50	100	—	reflecting	semi-absorbing ($P_O = 0.5$)	0	1	1	2
E	homogeneous	50	100	—	absorbing	absorbing	1	0	1	0
F	heterogeneous	0	50	100	—	absorbing	0	1	1	0
G	heterogeneous	0	50	100	—	semi-absorbing ($P_O = 0.5$)	0	1	1	2

Table 2.2: Geometry and boundary parameters for Cases A–G.

Each surrogate model is benchmarked against the stochastic and continuum model. To account for the variability of $\mathcal{P}_s(t)$ (2.3) from the stochastic model, we perform $N_s = 100$ simulations using $N_p = 50$ and $N_p = 500$ particles. For each value of N_p , we store the minimum and maximum values of $\mathcal{P}_s(t)$ at each time step across all $N_s = 100$ simulations with the resulting area enclosed encompassing all realizations of $\mathcal{P}_s(t)$. For the heterogeneous geometries (Cases F–G), we choose $n = 36$ and $n_1 = n_2 = 12$ [57] when processing the movement probabilities at the interface (see section 2.2.2). To calculate $\mathcal{P}_c(t)$ from the continuum model, we first compute a numerical solution to the homogeneous continuum model (2.4)–(2.7) (Cases A–E) or the heterogeneous continuum model (2.8)–(2.14) (Cases F–G) by discretising in space using a finite volume method and discretising in time using the Crank-Nicolson method (see section 3.3). We use $N_t = 10^5$ fixed time steps and $N_r = 501$ (Cases A–E) or $N_r = 1001$ (Cases F–G) uniformly-spaced nodes. For both the homogeneous continuum model (2.4)–(2.7) and the heterogeneous continuum model (2.8)–(2.14), this yields approximations $c(r_i, t_j)$ where $r_i = \ell_0 + (i - 1)(\ell_m - \ell_0)/(N_r - 1)$ ($m = 1$ for Cases A–E and $m = 2$ for Cases F–G) and $t_j = jT/N_t$ for $i = 1, \dots, N_r$ and $j = 1, \dots, N_t$. Using these discrete approximations, $c(r_i, t_j)$, and a trapezoidal rule approximation to the integrals (2.17) or (2.18) then allows $P_c(t_j)$ to be computed for $j = 1, \dots, N_t$. In addition to visual comparisons, to quantify the accuracy of the surrogate models, we also use the mean absolute error between each surrogate model and $\mathcal{P}_c(t)$,

$$\varepsilon_k = \frac{1}{N_t} \sum_{j=1}^{N_t} |C_k(t_j) - \mathcal{P}_c(t_j)|, \quad (2.89)$$

where $k = 1, \dots, 3$. Full details of the above implementations are available in our MATLAB code which can be accessed on GitHub: https://github.com/lukefilippini/Filippini_2023.

Figure 2.2 and Figure 2.3 compare the surrogate models to the benchmark values of $\mathcal{P}_s(t)$ and $\mathcal{P}_c(t)$ obtained from the stochastic and continuum models. Figure 2.2 assesses the performance of the one-term (2.35), two-term (2.45) and weighted two-term exponential models (2.60) for the homogeneous test cases (Cases A–E) while Figure 2.3 assesses the performance of the one-term (2.35) and two-term (2.45) exponential models for the heterogeneous test cases (Cases F–G). All subfigures feature the final time T and the corresponding mean absolute errors (2.89) for each surrogate model. Results are shown for $d = 2$ only with similar results observed

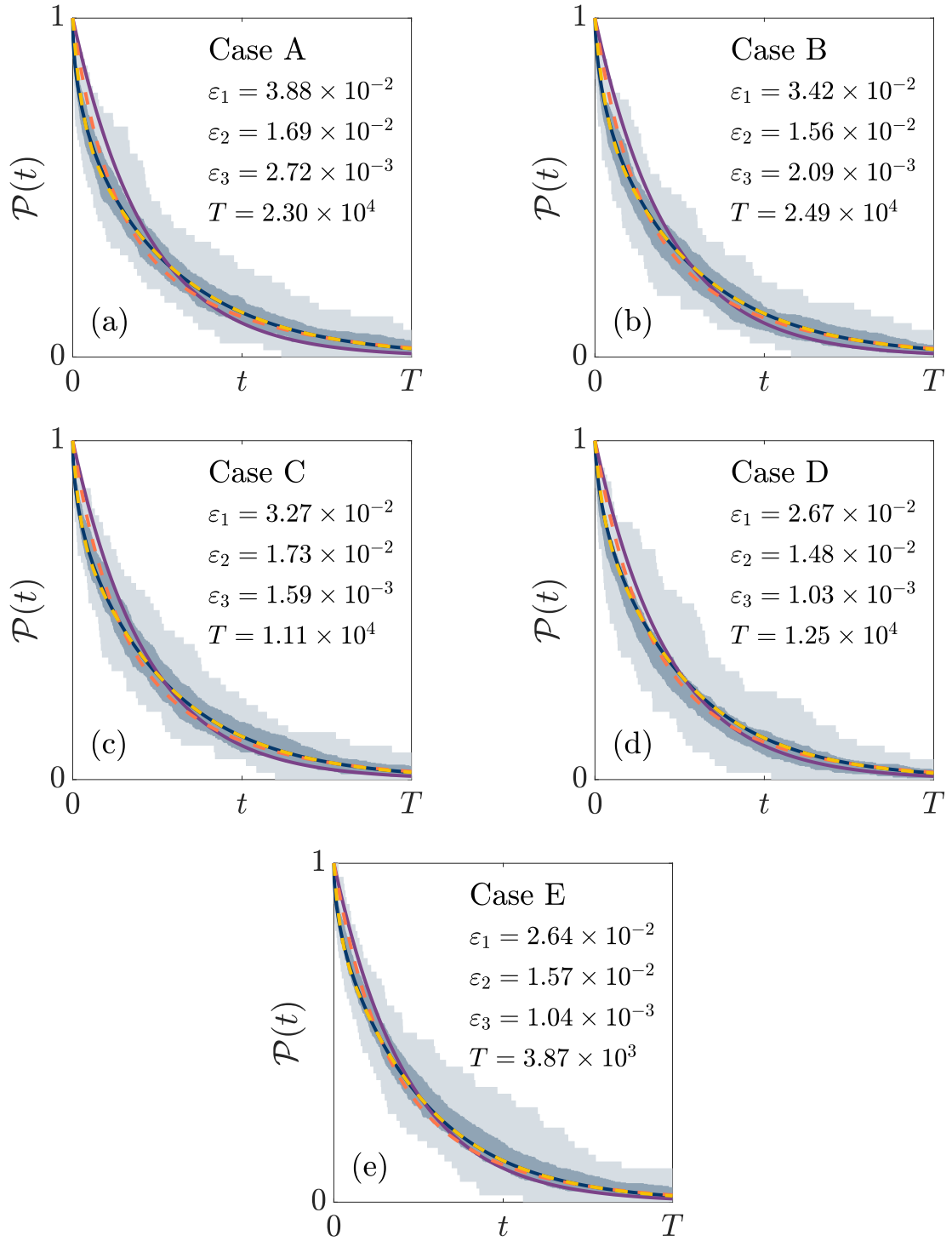


Figure 2.2: One-term, two term, and weighted two-term exponential models for $\mathcal{P}(t)$ compared with stochastic and continuum models for the homogeneous test cases (Cases A–E) with $d = 2$. For the stochastic model, the bounds of the shaded regions represent the maximum and minimum proportion of particles remaining at each point in time across the $N_s = 100$ simulations. The mean absolute errors ε_1 , ε_2 and ε_3 and final time T are rounded to three significant digits.

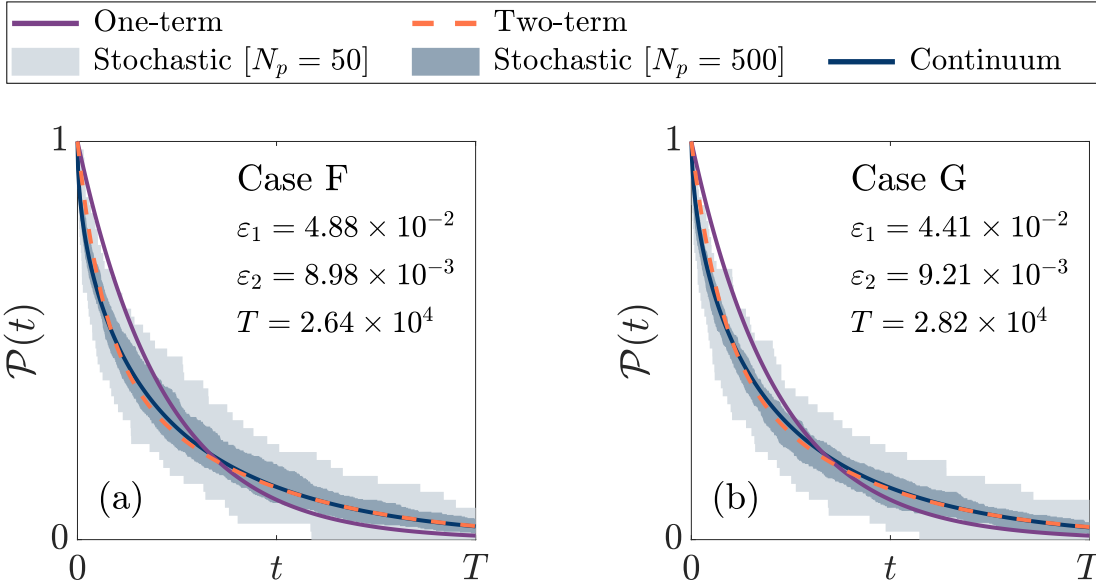


Figure 2.3: One-term and two-term exponential models for $\mathcal{P}(t)$ compared with stochastic and continuum models for the heterogeneous test cases (Cases F–G) with $d = 2$. For the stochastic model, the bounds of the shaded regions represent the maximum and minimum proportion of particles remaining at each point in time across the $N_s = 100$ simulations. The mean absolute errors ε_1 and ε_2 and final time T are rounded to three significant digits.

for $d = 1, 3$ (see section 3.4). From the results in Figure 2.2 and Figure 2.3, we can conclude that:

- All surrogate models reliably capture the release profile over the seven test cases but with varying levels of accuracy.
- The one-term exponential model (2.35) has the lowest accuracy of the three models across all seven test cases, however, it is the most simplistic and may potentially be sufficient in some cases.
- The weighted two-term exponential model (2.60) provides the highest accuracy, capturing the early and late decay of $\mathcal{P}(t)$ more accurately than the one-term (2.35) and two-term (2.45) models, however, this comes with the trade-off of increased model complexity.
- All three surrogate models yield higher accuracy for test cases with semi-absorbing boundary conditions (Cases B, D and G) when compared to test cases with purely absorbing boundary conditions (Cases A, C, E and F).

Finally, we compare the surrogate models developed in this paper to the Weibull model of Carr [18], which was developed for homogeneous geometries only (i.e. Cases A–E). Table 3 displays the mean absolute errors for the Weibull model, denoted as ε_w , for Cases A–E. In comparison to the mean absolute errors presented in Figure 2.2, we find that the Weibull model is more accurate than the one-term (2.35) and two-term (2.45) exponential models but less accurate than the weighted two-term exponential model (2.60).

Case	A	B	C	D	E
ε_w	1.05×10^{-2}	9.21×10^{-3}	1.03×10^{-2}	8.42×10^{-3}	9.22×10^{-3}

Table 2.3: Mean absolute errors for the Weibull model of Carr [18] (Cases A–E).

2.6 Conclusion

We have considered the problem of particle diffusion in d -dimensional radially-symmetric geometries with reflecting, absorbing and/or semi-absorbing boundaries. By matching moments with the continuum analogue of the stochastic diffusion model, we have presented several new one-term and two-term exponential models for $\mathcal{P}(t)$, the proportion of particles remaining within the geometry over time. New surrogate models have been developed for three main problems: (i) homogeneous slab, circular and spherical geometries with an absorbing or semi-absorbing outer boundary (ii) homogeneous slab, annular and spherical shell geometries with absorbing, reflecting and/or semi-absorbing boundaries and (iii) heterogeneous slab, circular and spherical geometries with an absorbing or semi-absorbing outer boundary. Each surrogate model provides a simple approximation of $\mathcal{P}(t)$ that is easy to evaluate, avoids the limitations and complexity of exact expressions obtained from the continuum model, reliably captures the particle release profile over time and explicitly depends on the physical parameters of the diffusive transport system: dimension, diffusivity, geometry and boundary conditions. Of the three surrogate models developed, our findings demonstrated that the weighted two-term exponential model (2.60) captures both stochastic and continuum calculations of $\mathcal{P}(t)$ with the highest degree of accuracy. It also offers improved simplicity and accuracy when compared to the Weibull model previously presented by Carr [18].

The results reported in this paper indicate, as may have been expected, that the most accurate surrogate model is the one with the greatest number of parameters (weighted two-term exponential model) and the least accurate surrogate model is the one with the fewest number of parameters (one-term exponential model). To account for this trade-off between model accuracy and model complexity, a standard model selection criterion that rewards accuracy but penalises the number of parameters [64] could be used to select a single preferred surrogate model. Other avenues for future research (see section 3.5) could include accounting for a non-uniform initial distribution of particles or drift and/or decay in the diffusive transport process. Additionally, surrogate models using different functional forms could also be explored. Surrogate models using different functional forms, such as a weighted two-term Weibull model, could also be explored and may further improve accuracy but at the cost of increased model complexity.

Chapter 3

Supporting information for surrogate model development

3.1 Analysis of analytical solutions for $\mathcal{P}_c(t)$

In section 2.4.1, we presented an exact expression for $\mathcal{P}_c(t)$ for a homogeneous disc ($d = 2$) with $\ell_0 = 0$, $\ell_1 = L$, radial symmetry at the origin ($[a_0, b_0] = [0, 1]$) and a semi-absorbing boundary ($[a_1, b_1], [1, \beta_1]$). The limitations of this model for $\mathcal{P}(t)$ were identified and used as a motivation for the development of the one-term, two-term and weighted two-term surrogate models in sections 2.4.3–2.4.5, respectively. In this section, we derive the analytical solution for $\mathcal{P}_c(t)$ presented in section 2.4.1 and those for a homogeneous slab and sphere with the same parameter configurations (Case B of Table 2.1). These exact solutions are then truncated and compared against analogous numerical results for $\mathcal{P}_c(t)$ (see section 3.3). The drawbacks of the exact solutions are then discussed in further detail. Finally, we show that an initial-value problem can be derived for $\mathcal{P}_c(t)$, although dependence on $c(r, t)$ can only be eliminated for a trivial choice of boundary conditions.

3.1.1 Separation of variables and eigenfunction expansion

In this section, we present exact solutions for the continuum analogue (2.17) of $\mathcal{P}(t)$,

$$\mathcal{P}_c(t) = \frac{d}{\ell_1^d - \ell_0^d} \int_{\ell_0}^{\ell_1} r^{d-1} c(r, t) dt.$$

To illustrate the limitations associated with analytical solutions for $\mathcal{P}_c(t)$, we consider Case B of Table 2.1: a homogeneous slab, circular or spherical geometry ($\ell_0 = 0$, $\ell_1 = L$) with radial symmetry at the origin ($[a_0, b_0] = [0, 1]$) and a semi-absorbing boundary ($[a_1, b_1] = [1, \beta_1]$). We use separation of variables and eigenfunction expansion to obtain expressions for $c(r, t)$, and then apply (2.17) to give exact solutions for $\mathcal{P}_c(t)$. Firstly, we consider the continuum model (2.4)–(2.7) and assume that $c(r, t)$ can be expressed as the product $c(r, t) = R(r)T(t)$, which

can be substituted into the model (2.4) to give

$$\frac{T'}{DT} = \frac{1}{r^{d-1}R} \frac{d}{dr}(r^{d-1}R) = -\eta^2 \quad (3.1)$$

where $\eta > 0$ is an arbitrary constant. Considering $R(r)$, we rearrange (3.1) to obtain the ordinary differential equations

$$\begin{cases} R'' + \eta^2 R = 0, & \text{for } d = 1, \\ r^2 R'' + rR' + (\eta r)^2 R = 0, & \text{for } d = 2, \\ r^2 R'' + 2rR' + (\eta r)^2 R = 0, & \text{for } d = 3, \end{cases}$$

subject to the boundary conditions $R'(0) = 0$ and $R(L) + \beta_1 R'(L) = 0$. Thus, we obtain, for $n = 1, 2, \dots$, the unique solutions

$$R_n(r) = \begin{cases} \cos(\eta_n r), & \text{for } d = 1, \\ J_0(\eta_n r), & \text{for } d = 2, \\ \sin(\eta_n r)/(\eta_n r), & \text{for } d = 3, \end{cases}$$

where $J_\nu(\cdot)$ is the Bessel function of the first kind of order ν and η_n are the positive roots of the transcendental equations

$$\begin{cases} \tan(\eta_n L) = 1/(\beta_1 \eta_n), & \text{for } d = 1, \\ J_1(\eta_n L)/J_0(\eta_n L) = 1/(\beta_1 \eta_n), & \text{for } d = 2, \\ \tan(\eta_n L) = \beta_1 \eta_n L / (\beta_1 - L), & \text{for } d = 3. \end{cases} \quad (3.2)$$

Now, we consider $T(t)$ by first rearranging (3.1). We obtain the ordinary differential equation $T'_n + \eta_n^2 DT_n = 0$, which has the general solution

$$T_n(t) = A_n e^{-\eta_n^2 D t}.$$

Thus, we obtain the following general solutions for $c(r, t)$,

$$c(r, t) = \begin{cases} \sum_{n=1}^{\infty} A_n \cos(\eta_n r) e^{-\eta_n^2 D t}, & \text{for } d = 1, \\ \sum_{n=1}^{\infty} A_n J_0(\eta_n r) e^{-\eta_n^2 D t}, & \text{for } d = 2, \\ \sum_{n=1}^{\infty} A_n \sin(\eta_n r)/(\eta_n r) e^{-\eta_n^2 D t}, & \text{for } d = 3. \end{cases} \quad (3.3)$$

Substituting (3.3) into the initial condition (2.5) and using orthogonality of eigenfunctions, we can express the coefficients A_n as

$$A_n = \begin{cases} 4 \sin(\eta_n L) / (2\eta_n L + \sin(2\eta_n L)), & \text{for } d = 1, \\ \int_0^L r J_0(\eta_n r) dr / \int_0^L r J_0(\eta_n r)^2 dr, & \text{for } d = 2, \\ 4(\sin(\eta_n L) - \eta_n L \cos(\eta_n L)) / (2\eta_n L - \sin(2\eta_n L)), & \text{for } d = 3. \end{cases}$$

Finally, by calculating the average using (2.17), we obtain exact solutions for the continuum analogue of $\mathcal{P}(t)$,

Slab ($d = 1$):

$$\mathcal{P}_c(t) = \frac{4}{L} \sum_{n=1}^{\infty} \frac{\sin^2(2\eta_n L)}{2\eta_n^2 + \eta_n \sin(2\eta_n L)} e^{-\eta_n^2 D t}, \quad (3.4)$$

Circular ($d = 2$):

$$\mathcal{P}_c(t) = \frac{2}{L^2} \sum_{n=1}^{\infty} \frac{\left[\int_0^L r J_0(\eta_n r) dr \right]^2}{\int_0^L r J_0(\eta_n r)^2 dr} e^{-\eta_n^2 D t}, \quad (3.5)$$

Spherical ($d = 3$):

$$\mathcal{P}_c(t) = \frac{12}{L^3} \sum_{n=1}^{\infty} \frac{[\sin(\eta_n L) - \eta_n L \cos(\eta_n L)]^2}{\eta_n^3 [2\eta_n L - \sin(2\eta_n L)]} e^{-\eta_n^2 D t}. \quad (3.6)$$

3.1.2 Limitations of continuum models

Here, we discuss the limitations associated with the continuum analogues (3.4)–(3.6) of $\mathcal{P}(t)$. These limitations arise from the complexity of the expressions, methods for determining roots of the transcendental equations (3.2) and truncation requirements. Firstly, the roots of the transcendental equations (3.2) do not have exact solutions and must be approximated using numerical methods. We use MATLAB's **fzero** [65] function to determine the roots of each equation in (3.2), subject to appropriate initial guesses for each root. Example values are presented in Table 3.1 for Case B of Table 2.2. The primary issue with these roots is that they lack analytical insight. To elaborate, the numerical techniques used to approximate the roots limit meaningful interpretation of the precise influence of the radius and boundary conditions on the values of η_n . Furthermore, the initial guesses required must be very precise to avoid incorrect approximation of the roots, particularly as the frequency of the functions on the left hand side of (3.2) increases. This requires visual inspection or an approximation which must be redefined for each new set of parameters. The roots must then be used within each term of the infinite series solutions (3.4)–(3.6), which are complicated terms that, for a disc ($d = 2$), require numerical integration. Additionally, given that the continuum analogues (3.4)–(3.6) are not closed-form, truncation is required to give a suitable number of terms which sufficiently approximate the true solution for $\mathcal{P}_c(t)$. Figure 3.1 displays a comparison between the series

Root	η_1	η_2	η_3	η_4	η_5
Slab ($d = 1$)	0.0154	0.0462	0.0770	0.1078	0.1387
Disc ($d = 2$)	0.0236	0.0541	0.0848	0.1156	0.1464
Sphere ($d = 3$)	0.0308	0.0616	0.0924	0.1232	0.1540

Table 3.1: Numerical roots of the transcendental equations (3.2) determined using MATLAB's `fzero` [65] function for Case B of Table 2.2.

solutions, truncated at one and two terms, and numerical calculations (see sections 2.5 and 3.3) for slab, circular and spherical geometries. These comparisons demonstrate that more than two terms are required to accurately capture the early decay of $\mathcal{P}(t)$ for high probabilities of particle absorption at the outer boundary, or small values of β_1 . On the other hand, the two-term (2.45) and weighted two-term (2.60) surrogate models accurately capture this early decay and are simpler in form than the series solutions. To summarise, the complexity of the terms of each infinite series, the need for truncation and repeated numerical techniques all diminish the potential for meaningful analytical insight into the precise influence of each physical parameter on $\mathcal{P}(t)$.

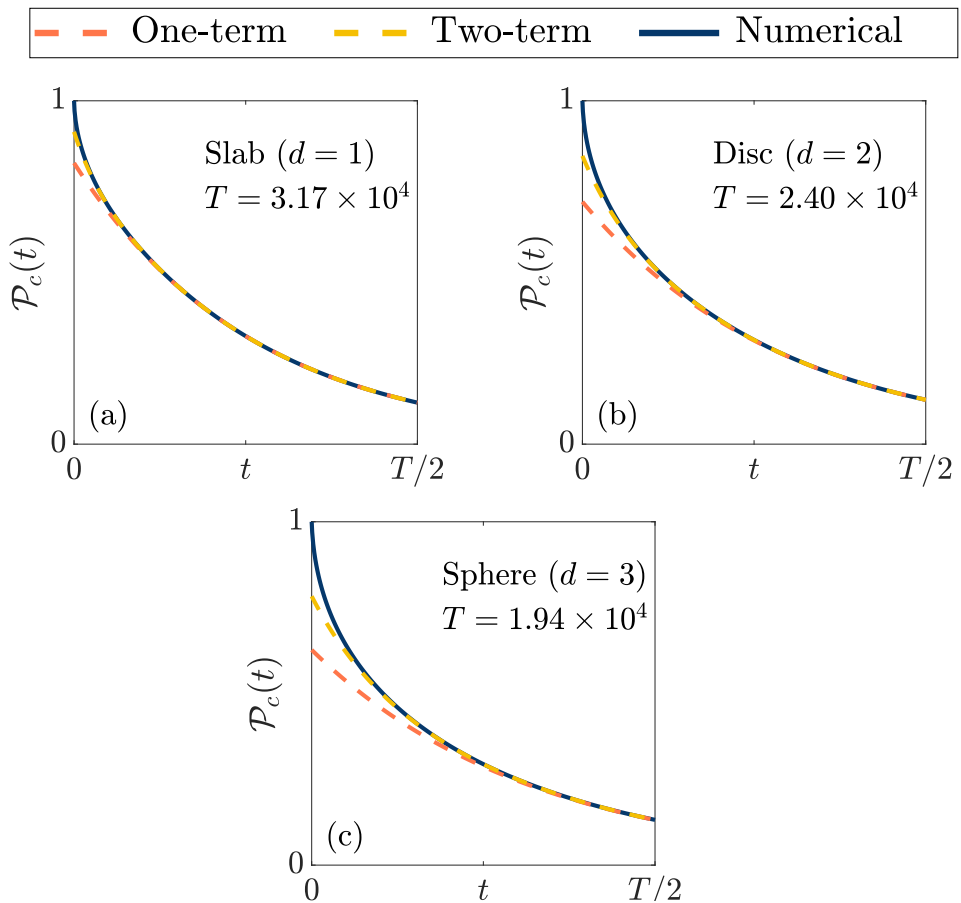


Figure 3.1: One-term and two-term series solutions for $\mathcal{P}_c(t)$ compared with numerical results for a homogenous (a) slab, (b) disc and (c) sphere with radial symmetry at the origin and a semi-absorbing outer boundary (Case B of Table 2.1). Here, we choose $L = 100$, $\beta_1 = 1.053$ ($P_0 = 0.95$) and $D = 0.5, 0.25, 0.167$ for $d = 1, 2, 3$, respectively. The final time T is rounded to three significant digits.

3.1.3 Initial value problem for $\mathcal{P}_c(t)$

Finally, it is important to note that we can obtain an initial value problem satisfied by $\mathcal{P}_c(t)$ by averaging the continuum model (2.4)–(2.7) or (2.8)–(2.14) for the homogeneous and heterogeneous geometries, respectively. However, this is only valid for a trivial set of boundary conditions. Considering the continuum model (2.4)–(2.7) for the homogeneous geometries, applying the averaging operator (2.17) to the diffusion equation (2.4) yields

$$\frac{d\mathcal{P}_c}{dt} = \frac{dD}{\ell_1^d - \ell_0^d} \left[\ell_1^{d-1} \frac{\partial c}{\partial r}(\ell_1, t) - \ell_0^{d-1} \frac{\partial c}{\partial r}(\ell_0, t) \right]. \quad (3.7)$$

In the trivial case that both boundaries are reflecting, such that $a_0 = a_1 = 0$ and $b_0 = b_1 = 1$, the ordinary differential equation (3.7) simplifies to $d\mathcal{P}_c/dt = 0$. Thus, $\mathcal{P}_c(t) = 1$ for all time, as no particles are able to exit the system. However, if at least one boundary is absorbing or semi-absorbing, such that $a_0 \neq 0$ and/or $a_1 \neq 0$, we obtain

$$\frac{d\mathcal{P}}{dt} = \frac{dD}{\ell_1^d - \ell_0^d} \left[\frac{a_0 \ell_0^{d-1}}{b_0} c(\ell_0, t) - \frac{a_1 \ell_1^{d-1}}{b_1} c(\ell_1, t) \right],$$

which implies that it is not possible to eliminate the dependence of $\mathcal{P}_c(t)$ on the continuum solution $c(r, t)$.

3.2 Surrogate model development and analysis

In sections 2.4.3–2.4.5, we presented surrogate models for $\mathcal{P}(t)$ obtained by matching moments with the continuum analogue of the stochastic diffusion model. In this section, we provide detailed derivations of the one-term, two-term and weighted two-term models for $\mathcal{P}(t)$ for some of the cases given in Table 2.1. Firstly, we derive the formula (2.37) for λ for the one-term model (2.35) and consider unique solutions for Cases B, E and G of Table 2.1. Secondly, we consider the two-term model (2.45) and derive the formula (2.50) for $\lambda_{1,2}$. Using this formula, we then construct unique expressions for (2.50) for the same three cases. Thirdly, we derive the formulas (2.67)–(2.70) for λ_1 , λ_2 , θ and ω for the weighted model (2.60) and consider Cases B and E for the homogeneous geometries. Finally, we illustrate the usefulness of surrogate models for simplifying the fitting of experimental release data. This is shown by using the one-term model (2.35) to estimate the diffusivity for Case B of Table 2.1.

3.2.1 One-term model

Considering the one-term model (2.35), we follow [18] and match the zeroth moments of $S_1(t)$ and $\mathcal{P}_c(t)$. Substituting in the one-term model (2.35) and continuum analogue (2.17) or (2.18)

into the condition (2.36), we obtain

$$\begin{aligned}\int_0^\infty e^{-\lambda t} dt &= \int_0^\infty \left[\frac{d}{\ell_1^d - \ell_0^d} \int_{\ell_0}^{\ell_1} r^{d-1} c(r, t) dr \right] dt, \\ \int_0^\infty e^{-\lambda t} dt &= \int_0^\infty \left[\frac{d}{\ell_2^d - \ell_0^d} \left[\int_{\ell_0}^{\ell_1} r^{d-1} c_1(r, t) dr + \int_{\ell_1}^{\ell_2} r^{d-1} c_2(r, t) dr \right] \right] dt,\end{aligned}$$

for the homogeneous and heterogeneous geometries, respectively. The order of integration on the right hand side can be rearranged and the definitions (2.21) for $M_0(r)$ and (2.26) for $M_0^{(1)}(r)$ and $M_0^{(2)}(r)$, where $k = 0$, allow for simplification. Integrating and evaluating on the left hand side, we then obtain

$$\begin{aligned}\frac{1}{\lambda} &= \frac{d}{\ell_1^d - \ell_0^d} \int_{\ell_0}^{\ell_1} r^{d-1} M_0(r) dr, \\ \frac{1}{\lambda} &= \frac{d}{\ell_2^d - \ell_0^d} \left[\int_{\ell_0}^{\ell_1} r^{d-1} M_0^{(1)}(r) dr + \int_{\ell_1}^{\ell_2} r^{d-1} M_0^{(2)}(r) dr \right].\end{aligned}$$

Lastly, we use the definition of $\langle M_0(r) \rangle$, given by (2.25) for the homogeneous geometries or (2.34) for the heterogeneous geometries, where $k = 0$. The expression $1/\lambda = \langle M_0(r) \rangle$ is obtained, which can be inverted to recover (2.37),

$$\lambda = \frac{1}{\langle M_0(r) \rangle}.$$

Homogeneous geometries

Considering the homogeneous geometries, we determine closed-form analytical expressions for the zeroth moment $M_0(r)$. The ordinary differential equation (2.22), where $k = 0$,

$$\frac{D}{r^{d-1}} \frac{d}{dr} \left(r^{d-1} \frac{dM_0}{dr} \right) = -1,$$

can be solved to give a general solution for $M_0(r)$, and we then obtain unique solutions for Cases B and E of Table 2.1. Finally, analytical expressions for $\langle M_0(r) \rangle$ are then obtained by applying (2.25), where $k = 0$,

$$\langle M_0(r) \rangle = \frac{d}{\ell_1^d - \ell_0^d} \int_{\ell_0}^{\ell_1} r^{d-1} M_0(r) dr, \quad (3.8)$$

to the unique solutions for $M_0(r)$. The general solution for $M_0(r)$ is given by

$$M_0(r) = k_1 I_1(r) - \frac{r^2}{2dD} + k_2, \quad (3.9)$$

$$I_1(r) = \int_{\ell_0}^r z_1^{1-d} dz_1, \quad (3.10)$$

where k_1 and k_2 are constants. The definite integral $I_1(r)$ allows $M_0(r)$ to be expressed in terms

of a general dimension d , and closed-form expressions for $d = 1, 2, 3$ are given in [Appendix B](#). To determine k_1 and k_2 , we first consider Case B. The boundary conditions [\(2.23\)](#) and [\(2.24\)](#), where $k = 0$, simplify to

$$\frac{dM_0}{dr}(0) = 0, \quad M_0(L) + \beta_1 \frac{dM_0}{dr}(L) = 0,$$

which, when applied to [\(3.9\)](#), yield $k_1 = 0$ and $k_2 = (L^2 + 2\beta_1 L)/(2dD)$. Thus, we have a unique solution for $M_0(r)$, and the spatial average $\langle M_0(r) \rangle$ can be obtained by applying [\(3.8\)](#),

$$M_0(r) = \frac{L^2 - r^2 + 2\beta_1 L}{2dD}, \quad (3.11)$$

$$\langle M_0(r) \rangle = \frac{L^2 + (d+2)\beta_1 L}{d(d+2)D}. \quad (3.12)$$

[Figure 3.2](#) presents a validation of the analytical solution [\(3.11\)](#) for $M_0(r)$ by comparison with numerical values obtained using MATLAB's **bvp4c** [66] function. The code that computes the numerical solution and generates the figure is available on GitHub (https://github.com/lukefilippini/Filippini_2023.git).

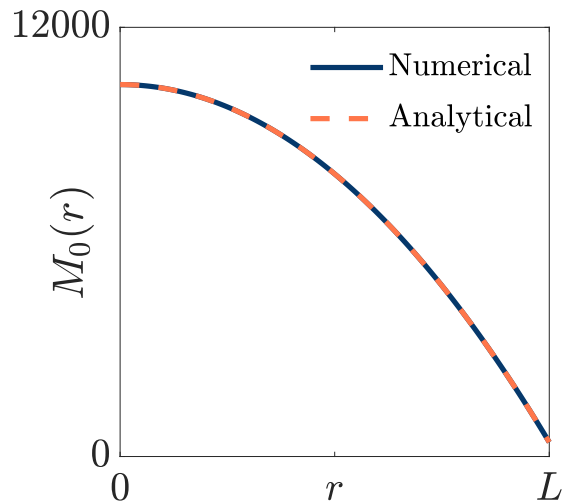


[Figure 3.2](#): Comparison between analytical and numerical solutions for the zeroth moment, $M_0(r)$, for homogeneous slab, circular and spherical geometries with radial symmetry at the origin and a semi-absorbing boundary (Case B of [Table 2.1](#)). Note that the solutions for $M_0(r)$ do not vary with dimension.

The expression [\(2.38\)](#) for λ is recovered by substituting the spatial average [\(3.12\)](#) into the general solution [\(2.37\)](#). We restate [\(2.38\)](#) for convenience,

$$\lambda = \frac{d(d+2)D}{L^2 + \beta_1 L(d+2)}.$$

Next, we consider Case E. The boundary conditions [\(2.23\)](#) and [\(2.24\)](#), where $k = 0$, are simplified to $M_0(\ell_0) = M_0(\ell_1) = 0$ and give simultaneous equations that can be presented as a

linear system. The constants k_1 and k_2 are obtained by solving

$$\begin{bmatrix} k_1 \\ k_2 \end{bmatrix} = \mathbf{A}_d^{-1} \begin{bmatrix} \ell_0^2/(2dD) \\ \ell_1^2/(2dD) \end{bmatrix}, \quad \mathbf{A}_d = \begin{bmatrix} 0 & 1 \\ I_1(\ell_1) & 1 \end{bmatrix},$$

which gives the unique solutions $k_1 = (\ell_1^2 - \ell_0^2)/(2dDI_1(\ell_1))$ and $k_2 = \ell_0^2/(2dD)$, where $I_1(r)$ is defined in [Appendix B](#). Hence, we have a unique solution for $M_0(r)$, and the spatial average $\langle M_0(r) \rangle$ is obtained by applying (3.8),

$$\begin{aligned} M_0(r) &= \frac{(\ell_1^2 - \ell_0^2)I_1(r) - (r^2 - \ell_0^2)I_1(\ell_1)}{2dDI_1(\ell_1)}, \\ \langle M_0(r) \rangle &= \frac{d(d+2)(\ell_1^2 - \ell_0^2)I_2(\ell_1) - [d(\ell_1^{d+2} - \ell_0^{d+2}) + (d+2)(\ell_1^d - \ell_0^d)\ell_0^2]I_1(\ell_1)}{2d(d+2)(\ell_1^d - \ell_0^d)DI_1(\ell_1)}, \\ I_2(r) &= \int_{\ell_0}^r z_2^{d-1} I_1(z_2) dz_2. \end{aligned} \quad (3.13)$$

It can be shown that $I_2(r) = I_1(r)r^d/d - (r^2 - \ell_0^2)/(2d)$, which implies that the expression (3.13) can be simplified to give

$$\langle M_0(r) \rangle = \frac{4(\ell_1^{d+2} - \ell_0^{d+2}) - (d+2)(\ell_1^2 - \ell_0^2)^2 [I_1(\ell_1)]^{-1}}{4d(d+2)(\ell_1^d - \ell_0^d)D}. \quad (3.14)$$

The expression (2.42) for λ can then be recovered by inverting the spatial average (3.14),

$$\lambda = \frac{4d(d+2)(\ell_1^d - \ell_0^d)D}{4(\ell_1^{d+2} - \ell_0^{d+2}) - (d+2)(\ell_1^2 - \ell_0^2)^2 [\int_{\ell_0}^{\ell_1} r^{1-d} dr]^{-1}}.$$

Heterogeneous geometries

Considering the heterogeneous geometries, we determine closed-form analytical expressions for the zeroth moments $M_0^{(1)}(r)$ and $M_0^{(2)}(r)$ for the inner ($\ell_0 < r < \ell_1$) and outer ($\ell_1 < r < \ell_2$) layers, respectively. The ordinary differential equations (2.28) and (2.29), where $k = 0$,

$$\frac{D_1}{r^{d-1}} \frac{d}{dr} \left(r^{d-1} \frac{dM_0^{(1)}}{dr} \right) = -1, \quad \frac{D_2}{r^{d-1}} \frac{d}{dr} \left(r^{d-1} \frac{dM_0^{(2)}}{dr} \right) = -1,$$

can be solved to give a general solution for $M_0^{(1)}(r)$ and $M_0^{(2)}(r)$, respectively. Unique solutions for both quantities are then obtained by applying the boundary and interface conditions (2.30)–(2.33), where $k = 0$. Here, we consider Case G of [Table 2.1](#) and solve for $M_0^{(1)}(r)$ and $M_0^{(2)}(r)$ subject to

$$\frac{dM_0^{(1)}}{dr}(0) = 0, \quad M_0^{(2)}(L) + \beta_1 \frac{dM_0^{(2)}}{dr}(L) = 0, \quad (3.15)$$

$$M_0^{(1)}(\ell_1) = M_0^{(2)}(\ell_1), \quad D_1 \frac{dM_0^{(1)}}{dr}(\ell_1) = D_2 \frac{dM_0^{(2)}}{dr}(\ell_1). \quad (3.16)$$

Lastly, an analytical solution for $\langle M_0(r) \rangle$ is then obtained by applying (2.34), where $k = 0$,

$$\langle M_0(r) \rangle = \frac{d}{\ell_2^d - \ell_0^d} \left[\int_{\ell_0}^{\ell_1} r^{d-1} M_0^{(1)}(r) \, dr + \int_{\ell_1}^{\ell_2} r^{d-1} M_0^{(2)}(r) \, dr \right], \quad (3.17)$$

to the unique solutions for $M_0^{(1)}(r)$ and $M_0^{(2)}(r)$. The general solutions for $M_0^{(1)}(r)$ and $M_0^{(2)}(r)$ are given by

$$M_0^{(1)}(r) = k_1 I_1^{(1)}(r) - \frac{r^2}{2dD_1} + k_2, \quad M_0^{(2)}(r) = k_3 I_1^{(2)}(r) - \frac{r^2}{2dD_2} + k_4,$$

$$I_1^{(1)}(r) = \int_{\ell_0}^r z_1^{1-d} \, dz_1, \quad I_1^{(2)}(r) = \int_{\ell_1}^r z_1^{1-d} \, dz_1,$$

where k_1, k_2, k_3 and k_4 are constants. Closed-form expressions for $I_1^{(1)}(r)$ and $I_1^{(2)}(r)$ are given in Appendix B. The boundary and interface conditions (3.15)–(3.16) yield the unique solutions $k_1 = k_3 = 0$, $k_2 = [(L^2 + 2\beta_1 L)D_1 + \ell_1^2(D_2 - D_1)]/(2dD_1D_2)$ and $k_4 = (L^2 + 2\beta_1 L)/(2dD_2)$ for the constants. Thus, we obtain unique solutions for $M_0^{(1)}(r)$ and $M_0^{(2)}(r)$ and determine the spatial average $\langle M_0(r) \rangle$ by applying (3.17),

$$M_0^{(1)}(r) = \frac{(L^2 - \ell_1^2 + 2\beta_1 L)D_1 + D_2(\ell_1^2 - r^2)}{2dD_1D_2}, \quad M_0^{(2)}(r) = \frac{L^2 - r^2 + 2\beta_1 L}{2dD_1},$$

$$\langle M_0(r) \rangle = \frac{D_1 [L^2 + \beta_1 L(d+2)] + \ell_1^{d+2} (D_2 - D_1) / L^d}{d(d+2)D_1D_2}. \quad (3.18)$$

The spatial average (3.18) can be inverted to recover the expression (2.44) for λ , which we restate for convenience,

$$\lambda = \frac{d(d+2)D_1D_2}{(L^2 + \beta_1 L(d+2))D_1 + \ell_1^{d+2}(D_2 - D_1)/L^d}.$$

3.2.2 Two-term model

Considering the two-term model (2.45), we propose a matching of the zeroth and first moments of $S_2(t)$ and $\mathcal{P}_c(t)$. Substituting in the two-term model (2.45) and continuum analogue (2.17) or (2.18) into the conditions (2.46) and (2.47), we obtain

$$\frac{1}{2} \int_0^\infty e^{-\lambda_1 t} + e^{-\lambda_2 t} \, dt = \langle M_0(r) \rangle, \quad (3.19)$$

$$\frac{1}{2} \int_0^\infty t [e^{-\lambda_1 t} + e^{-\lambda_2 t}] \, dt = \langle M_1(r) \rangle, \quad (3.20)$$

where the spatial average $\langle M_1(r) \rangle$ is obtained by following a process analogous to that discussed in section 3.2.1. Note that we have already determined expressions for $\langle M_0(r) \rangle$ for Cases B, E and G of Table 2.1. Integrating and evaluating on the left hand side of (3.19), and using

integration by parts for (3.20), we recover (2.48) and (2.49), respectively,

$$\frac{1}{2} \left[\frac{1}{\lambda_1} + \frac{1}{\lambda_2} \right] = \langle M_0(r) \rangle, \quad \frac{1}{2} \left[\frac{1}{\lambda_1^2} + \frac{1}{\lambda_2^2} \right] = \langle M_1(r) \rangle.$$

Using the expression (2.48), we rearrange for $1/\lambda_1$ and substitute into (2.49) to give a quadratic expression in $1/\lambda_2$,

$$\left(\frac{1}{\lambda_2} \right)^2 - 2\langle M_0(r) \rangle \left(\frac{1}{\lambda_2} \right) + 2\langle M_0(r) \rangle^2 - \langle M_1(r) \rangle = 0. \quad (3.21)$$

The roots of (3.21) are obtained by using the quadratic formula. We choose the root

$$\frac{1}{\lambda_2} = \langle M_0(r) \rangle - \sqrt{\langle M_1(r) \rangle - \langle M_0(r) \rangle^2}. \quad (3.22)$$

to give a single value for λ_2 , although the other root could alternatively be chosen with no difference arising in the form of $S_2(t)$. Lastly, (3.22) can be substituted into (2.48) to give the other root of the quadratic expression (3.21),

$$\frac{1}{\lambda_1} = \langle M_0(r) \rangle + \sqrt{\langle M_1(r) \rangle - \langle M_0(r) \rangle^2}. \quad (3.23)$$

Thus, inverting (3.22) and (3.23) recovers the expression (2.50) for $\lambda_{1,2}$,

$$\lambda_{1,2} = \frac{1}{\langle M_0(r) \rangle \pm \sqrt{\langle M_1(r) \rangle - \langle M_0(r) \rangle^2}}.$$

Homogeneous geometries

Considering the homogeneous geometries, we determine closed-form analytical expressions for the first moment $M_1(r)$. The ordinary differential equation (2.22), where $k = 1$,

$$\frac{D}{r^{d-1}} \frac{d}{dr} \left(r^{d-1} \frac{dM_1}{dr} \right) = -M_0(r), \quad (3.24)$$

can be solved to give a general solution for $M_1(r)$. We obtain unique solutions for Cases B and E of Table 2.1, as in section 3.2.1. Lastly, analytical expressions for $\langle M_1(r) \rangle$ can be obtained by applying (2.25), where $k = 1$,

$$\langle M_1(r) \rangle = \frac{d}{\ell_1^d - \ell_0^d} \int_{\ell_0}^{\ell_1} r^{d-1} M_1(r) dr, \quad (3.25)$$

to the unique solutions for $M_1(r)$. The general solution for $M_1(r)$ is given by

$$M_1(r) = \gamma_1(r) + g_1 I_1(r) + g_2, \quad (3.26)$$

$$\gamma_1(r) = \frac{r^4}{8d(d+2)D^2} - \frac{k_1}{D} I_3(r) - \frac{k_2}{2dD} r^2, \quad (3.27)$$

$$I_3(r) = \int_{\ell_0}^r z_3^{1-d} I_2(z_3) dz_3. \quad (3.28)$$

where g_1 and g_2 are constants and k_1 and k_2 are given in section 3.2.1 for Cases B and E. Note that the general solution (3.9)–(3.10) for $M_0(r)$ is substituted in to the right hand side of (3.24). Expressions for $I_3(r)$ for $d = 1, 2, 3$ are given in Appendix B. Now, we first determine unique expressions for g_1 and g_2 for Case B. The boundary conditions (2.23) and (2.24), where $k = 1$, simplify to

$$\frac{dM_1}{dr}(0) = 0, \quad M_1(L) + \beta_1 \frac{dM_1}{dr}(L) = 0,$$

which give $g_1 = 0$ and $g_2 = [(d+4)(L^2 + 2\beta_1 L)^2 + 4d\beta_1^2 L^2] / [8d^2(d+2)D^2]$. Thus, we obtain a unique solution for $M_1(r)$ and determine the spatial average $\langle M_1(r) \rangle$ by using (3.25),

$$M_1(r) = \frac{(L^2 + 2\beta_1 L) [(d+4)(L^2 + 2\beta_1 L) - 2(d+2)r^2] + dr^4 + 4d\beta_1^2 L^2}{8d^2(d+2)D^2}, \quad (3.29)$$

$$\langle M_1(r) \rangle = \frac{2(L^2 + 2\beta_1 L)^2 + 2d\beta_1 L^3 + d(d+6)\beta_1^2 L^2}{d^2(d+2)^2(d+4)D^2}. \quad (3.30)$$

Figure 3.3 shows that the analytical solution (3.29) is valid when compared to numerical values for $d = 1, 2, 3$, obtained using MATLAB's **bvp4c** [66] function. The code which computes the numerical solutions and generates the figures is available on GitHub (https://github.com/lukefilippini/Filippini_2023.git). We now substitute the spatial averages (3.12) and (3.30) for $M_0(r)$ and $M_1(r)$, respectively, into the general expression (2.50) for $\lambda_{1,2}$ and simplify to recover (2.52),

$$\lambda_{1,2} = \frac{d(d+2)D}{L^2(1 \pm \sqrt{d/(d+4)}) + \beta_1 L(d+2)}.$$

Next, we consider Case E. The boundary conditions (2.23) and (2.24), where $k = 1$, are simplified to $M_1(\ell_0) = M_1(\ell_1) = 0$. These conditions yield unique expressions for g_1 and g_2 , which are obtained by solving the linear system

$$\begin{bmatrix} g_1 \\ g_2 \end{bmatrix} = \mathbf{A}_d^{-1} \begin{bmatrix} -\gamma_1(\ell_0) \\ -\gamma_1(\ell_1) \end{bmatrix}, \quad \mathbf{A}_d = \begin{bmatrix} 0 & 1 \\ I_1(\ell_1) & 1 \end{bmatrix}.$$

We do not present expressions for $M_1(r)$ and $\langle M_1(r) \rangle$ due to their length and complexity. Regardless, analytical solutions for $M_1(r)$ and $\langle M_1(r) \rangle$ can be determined using Wolfram Mathematica [67] to minimise tedious by-hand solutions and human error. Mathematica and by-hand simplification were used to determine the expressions (2.53)–(2.56), which we restate for convenience,

Slab ($d = 1$)

$$\lambda_{1,2} = \frac{12D}{(\ell_1 - \ell_0)^2(1 \pm 1/\sqrt{5})}.$$

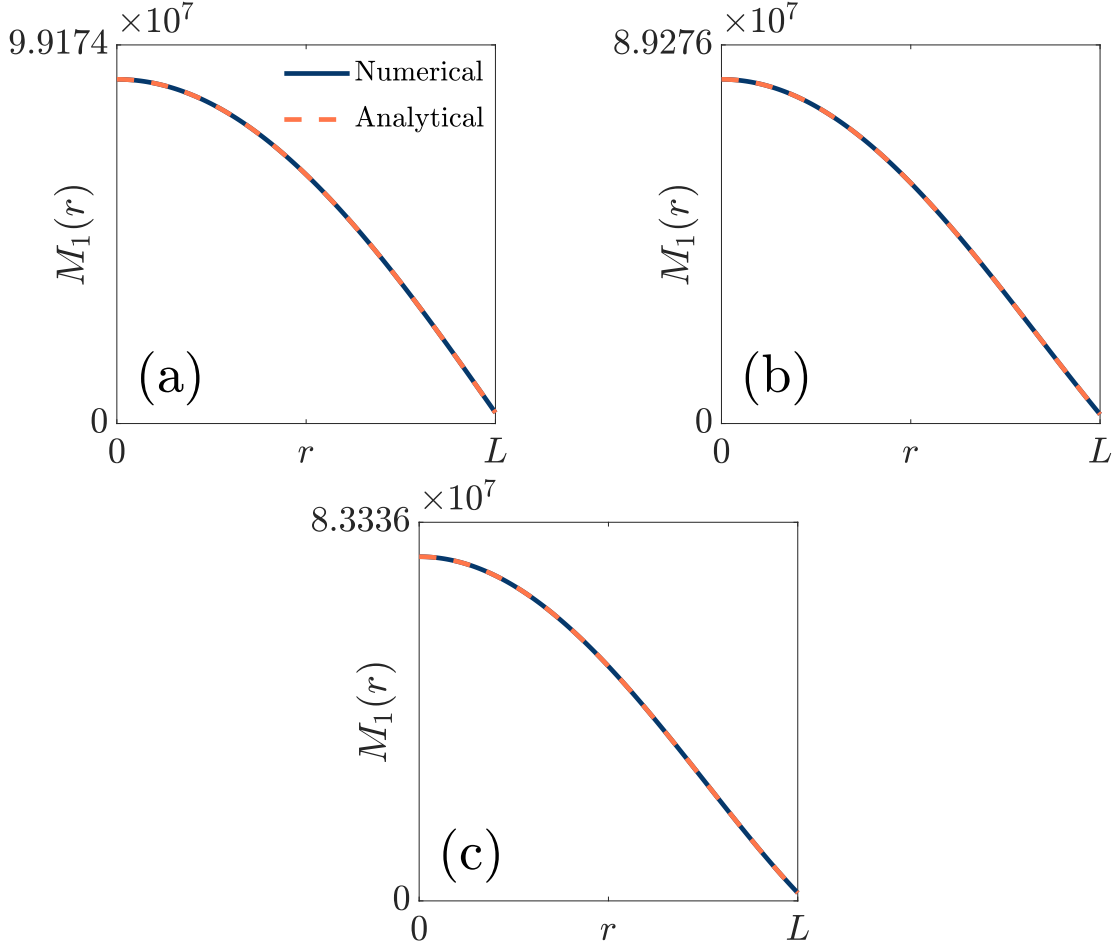


Figure 3.3: Comparisons between analytical and numerical solutions for the first moment, $M_1(r)$, for homogeneous (a) slab, (b) circular and (c) spherical geometries with radial symmetry at the origin and a semi-absorbing boundary (Case B of Table 2.1).

Annular ($d = 2$)

$$\lambda_{1,2} = \frac{8D \log(\ell_1/\ell_0)}{(\ell_0^2 + \ell_1^2) \log(\ell_1/\ell_0) - (\ell_1^2 - \ell_0^2) \pm \sqrt{\xi_{2,1}/3}},$$

$$\xi_{2,1} = 3(\ell_1^2 - \ell_0^2)^2 - 3(\ell_1^4 - \ell_0^4) \log(\ell_1/\ell_0) + (\ell_1^2 - \ell_0^2)^2 \log^2(\ell_1/\ell_0).$$

Spherical shell ($d = 3$)

$$\lambda_{1,2} = \frac{60D(\ell_1^3 - \ell_0^3)}{(\ell_1 - \ell_0)^3(4\ell_0^2 + 7\ell_0\ell_1 + 4\ell_1^2 \pm \sqrt{3\xi_{3,1}/7})},$$

$$\xi_{3,1} = 16\ell_1^4 + 26\ell_0\ell_1^3 + 21\ell_0^2\ell_1^2 + 26\ell_0^3\ell_1 + 16\ell_0^4.$$

Heterogeneous geometries

Considering the heterogeneous geometries, we determine closed-form analytical expressions for the first moments $M_1^{(1)}(r)$ and $M_1^{(2)}(r)$ (2.26) for the inner ($\ell_0 < r < \ell_1$) and outer ($\ell_1 < r < \ell_2$)

layers, respectively. The ordinary differential equations (2.28) and (2.29), where $k = 1$,

$$\frac{D_1}{r^{d-1}} \frac{d}{dr} \left(r^{d-1} \frac{dM_1^{(1)}}{dr} \right) = -M_0^{(1)}(r), \quad \frac{D_2}{r^{d-1}} \frac{d}{dr} \left(r^{d-1} \frac{dM_1^{(2)}}{dr} \right) = -M_0^{(2)}(r),$$

can be solved to give general solutions for $M_1^{(1)}(r)$ and $M_1^{(2)}(r)$, respectively. Unique solutions for both quantities are then obtained by applying the boundary and interface conditions (2.30)–(2.33), where $k = 1$. As in section 3.2.1, we consider Case G in Table 2.1 and, hence, apply the conditions

$$\frac{dM_1^{(1)}}{dr}(0) = 0, \quad M_1^{(2)}(L) + \beta_1 \frac{dM_1^{(2)}}{dr}(L) = 0, \quad (3.31)$$

$$M_1^{(1)}(\ell_1) = M_1^{(2)}(\ell_1), \quad D_1 \frac{dM_1^{(1)}}{dr}(\ell_1) = D_2 \frac{dM_1^{(2)}}{dr}(\ell_1), \quad (3.32)$$

Finally, we obtain an analytical solution for $\langle M_1(r) \rangle$ by applying (2.34), where $k = 1$,

$$\langle M_1(r) \rangle = \frac{d}{\ell_2^d - \ell_0^d} \left[\int_{\ell_0}^{\ell_1} r^{d-1} M_1^{(1)}(r) dr + \int_{\ell_1}^{\ell_2} r^{d-1} M_1^{(2)}(r) dr \right], \quad (3.33)$$

to the unique solutions for $M_1^{(1)}(r)$ and $M_1^{(2)}(r)$. The general solutions for $M_1^{(1)}(r)$ and $M_1^{(2)}(r)$ are given by

$$M_1^{(1)}(r) = \frac{2r^2(d+2)[(L^2 - \ell_1^2 + 2\beta_1 L)D_1 + \ell_1^2 D_2] - dr^4 D_2}{8d^2(d+2)D_1^2 D_2} + h_1 I_1^{(1)}(r) + h_2,$$

$$M_1^{(2)}(r) = \frac{2r^2(d+2)(L^2 + 2\beta_1 L) - dr^4}{8d^2(d+2)D_2^2} + h_3 I_1^{(2)}(r) + h_4,$$

where h_1 , h_2 , h_3 and h_4 are constants. Unique solutions for these constants, which we do not present for readability, are determined by applying the boundary and interface conditions (3.31)–(3.32). The spatial average $\langle M_1(r) \rangle$ can be calculated by applying (3.33),

$$\langle M_1(r) \rangle = \frac{[2(L^2 + 2\beta_1 L)^2 + 2d\beta_1 L^3 + d(d+6)\beta_1^2 L^2]D_1^2 - \eta_d}{d^2(d+2)(d+4)D_1^2 D_2^2}, \quad (3.34)$$

$$\eta_d = \ell_1^{d+2}(D_2 - D_1)[(d+4)(L^2 - \ell_1^2 + 2\beta_1 L)D_1 + 2\ell_1^2(D_1 - D_2)]. \quad (3.35)$$

By substituting in the spatial averages (3.18) and (3.34)–(3.35) into the general expression (2.50) for $\lambda_{1,2}$, we recover (2.58)–(2.59),

$$\lambda_{1,2} = \frac{d(d+2)D_1 D_2}{[L^2 + \beta_1 L(d+2)]D_1 + [\ell_1^{d+2}(D_2 - D_1) \pm \sqrt{\sigma_d/(d+4)}]/L^d},$$

$$\sigma_d = d(d+4)(D_2 - D_1)D_1 L^{d+2} \ell_1^{d+2} - (d+4)(D_1 - D_2)^2 \ell_1^{2d+4} + (d+2)((d+2)D_1^2 - (d+4)D_1 D_2 + 2D_2^2)L^d \ell_1^{d+4} + dD_1^2 L^{2d+4}.$$

3.2.3 Weighted two-term model

Considering the weighted two-term model (2.60), we propose a matching of the zeroth, first and second moments of $S_3(t)$ and $\mathcal{P}_c(t)$. Substituting in the weighted two-term model (2.60) and continuum analogue (2.17) or (2.18) into the conditions (2.61)–(2.63), we obtain

$$\int_0^\infty \theta e^{-\lambda_1 t} + (1-\theta)e^{-\lambda_2 t} dt = \langle M_0(r) \rangle, \quad (3.36)$$

$$\int_0^\infty t [\theta e^{-\lambda_1 t} + (1-\theta)e^{-\lambda_2 t}] dt = \langle M_1(r) \rangle, \quad (3.37)$$

$$\int_0^\infty t^2 [\theta e^{-\lambda_1 t} + (1-\theta)e^{-\lambda_2 t}] dt = \langle M_2(r) \rangle, \quad (3.38)$$

where the spatial average $\langle M_2(r) \rangle$ is obtained by following a process analogous to those described in sections 3.2.1 and 3.2.2. Note that analytical expressions for $\langle M_0(r) \rangle$ and $\langle M_1(r) \rangle$ have been determined for Cases B, E and G of Table 2.1. Integrating and evaluating on the left hand side of (3.36), and using integration by parts for (3.37) and (3.38), we recover (2.64)–(2.66),

$$\frac{\theta}{\lambda_1} + \frac{1-\theta}{\lambda_2} = \langle M_0(r) \rangle, \quad \frac{\theta}{\lambda_1^2} + \frac{1-\theta}{\lambda_2^2} = \langle M_1(r) \rangle, \quad 2 \left[\frac{\theta}{\lambda_1^3} + \frac{1-\theta}{\lambda_2^3} \right] = \langle M_2(r) \rangle.$$

Using the expression (2.64), we rearrange for $1/\lambda_1$ and substitute into (2.65) to give a quadratic expression in $1/\lambda_2$,

$$\left(\frac{1}{\lambda_2} \right) - 2\langle M_0(r) \rangle \left(\frac{1}{\lambda_2} \right) + \frac{\langle M_0(r) \rangle^2}{1-\theta} - \frac{\theta \langle M_1(r) \rangle}{1-\theta} = 0. \quad (3.39)$$

The roots of (3.39) are obtained by using the quadratic formula. We choose the following root for λ_2 :

$$\frac{1}{\lambda_2} = \langle M_0(r) \rangle - \sqrt{\theta [\langle M_1(r) \rangle - \langle M_0(r) \rangle^2] / (1-\theta)}, \quad (3.40)$$

which can be substituted into (2.64) to give

$$\frac{1}{\lambda_1} = \langle M_0(r) \rangle + \sqrt{(1-\theta) [\langle M_1(r) \rangle - \langle M_0(r) \rangle^2] / \theta}. \quad (3.41)$$

Thus, inverting (3.40) and (3.41) recovers the expressions (2.68) and (2.67) for λ_1 and λ_2 , respectively,

$$\begin{aligned} \lambda_1 &= \frac{1}{\langle M_0(r) \rangle + \sqrt{(1-\theta)[\langle M_1(r) \rangle - \langle M_0(r) \rangle^2] / \theta}}, \\ \lambda_2 &= \frac{1}{\langle M_0(r) \rangle - \sqrt{\theta[\langle M_1(r) \rangle - \langle M_0(r) \rangle^2] / (1-\theta)}}. \end{aligned}$$

Finally, substituting in (3.40) and (3.41) into (2.66) and performing laborious rearrangement

yields a quadratic expression in terms of the weighting parameter θ ,

$$\begin{aligned} & (\omega + 4)\theta^2 - (\omega + 4)\theta + 1 = 0, \\ \omega = & \left[\frac{6\langle M_0(r) \rangle (\langle M_1(r) \rangle - \langle M_0(r) \rangle^2) + 2\langle M_0(r) \rangle^3 - \langle M_2(r) \rangle}{2(\langle M_1(r) \rangle - \langle M_0(r) \rangle^2)^{3/2}} \right]^2. \end{aligned} \quad (3.42)$$

We choose the root (2.69) of (3.42),

$$\theta = \frac{1}{2} + \frac{1}{2}\sqrt{\frac{\omega}{\omega + 4}}.$$

A trial and error approach shows that choosing the configuration immediately above for λ_1 , λ_2 and θ satisfies the matching of the zeroth, first and second moments of $S_3(t)$ and $\mathcal{P}_c(t)$, while enforcing $\lambda_1 > 0$, $\lambda_2 > 0$ and $\theta \in [0, 1]$. Alternatively, one could also choose

$$\begin{aligned} \lambda_1 &= \frac{1}{\langle M_0(r) \rangle - \sqrt{(1-\theta)[\langle M_1(r) \rangle - \langle M_0(r) \rangle^2]/\theta}}, \\ \lambda_2 &= \frac{1}{\langle M_0(r) \rangle + \sqrt{\theta[\langle M_1(r) \rangle - \langle M_0(r) \rangle^2]/(1-\theta)}}, \\ \theta &= \frac{1}{2} - \frac{1}{2}\sqrt{\frac{\omega}{\omega + 4}}, \end{aligned}$$

and the weighted two-term model results (see section 2.5) would remain unchanged.

Homogeneous geometries

Considering the homogeneous geometries, we can determine closed-form analytical expressions for the second moment $M_2(r)$. The ordinary differential equation (2.22), where $k = 2$,

$$\frac{D}{r^{d-1}} \frac{d}{dr} \left(r^{d-1} \frac{dM_2}{dr} \right) = -2M_1(r),$$

can be solved to give a general solution for $M_2(r)$,

$$M_2(r) = \gamma_2(r) + h_1 I_1(r) + h_2, \quad (3.43)$$

$$\gamma_2(r) = \frac{2k_1}{D^2} I_5(r) + \frac{k_2}{4d(d+2)D^2} r^4 - \frac{r^6}{24d(d+2)(d+4)D^3} - \frac{2g_1}{D} I_3(r) - \frac{g_2}{dD} r^2, \quad (3.44)$$

$$I_4(r) = \int_{\ell_0}^r z_4^{d-1} I_3(r) dz_4, \quad I_5(r) = \int_{\ell_0}^r z_5^{1-d} I_4(r) dz_5,$$

where h_1 and h_2 are constants and k_1 , k_2 , g_1 and g_2 are given in sections 3.2.1 and 3.2.2 for Cases B and E of Table 2.1. Note that the general solution (3.26)–(3.28) for $M_1(r)$ is substituted in as the right hand side of (2.22). Evaluations of $I_4(r)$ and $I_5(r)$ for $d = 1, 2, 3$ are available in Appendix B. Analytical expressions for $\langle M_2(r) \rangle$ can be obtained by applying (2.25), where $k = 2$,

$$\langle M_2(r) \rangle = \int_{\ell_0}^{\ell_1} r^{d-1} M_2(r) \, dr.$$

Here, we do not present analytical expressions for $M_2(r)$ or $\langle M_2(r) \rangle$. Mathematica [67] calculations and by-hand simplification were used to determine the expressions λ_1 , λ_2 and ω for Cases B and E in section 2.4.5, respectively.

3.2.4 Parameter estimation using one-term model (2.35)

Surrogate models, such as the one-term (2.35), two-term (2.45) and weighted two-term (2.60) models presented in this work, avoid the limitations of the continuum analogue of $\mathcal{P}(t)$ outlined in sections 2.4.1 and 3.1.2. To elaborate, these models are simple closed-form analytical expressions that are easy to compute, require no numerical calculations and highlight the precise influence that each physical parameter has on the release profile. Moreover, an additional advantage that surrogate models can have over $\mathcal{P}_c(t)$ is in simplifying the process of fitting experimental data. For example, consider the one-term model (2.35) for Case B of Table 2.1,

$$S_1(t) = \exp \left(-\frac{d(d+2)D}{L^2 + \beta_1 L(d+2)} t \right). \quad (3.45)$$

If the diffusivity, D , of a material of interest is unknown, an estimate can be obtained by a simple rearrangement of (3.45),

$$D \approx -\frac{L^2 + \beta_1 L(d+2)}{d(d+2)t^*} \log(\mathcal{P}(t^*)), \quad (3.46)$$

where $t^* \in [0, T]$. Thus, for experimental observations of $\mathcal{P}(t)$, an estimate of the diffusivity, D , can be obtained by substituting in $\mathcal{P}(t^*)$, the observed proportion of particles remaining at time t^* , into (3.46). A limitation of this approach is that the one-term model does not accurately capture the early and late-time decay of $\mathcal{P}(t)$. Thus, the reliability of (3.46) depends on the time t^* and, hence, observation $\mathcal{P}(t^*)$ used in the estimation of the diffusivity.

3.3 Finite volume and time stepping schemes

In section 2.5, we briefly discussed the finite volume and time stepping schemes used to calculate numerical solutions of $c(r, t)$ for the homogeneous geometries and $c_1(r, t)$ and $c_2(r, t)$ for the heterogeneous geometries. The continuum analogue of $\mathcal{P}(t)$, given by the spatial average (2.17) or (2.18) for the homogeneous and heterogeneous geometries, respectively, was then calculated by using a trapezoidal rule approximation. In this section, we discuss the finite volume and time stepping schemes for discretising the continuum models (see section 2.3) in thorough detail.

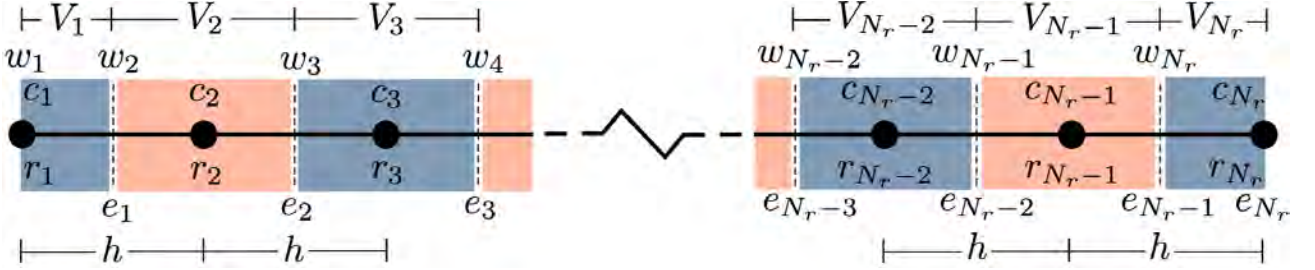


Figure 3.4: Schematic of a vertex-centred finite volume discretisation for a homogeneous radially-symmetric geometry. Here, c_i denotes the numerical approximation to $c(r_i, t)$ for $i = 1, 2, \dots, N_r$. The quantities V_i , w_i and e_i represent the i th control volume length, west boundary and east boundary, respectively. Additionally, the quantity h represents the uniform spacing between the nodes r_i .

3.3.1 Homogeneous materials

Considering the continuum model (2.4)–(2.7), we use a vertex-centred finite volume scheme to discretise in space for a homogeneous material, as shown in Figure 3.4. We define N_r nodes r_1, \dots, r_{N_r} on the radial domain $[\ell_0, \ell_1]$ such that $r_1 = \ell_0$ and $r_{N_r} = \ell_1$. The uniform spacing between the nodes is given by $h = (\ell_1 - \ell_0)/(N_r - 1)$, although a non-uniform spacing could also be used. Next, we define c_i as the numerical approximation of $c(r, t)$ at node r_i for $i = 1, \dots, N_r$. Additionally, we let $V_i = e_i - w_i$ denote the i th control volume, where

$$w_i = \begin{cases} r_1, & i = 1, \\ \frac{r_i + r_{i-1}}{2}, & i = 2, \dots, N_r, \end{cases} \quad e_i = \begin{cases} \frac{r_{i+1} + r_i}{2}, & i = 1, \dots, N_r - 1, \\ r_{N_r}, & i = N_r, \end{cases} \quad (3.47)$$

represent the west and east control volume boundaries, respectively. Next, rearranging the partial differential equation (2.4) and integrating over each control volume yields

$$\int_{w_i}^{e_i} r^{d-1} \frac{\partial c}{\partial t} dr = D \int_{w_i}^{e_i} \frac{\partial}{\partial r} \left(r^{d-1} \frac{\partial c}{\partial r} \right) dr.$$

We use the definition of the average concentration over the i th control volume,

$$\bar{c}_i = \frac{1}{V_i} \int_{w_i}^{e_i} r^{d-1} c(r, t) dr,$$

to obtain the following expression:

$$V_i \frac{d\bar{c}_i}{dt} = D \left[e_i^{d-1} \frac{\partial c}{\partial r}(e_i, t) - w_i^{d-1} \frac{\partial c}{\partial r}(w_i, t) \right].$$

Next, we introduce the approximation $\bar{c}_i \approx r_i^{d-1} c_i$ to obtain the following system of ordinary differential equations:

$$\frac{dc_i}{dt} = \frac{D}{V_i r_i^{d-1}} \left[e_i^{d-1} \frac{\partial c}{\partial r}(e_i, t) - w_i^{d-1} \frac{\partial c}{\partial r}(w_i, t) \right], \quad i = 1, 2, \dots, N_r.$$

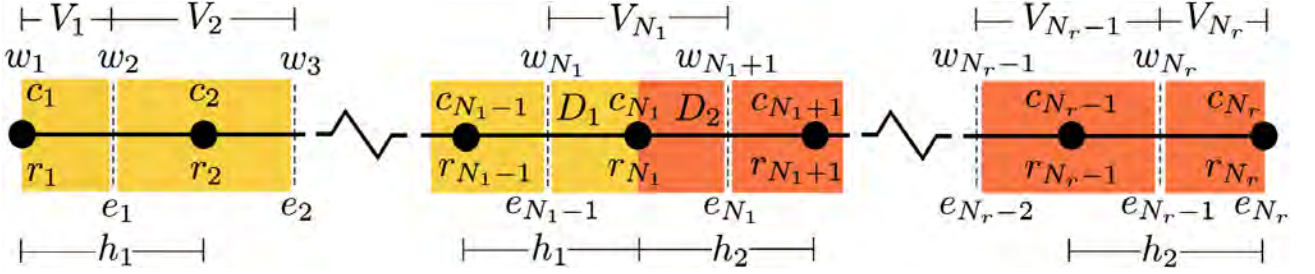


Figure 3.5: Schematic of a vertex-centred finite volume discretisation for a heterogeneous radially-symmetric geometry comprised of two concentric homogeneous layers. The inner layer has diffusivity D_1 , and the outer layer has diffusivity D_2 . Here, $c_1^{(j)}$ and $c_2^{(k)}$ denote the numerical approximations to $c_1(r_j, t)$ and $c_2(r_k, t)$, respectively, for $j = 1, \dots, N_1$ and $k = N_1 + 1, \dots, N_r$. The quantities V_i , w_i and e_i represent the i th control volume length, west boundary and east boundary, respectively, for $i = 1, 2, \dots, N_r$. Additionally, the quantities h_1 and h_2 represent the spacing between nodes r_j and r_k , respectively, for $j = 1, \dots, N_1$ and $k = N_1 + 1, \dots, N_r$.

Finally, by introducing central difference approximations for the spatial derivatives and incorporating the boundary conditions (2.6) and (2.7), we obtain

$$\frac{dc_1}{dt} = \frac{D}{V_1 \ell_0^{d-1}} \left[-\left(\frac{e_1^{d-1}}{h} + \frac{\ell_0^{d-1} a_0}{b_0} \right) c_1 + \frac{e_1^{d-1}}{h} c_2 \right], \quad (3.48)$$

$$\frac{dc_i}{dt} = \frac{D}{V_i r_i^{d-1} h} \left[w_i^{d-1} c_{i-1} - (w_i^{d-1} + e_i^{d-1}) c_i + e_i^{d-1} c_{i+1} \right], \quad i = 2, \dots, N_r - 1, \quad (3.49)$$

$$\frac{dc_{N_r}}{dt} = \frac{D}{V_{N_r} \ell_1^{d-1}} \left[\frac{w_{N_r}^{d-1}}{h} c_{N_r-1} - \left(\frac{w_{N_r}^{d-1}}{h} + \frac{\ell_1^{d-1} a_1}{b_1} \right) c_{N_r} \right]. \quad (3.50)$$

Note that, in the case where $\ell_0 = 0$ and $d > 1$, which implies a disc ($d = 2$) or sphere ($d = 3$) with radial symmetry at the origin, we obtain $c_1 = c_2$ and only require (3.49)–(3.50).

3.3.2 Heterogeneous materials

Considering the continuum model (2.8)–(2.14), we use a vertex-centred finite volume scheme to discretise in space for a heterogeneous material with two layers, as shown in Figure 3.5. We define $N_r = N_1 + N_2 - 1$ nodes $r_1, r_2, \dots, r_{N_1}, r_{N_1+1}, \dots, r_{N_r}$ on the radial domain $[\ell_0, \ell_2]$ such that $r_1 = \ell_0$, $r_{N_1} = \ell_1$ and $r_{N_r} = \ell_2$. The node spacings are defined as $h_1 = (\ell_1 - \ell_0)/(N_1 - 1)$ for r_1, r_2, \dots, r_{N_1} and $h_2 = (\ell_2 - \ell_1)/(N_2 - 1)$ for $r_{N_1+1}, r_{N_1+2}, \dots, r_{N_r}$. Here, we let $N_1 = \lceil \ell_1 N_r / \ell_2 \rceil$ and $N_2 = \lceil (\ell_2 - \ell_1) N_r / \ell_2 \rceil$, where $\lceil \cdot \rceil$ represents the ceiling function. Moreover, we define $c_1^{(j)}$ and $c_2^{(k)}$ as the numerical approximations of $c_1(r, t)$ and $c_2(r, t)$ at the nodes r_j and r_k for $j = 1, \dots, N_1$ and $k = N_1 + 1, \dots, N_r$, respectively. Again, we let $V_i = e_i - w_i$ represent the i th control volume for $i = 1, \dots, N_r$, where the control volume boundaries are given by (3.47). Next, rearranging the partial differential equations (2.8) and (2.9) and integrating over each control volume, we obtain

$$\begin{aligned}
\int_{w_j}^{e_j} r^{d-1} \frac{\partial c_1}{\partial t} dr &= D_1 \int_{w_j}^{e_j} \frac{\partial}{\partial r} \left(r^{d-1} \frac{\partial c_1}{\partial r} \right) dr, \quad j = 1, \dots, N_1 - 1, \\
\int_{w_k}^{e_k} r^{d-1} \frac{\partial c_2}{\partial t} dr &= D_2 \int_{w_k}^{e_k} \frac{\partial}{\partial r} \left(r^{d-1} \frac{\partial c_2}{\partial r} \right) dr, \quad k = N_1 + 1, \dots, N_r, \\
\int_{w_{N_1}}^{\ell_1} r^{d-1} \frac{\partial c_1}{\partial t} dr + \int_{\ell_1}^{e_{N_1}} r^{d-1} \frac{\partial c_2}{\partial t} dr \\
&= D_1 \int_{w_{N_1}}^{\ell_1} \frac{\partial}{\partial r} \left(r^{d-1} \frac{\partial c_1}{\partial r} \right) dr + D_2 \int_{\ell_1}^{e_{N_1}} \frac{\partial}{\partial r} \left(r^{d-1} \frac{\partial c_2}{\partial r} \right) dr
\end{aligned} \tag{3.51}$$

We use definitions of the average concentration over each control volume,

$$\begin{aligned}
\bar{c}_1^{(j)} &= \frac{1}{V_i} \int_{w_j}^{e_j} r^{d-1} c_1(r, t) dr, \quad j = 1, \dots, N_1 - 1, \\
\bar{c}_2^{(k)} &= \frac{1}{V_j} \int_{w_k}^{e_k} r^{d-1} c_2(r, t) dr, \quad k = N_1 + 1, \dots, N_r, \\
\bar{c}^* &= \frac{1}{V_{N_1}} \left[\int_{w_{N_1}}^{\ell_1} r^{d-1} c_1(r, t) dr + \int_{\ell_1}^{e_{N_1}} r^{d-1} c_2(r, t) dr \right],
\end{aligned}$$

to obtain the following expressions:

$$\begin{aligned}
V_j \frac{d\bar{c}_1^{(j)}}{dt} &= D_1 \left[e_j^{d-1} \frac{\partial c_1}{\partial r}(e_j, t) - w_j^{d-1} \frac{\partial c_1}{\partial r}(w_j, t) \right], \quad j = 1, \dots, N_1 - 1, \\
V_k \frac{d\bar{c}_2^{(k)}}{dt} &= D_2 \left[e_k^{d-1} \frac{\partial c_2}{\partial r}(e_k, t) - w_k^{d-1} \frac{\partial c_2}{\partial r}(w_k, t) \right], \quad k = N_1 + 1, \dots, N_r, \\
V_{N_1} \frac{d\bar{c}^*}{dt} &= D_2 e_{N_1}^{d-1} \frac{\partial c_2}{\partial r}(e_{N_1}, t) - D_1 w_{N_1}^{d-1} \frac{\partial c_1}{\partial r}(w_{N_1}, t).
\end{aligned} \tag{3.52}$$

The expression (3.52) is obtained from (3.51) by using the interface condition (2.14). Finally, we introduce the approximations $\bar{c}_1^{(j)} \approx r_j^{d-1} c_1^{(j)}$, $\bar{c}_2^{(k)} \approx r_k^{d-1} c_2^{(k)}$ and $\bar{c}^* \approx r_{N_1}^{d-1} c_1^{(N_1)}$. Thus, we obtain the following set of ordinary differential equations:

$$\begin{aligned}
\frac{dc_1^{(j)}}{dt} &= \frac{D_1}{V_j r_j^{d-1}} \left[e_j^{d-1} \frac{\partial c_1}{\partial r}(e_j, t) - w_j^{d-1} \frac{\partial c_1}{\partial r}(w_j, t) \right], \quad j = 1, \dots, N_1 - 1, \\
\frac{dc_2^{(k)}}{dt} &= \frac{D_2}{V_k r_k^{d-1}} \left[e_k^{d-1} \frac{\partial c_2}{\partial r}(e_k, t) - w_k^{d-1} \frac{\partial c_2}{\partial r}(w_k, t) \right], \quad k = N_1 + 1, \dots, N_r, \\
\frac{dc_1^{(N_1)}}{dt} &= \frac{1}{V_{N_1} r_{N_1}^{d-1}} \left[D_2 e_{N_1}^{d-1} \frac{\partial c_2}{\partial r}(e_{N_1}, t) - D_1 w_{N_1}^{d-1} \frac{\partial c_1}{\partial r}(w_{N_1}, t) \right].
\end{aligned}$$

By using central difference approximations for the spatial derivatives, and using the boundary conditions (2.11) and (2.12), we obtain

$$\frac{dc_1^{(1)}}{dt} = \frac{D_1}{V_1 \ell_0^{d-1}} \left[- \left(\frac{e_1^{d-1}}{h_1} + \frac{\ell_0^{d-1} a_0}{b_0} \right) c_1^{(1)} + \frac{e_1^{d-1}}{h_1} c_1^{(2)} \right], \tag{3.53}$$

$$\frac{dc_1^{(j)}}{dt} = \frac{D_1}{V_j r_j^{d-1} h_1} \left[w_j^{d-1} c_1^{(j-1)} - (w_j^{d-1} + e_j^{d-1}) c_1^{(j)} + e_j^{d-1} c_1^{(j+1)} \right], \quad j = 2, \dots, N_1 - 1, \quad (3.54)$$

$$\frac{dc_1^{(N_1)}}{dt} = \frac{1}{V_{N_1} \ell_1^{d-1}} \left[\frac{D_1 w_{N_1}^{d-1}}{h_1} \left(c_1^{(N_1-1)} - c_1^{(N_1)} \right) - \frac{D_2 e_{N_1}^{d-1}}{h_2} \left(c_2^{(N_1)} - c_2^{(N_1+1)} \right) \right], \quad (3.55)$$

$$\frac{dc_2^{(k)}}{dt} = \frac{D_2}{V_k r_k^{d-1} h_2} \left[w_k^{d-1} c_2^{(k-1)} - (w_k^{d-1} + e_k^{d-1}) c_2^{(k)} + e_k^{d-1} c_2^{(k+1)} \right], \quad k = N_1 + 1, \dots, N_r, \quad (3.56)$$

$$\frac{dc_2^{(N_r)}}{dt} = \frac{D_2}{V_{N_r} \ell_2^{d-1}} \left[\frac{w_{N_r}^{d-1}}{h_2} c_2^{(N_r-1)} - \left(\frac{w_{N_r}^{d-1}}{h_2} + \frac{\ell_1^{d-1} a_1}{b_1} \right) c_2^{(N_r)} \right]. \quad (3.57)$$

In the case of a disc or sphere with radial symmetry at the origin ($\ell_0 > 0$ and $d > 1$), we obtain $c_1^{(1)} = c_1^{(2)}$ from (3.53) and only require (3.54)–(3.57).

3.3.3 Crank-Nicolson method

The system of ordinary differential equations (3.48)–(3.50) or (3.53)–(3.57) yield the initial value problem,

$$\frac{d\mathbf{c}}{dt} = \mathbf{A}\mathbf{c}, \quad \mathbf{c}(0) = \mathbf{c}^{(0)}, \quad (3.58)$$

where $\mathbf{c} = (c_1, \dots, c_{N_r})^T$ contains the numerical solution at each node, $\mathbf{c}^{(0)} = (c_0, \dots, c_0)^T$ is the initial solution and $\mathbf{A} \in \mathbb{R}^{N_r \times N_r}$ contains the coefficients from (3.48)–(3.50) or (3.53)–(3.57). Next, we choose a sufficiently large time T over which to numerically solve for $c(r, t)$. The continuous time interval $0 \leq t \leq T$ is divided into M equally-spaced subintervals of width $\delta t = T/M$ such that $t_n = n\delta t$ for $n = 0, \dots, M$. The initial value problem (3.58) can be integrated over each subinterval $[t_n, t_{n+1}]$ to obtain

$$\int_{t_n}^{t_{n+1}} \frac{d\mathbf{c}}{dt} dt = \int_{t_n}^{t_{n+1}} \mathbf{A}\mathbf{c} dt.$$

We introduce an averaging approximation to obtain

$$\mathbf{c}^{(n+1)} - \mathbf{c}^{(n)} = \frac{\delta t}{2} [\mathbf{A}\mathbf{c}^{(n)} + \mathbf{A}\mathbf{c}^{(n+1)}],$$

which, when rearranged, yields the Crank-Nicolson time-stepping scheme

$$\left(\mathbf{I} - \frac{\delta t}{2} \mathbf{A} \right) \mathbf{c}^{(n+1)} = \left(\mathbf{I} + \frac{\delta t}{2} \mathbf{A} \right) \mathbf{c}^{(n)}. \quad (3.59)$$

Here, $\mathbf{c}^{(n)} = (c_1^n, c_2^n, \dots, c_{N_r}^n)^T$ contains the numerical approximation of $c(r, t)$ at node r_i and time point t_n , $c_i^n \approx c(r_i, t_n)$, for $i = 1, \dots, N_r$ and $n = 0, \dots, M$. Given the initial solution $\mathbf{c}^{(0)} = (c_0, \dots, c_0)^T$ is known, the solution at time step t_1 can be obtained by solving the linear system (3.59) with $n = 0$. Thus, the solution at time step t_{n+1} , $\mathbf{c}^{(n+1)}$, can be obtained given

prior calculation of $\mathbf{c}^{(1)}, \mathbf{c}^{(2)}, \dots, \mathbf{c}^{(n)}$ by repetitious solving of (3.59). In the case of an absorbing inner or outer boundary, or a reflecting inner boundary for circular or spherical geometries, minor modifications are made to the linear system (3.59). The code that implements the finite volume and time stepping schemes, and includes these minor modifications, is available on GitHub (https://github.com/lukefilippini/Filippini_2023.git).

3.4 Results for one- and three-dimensional geometries

In section 2.5, we presented comparisons between the three surrogate models (2.35), (2.45) and (2.60) and the stochastic and continuum analogues (2.3) and (2.17) or (2.18), respectively, for the seven test cases of Table 2.2. These results were for two-dimensional radially-symmetric geometries. Here, we present the model comparisons and results for one- and three-dimensional radially-symmetric geometries, which are similar to those for the two-dimensional case. Figure 3.6 and Figure 3.7 are the results for Cases A–E for one ($d = 1$) and three ($d = 3$) dimensions, respectively. For Cases F and G, the results for one ($d = 1$) and three ($d = 3$) dimensions are presented in Figure 3.8 and Figure 3.9, respectively.

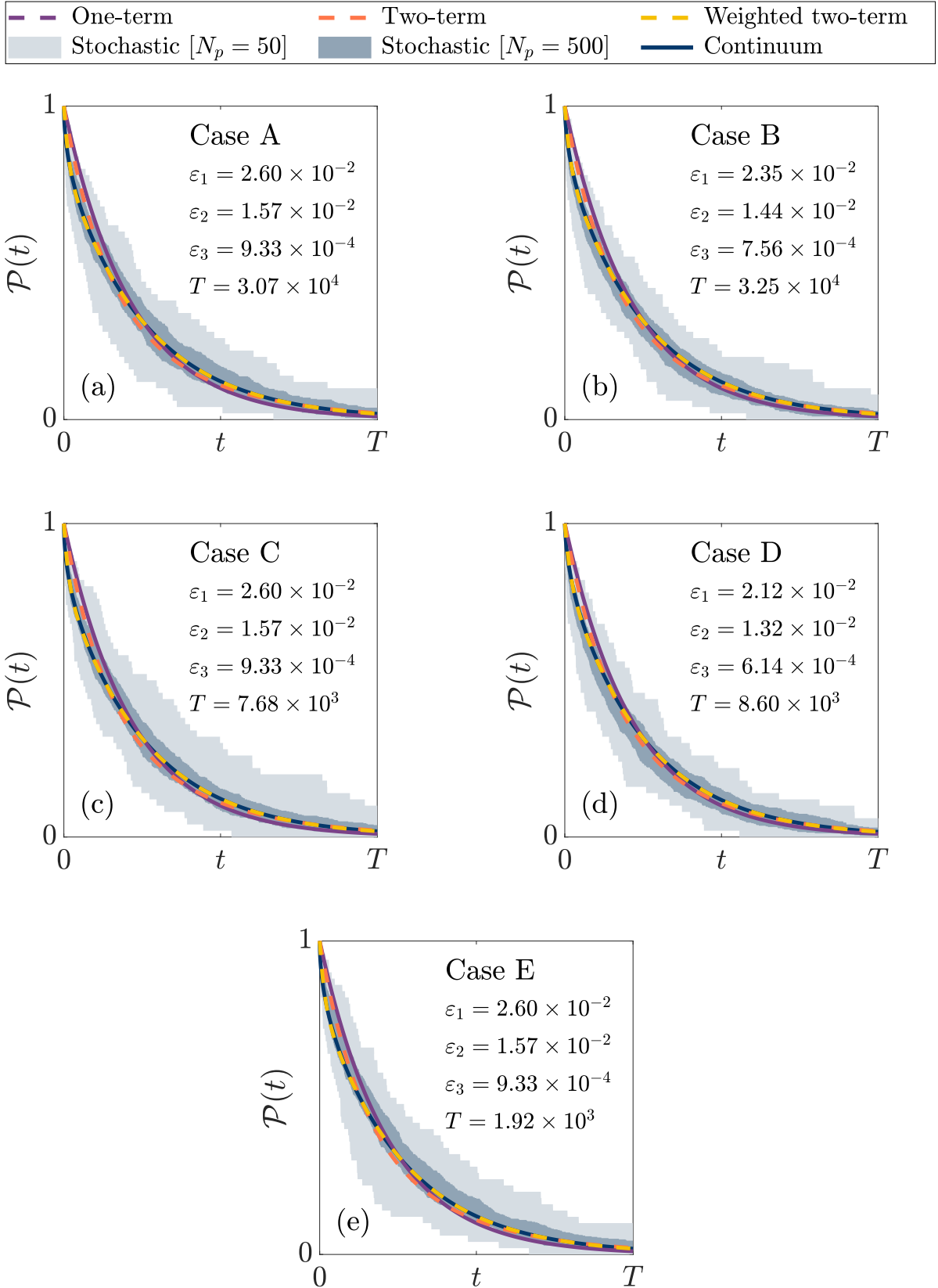


Figure 3.6: One-term, two term, and weighted two-term exponential models for $\mathcal{P}(t)$ compared with stochastic and continuum models for the homogeneous test cases (Cases A–E) with $d = 1$. For the stochastic model, the bounds of the shaded regions represent the maximum and minimum proportion of particles remaining at each point in time across the $N_s = 100$ simulations. The mean absolute errors ε_1 , ε_2 and ε_3 and final time T are rounded to three significant digits.

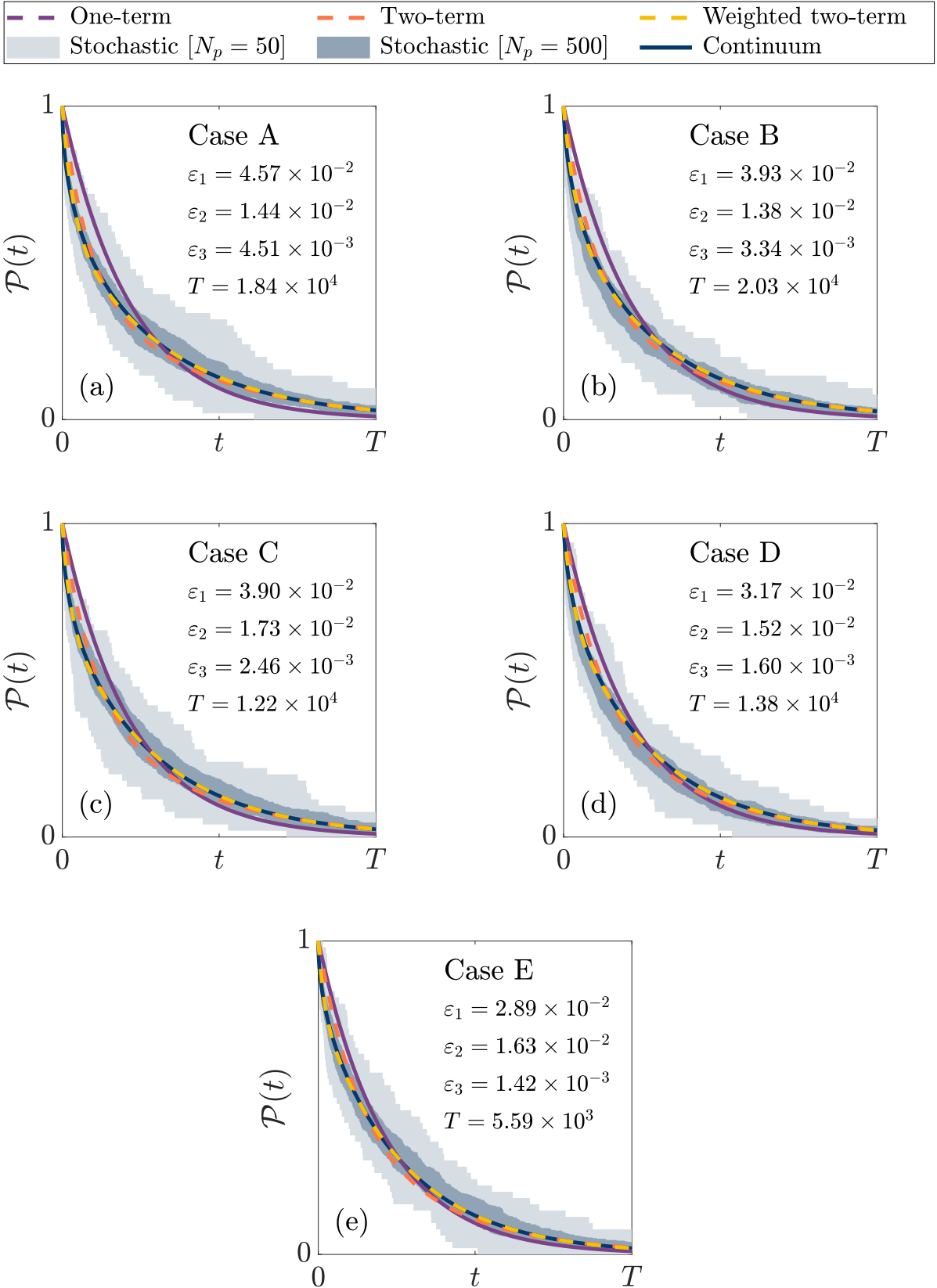


Figure 3.7: One-term, two term, and weighted two-term exponential models for $\mathcal{P}(t)$ compared with stochastic and continuum models for the homogeneous test cases (Cases A–E) with $d = 3$. For the stochastic model, the bounds of the shaded regions represent the maximum and minimum proportion of particles remaining at each point in time across the $N_s = 100$ simulations. The mean absolute errors ε_1 , ε_2 and ε_3 and final time T are rounded to three significant digits.

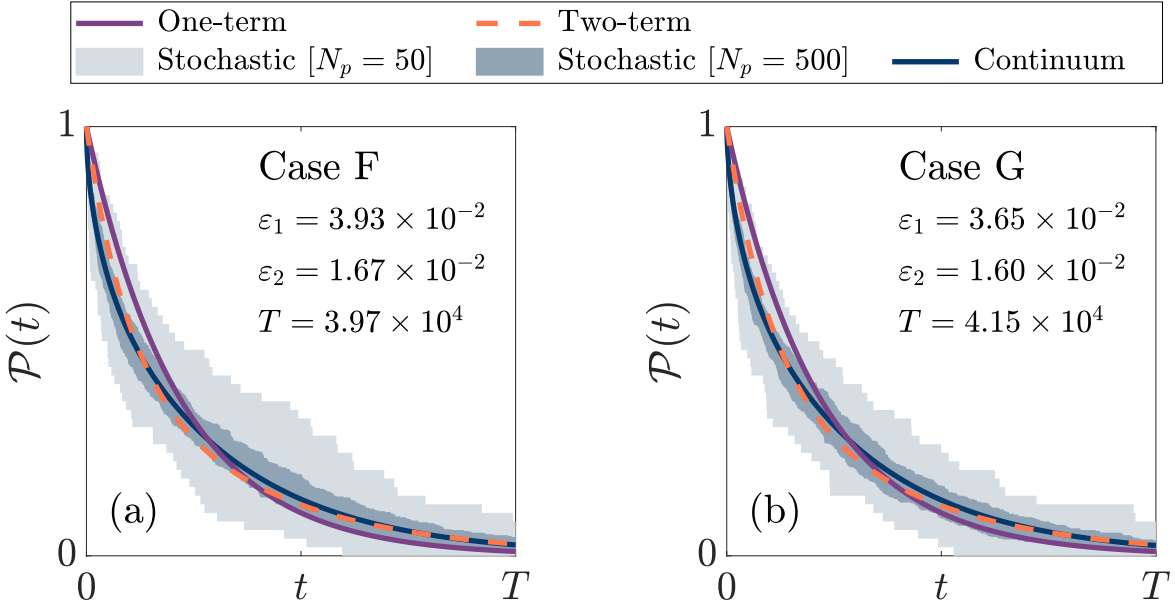


Figure 3.8: One-term and two-term exponential models for $\mathcal{P}(t)$ compared with stochastic and continuum models for the heterogeneous test cases (Cases F–G) with $d = 1$. For the stochastic model, the bounds of the shaded regions represent the maximum and minimum proportion of particles remaining at each point in time across the $N_s = 100$ simulations. The mean absolute errors ε_1 and ε_2 and final time T are rounded to three significant digits.

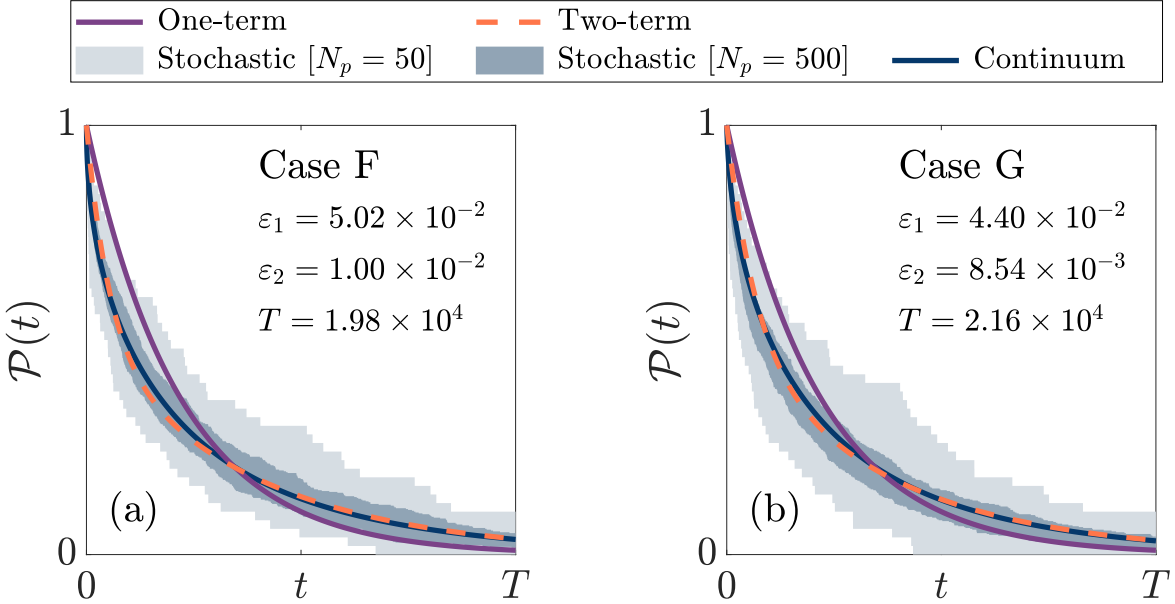


Figure 3.9: One-term and two-term exponential models for $\mathcal{P}(t)$ compared with stochastic and continuum models for the heterogeneous test cases (Cases F–G) with $d = 3$. For the stochastic model, the bounds of the shaded regions represent the maximum and minimum proportion of particles remaining at each point in time across the $N_s = 100$ simulations. The mean absolute errors ε_1 and ε_2 and final time T are rounded to three significant digits.

3.5 Additional project considerations

Finally, in section 2.6, we briefly touched on some avenues for future research and potential extensions of the work presented in this thesis. Here, we discuss potential avenues of future research that were explored during candidature, in addition to the work presented in chapter 2. The ideas in this section were outside of the scope of this thesis, but are considered to have enough potential significance to be included in this supporting chapter. In the three cases explored below, we consider the one-term model (2.35) and derive an analytical expression for the rate parameter λ . Firstly, we consider a system with a non-zero steady state $c_\infty(r)$ for the homogeneous geometries. Secondly, we discuss how the diffusivity for a heterogeneous radially-symmetric geometry can be represented as a smooth function which depends on the radial position, rather than a piecewise function. Lastly, we consider how the introduction of a reaction component in the transport system affects the construction of the one-term model (2.35) for the homogeneous geometries.

3.5.1 Non-zero steady-state

We account for the possibility of a non-zero steady-state $c_\infty(r) = \lim_{t \rightarrow \infty} c(r, t)$ and reconsider the one-term model (2.35). Considering the continuum model (2.4)–(2.7) for the homogeneous geometries, we make a small change in the boundary conditions (2.6) and (2.7),

$$a_0 c(\ell_0, t) - b_0 \frac{\partial c}{\partial r}(\ell_0, t) = e_0, \quad t > 0, \quad (3.60)$$

$$a_1 c(\ell_1, t) + b_1 \frac{\partial c}{\partial r}(\ell_1, t) = e_1, \quad t > 0, \quad (3.61)$$

which implies that the dimensionless particle concentration $c(r, t)$ will not decay to zero if $e_0 \neq 0$ and/or $e_1 \neq 0$. Note that $e_0 = \tilde{e}_0/\tilde{c}_0$ and $e_1 = \tilde{e}_1/\tilde{c}_0$ where \tilde{e}_0 and \tilde{e}_1 represent the number of particles per unit length/area/volume outside the inner and outer boundaries, respectively. Now, we alter the one-term model (2.35) in the following manner:

$$S_1(t) = C_\infty + (1 - C_\infty)e^{-\lambda t}, \quad (3.62)$$

$$C_\infty = \frac{d}{\ell_1^d - \ell_0^d} \int_{\ell_0}^{\ell_1} r^{d-1} c_\infty(r) dr. \quad (3.63)$$

Here, $C_\infty = \langle c_\infty(r) \rangle$, expressed as (3.63), represents the spatial average of the steady-state concentration, $c_\infty(r)$. The one-term model (3.62) is appropriate as it agrees with the continuum analogue $\mathcal{P}_c(t)$ (2.17) at initial time ($\mathcal{P}_c(0) = 1$) and has the correct limiting behaviour at large times (i.e. $\lim_{t \rightarrow \infty} \mathcal{P}_c(t) = C_\infty$). To determine an analytical expression for the parameter λ of the one-term model (3.62), we propose the following condition:

$$\int_0^\infty [S_1(t) - C_\infty] dt = \int_0^\infty [\mathcal{P}_c(t) - C_\infty] dt. \quad (3.64)$$

The expression (3.64) enforces the condition that the area enclosed between C_∞ and $S_1(t)$ must be equal to that between C_∞ and $\mathcal{P}_c(t)$. Substituting the one-term model (2.35), the continuum analogue (2.17) and the steady-state average (3.63) into (3.64), and rearranging the right hand side, we obtain

$$(1 - C_\infty) \int_0^\infty e^{-\lambda t} dt = \frac{d}{\ell_1^d - \ell_0^d} \int_{\ell_0}^{\ell_1} r^{d-1} \left[\int_0^\infty c(r, t) - c_\infty(r) dt \right] dr.$$

Integrating and evaluating on the left hand side, we arrive at

$$\begin{aligned} \frac{1 - C_\infty}{\lambda} &= \langle M_0(r) \rangle, \\ M_0(r) &= \int_0^\infty c(r, t) - c_\infty(r) dt, \\ \langle M_0(r) \rangle &= \frac{d}{\ell_1^d - \ell_0^d} \int_{\ell_0}^{\ell_1} r^{d-1} M_0(r) dr. \end{aligned} \tag{3.65}$$

Finally, the expression (3.65) is inverted to give an analytical form for λ ,

$$\lambda = \frac{1 - C_\infty}{\langle M_0(r) \rangle}. \tag{3.66}$$

The result (3.66) provides insight into the role of the boundary conditions (3.60)–(3.61) on the proportion of particles over time, $\mathcal{P}(t)$. Hence, this illustrates that the moment-matching approach discussed in this thesis can be extended to account for a non-zero steady state.

3.5.2 Smooth diffusivity function

We now consider heterogeneous geometries defined by a smooth diffusivity $D(r)$ and determine a unique expression for the one-term model (2.35). The general form of the rate parameter expression (2.37), given as $\lambda = 1/\langle M_0(r) \rangle$, does not change as we are no longer accounting for a non-zero steady state. Rather, we define a new boundary value problem, involving the diffusivity function $D(r)$, which $M_0(r)$ satisfies and compute the spatial average $\langle M_0(r) \rangle$ using (3.8). Here, we consider Case B of Table 2.1. Firstly, the initial-boundary value problem for this scenario is defined as

$$\begin{aligned} \frac{\partial c}{\partial t} &= \frac{1}{r^{d-1}} \frac{\partial}{\partial r} \left(r^{d-1} D(r) \frac{\partial c}{\partial r} \right), \quad 0 < r < L, \quad t > 0, \\ c(r, 0) &= 1, \quad 0 \leq r \leq L, \\ \frac{\partial c}{\partial r}(0, t) &= 0, \quad c(L, t) + \beta_1 \frac{\partial c}{\partial r}(L, t) = 0, \quad t > 0. \end{aligned}$$

By integrating the above initial-boundary value problem over time, we obtain a boundary value problem which $M_0(r)$ satisfies,

$$\begin{aligned} \frac{1}{r^{d-1}} \frac{d}{dr} \left(r^{d-1} D(r) \frac{dM_0}{dr} \right) &= -1, \quad 0 < r < L, \\ \frac{dM_0}{dr}(0) &= 0, \quad M_0(L) + \beta_1 \frac{dM_0}{dr}(L) = 0. \end{aligned}$$

The solution $M_0(r)$ of this boundary value problem and the average $\langle M_0(r) \rangle$ are given by

$$\begin{aligned} M_0(r) &= \frac{1}{d} \left[\int_0^L \frac{r}{D(r)} dr - \int_0^r \frac{z_1}{D(z_1)} dz_1 + \frac{\beta_1 L}{D(L)} \right], \\ \langle M_0(r) \rangle &= \frac{1}{d} \left[\int_0^L \frac{r}{D(r)} dr - \frac{d}{L^d} \int_0^L r^{d-1} \int_0^r \frac{z_1}{D(z_1)} dz_1 + \frac{\beta_1 L}{D(L)} \right]. \end{aligned} \quad (3.67)$$

Note that the expressions (3.11) and (3.12) for $M_0(r)$ and $\langle M_0(r) \rangle$, respectively, for homogeneous geometries are recovered by setting $D(r) = D$. For particular choices of the diffusivity function $D(r)$, the integrals within the spatial average (3.67) could be evaluated, yielding closed-form expressions for the rate parameter λ and, hence, the one-term model (2.35).

3.5.3 Addition of reaction term

Finally, we include a reaction term in the model (2.4)–(2.7) for the homogeneous geometries and determine a unique expression for the one-term model (2.35). We define a new boundary value problem, involving the reaction term, which $M_0(r)$ (2.21) satisfies and compute the spatial average $\langle M_0(r) \rangle$ using (3.8). We again consider Case B of Table 2.1. Firstly, we redefine the initial-boundary value problem (2.4)–(2.7) to include a reaction term for decay,

$$\begin{aligned} \frac{\partial c}{\partial t} &= \frac{D}{r^{d-1}} \frac{\partial}{\partial r} \left(r^{d-1} \frac{\partial c}{\partial r} \right) - \gamma c, \quad 0 < r < L, \quad t > 0, \\ c(r, 0) &= 1, \quad 0 \leq r \leq L, \\ \frac{\partial c}{\partial r}(0, t) &= 0, \quad c(L, t) + \beta_1 \frac{\partial c}{\partial r}(L, t) = 0, \quad t > 0. \end{aligned}$$

By integrating the above initial-boundary value problem over time, we obtain a boundary value problem which $M_0(r)$ satisfies,

$$\begin{aligned} \frac{D}{r^{d-1}} \frac{d}{dr} \left(r^{d-1} \frac{dM_0}{dr} \right) - \gamma M_0(r) &= -1, \quad 0 < r < L, \\ \frac{dM_0}{dr}(0) &= 0, \quad M_0(L) + \beta_1 \frac{dM_0}{dr}(L) = 0. \end{aligned}$$

The solution $M_0(r)$, for $d = 1$, of this boundary value problem and the spatial average $\langle M_0(r) \rangle$ are given by

$$M_0(r) = \frac{1}{\gamma} \left[1 - \frac{\cosh(\sqrt{\gamma r/D})}{\cosh(\sqrt{\gamma L/D}) + \beta_1 \sqrt{\gamma/D} \sinh(\sqrt{\gamma L/D})} \right],$$

$$\langle M_0(r) \rangle = \frac{1}{\gamma L} \left[L - \frac{\sqrt{\gamma/D} \sinh(\sqrt{\gamma/D} L)}{\cosh(\sqrt{\gamma L/D}) + \beta_1 \sqrt{\gamma/D} \sinh(\sqrt{\gamma L/D})} \right].$$

This illustrates that it is possible to derive analytical formulas for the one-term model (2.35) which highlight the influence of key physical parameters, including the reaction term γ , on $\mathcal{P}(t)$.

Chapter 4

Conclusion

4.1 Summary and discussion

In this thesis, we have considered the problem of diffusion-controlled particle release from d -dimensional radially-symmetric geometries with absorbing, reflecting and/or semi-absorbing boundaries. The purpose of this work, motivated by two research objectives, was to develop novel surrogate models to describe $\mathcal{P}(t)$, the proportion of particles remaining with the geometry over time. This work was motivated by drug delivery and thin-layer drying applications, where surrogate models are frequently used to approximate quantities analogous to $\mathcal{P}(t)$. Previous surrogate models included exponential, Weibull and other exponential-like functions to describe $\mathcal{P}(t)$ and related quantities [48, 49] for homogeneous slab, circular and spherical geometries with radial symmetry [19, 22, 23, 26, 27, 39, 58]. Motivated by Carr [18], we presented one-term, two-term and weighted two-term exponential models for $\mathcal{P}(t)$ obtained by matching moments with the continuum analogue of the stochastic diffusion model. This approach produced relatively simple closed-form analytical approximations of $\mathcal{P}(t)$ that are computationally inexpensive to evaluate and avoid the limitations associated with the stochastic and continuum descriptions of $\mathcal{P}(t)$. The surrogate models are expressed explicitly in terms of physical parameters of the diffusive transport system, and, thus, allow for meaningful analytical insight into the precise influence of each physical parameter on the release profile.

In Chapter 2, we presented the manuscript submitted to *Physica A* (April 2023). In this chapter, we developed novel exponential models to describe $\mathcal{P}(t)$. Firstly, we reproduced the one-term model (2.35) presented by Carr [18] by matching the zeroth moments of $S_1(t)$ and the continuum analogue of the stochastic diffusion model, $\mathcal{P}_c(t)$. Secondly, we developed the two-term model (2.45) by matching the zeroth and first moments of $S_2(t)$ and $\mathcal{P}_c(t)$. Finally, the weighted two-term model (2.60) was obtained by matching the zeroth, first and second moments of $S_3(t)$ and $\mathcal{P}_c(t)$. In total, we considered three main problems: (i) homogeneous slab, circular and spherical geometries with an absorbing or semi-absorbing boundary, (ii) homogeneous slab, annular and spherical shell geometries with absorbing, reflecting and/or semi-absorbing boundaries and (iii) heterogeneous slab, circular and spherical geometries with an absorbing or semi-absorbing boundary. For each of the seven test cases considered (Cases A–

G, [Table 2.1](#)), the weighted two-term and/or two-term model captured the early and late-time decay of $\mathcal{P}(t)$ more accurately than the one-term model. In particular, the weighted two-term model captured the stochastic and continuum descriptions of $\mathcal{P}(t)$ with the highest degree of accuracy. The most significant finding was that this model is more simplistic and accurate than the one-term Weibull model developed by Carr [\[18\]](#).

Chapter [3](#) contained supporting information for the manuscript presented in Chapter [2](#). Firstly, we developed exact analytical expressions, by using separation of variables and eigenfunction expansion, for $\mathcal{P}_c(t)$. To elaborate, we considered Case B of [Table 2.1](#), presenting exact solutions for a homogeneous slab, disc and sphere with radial symmetry at the origin and a semi-absorbing boundary. The limitations associated with these analytical solutions, including root approximations and truncation requirements, were then discussed in detail. Moreover, we provided a thorough derivation of the one-term, two-term and weighted models in section [3.2](#). Firstly, we determined a general solution for each model by matching moments with the continuum analogue $\mathcal{P}_c(t)$. We then considered Cases B, E and G of [Table 2.1](#) and constructed boundary value problems for the zeroth and first moment of particle lifetime. For the second moment, we considered Cases B and E for the homogeneous geometries. Several unique solutions for the surrogate models were then reproduced. Also, we discussed how the one-term model [\(2.35\)](#) could be used to simplify the process of fitting experimental data by obtaining an estimate of the diffusivity for Case B. Moreover, we provided the finite volume and time-stepping schemes used to compute $\mathcal{P}(t)$ for the continuum model. Additionally, we presented the results for the seven test cases of [Table 2.2](#) for one- and three-dimensional radially-symmetric geometries. These results illustrated that the weighted two-term and/or two-term models capture the early and late-time decay of $\mathcal{P}(t)$ more accurately than the one-term model. Finally, we discussed additional work conducted throughout candidature that could be considered as avenues for potential future research.

4.2 Future work

There are several avenues that could be explored in future as an extension of the work presented in this thesis. To begin, there are other functional forms of $\mathcal{P}(t)$ that can potentially be investigated, in addition to the one-term, two-term and weighted two-term models presented in this work. For example, many other exponential and exponential-like functions have been used in thin-layer drying applications, as summarised by Akpinar et al. [\[41\]](#), Ertekin et al. [\[42\]](#) and Onwude et al. [\[39\]](#). The moment-matching approach outlined in this thesis and by Carr [\[18\]](#) could be used directly or modified to develop new surrogate models for $\mathcal{P}(t)$ based on these other functional forms. This could ideally yield a model simpler in construction than the weighted two-term model [\(2.60\)](#) with a similar level of accuracy.

Moreover, we assume throughout this work that particles are always initially uniformly distributed within the radially-symmetric geometry. Another extension of this research could involve accounting for a non-uniform initial distribution of particles. This could be practically

relevant in drug delivery research, as several modelling approaches have been investigated for release from multi-layered core-shell capsules. The drug is initially distributed within a core shell and must diffuse through multiple concentric layers, which do not initially contain the drug, before it reaches the external environment [25, 28, 29]. Additionally, we have considered heterogeneous geometries with two concentric layers, so there is the potential to extend this work to consider radially-symmetric geometries with additional layers or a smooth diffusivity (see section 3.5.2). Lastly, the heterogeneous geometries could also be approximated by homogeneous domains with an effective diffusivity, D_{eff} . There are several approximations for D_{eff} that could be investigated [56], which implies that surrogate models for the homogeneous geometries could be used instead.

Appendix

A. Surrogate model parameter values

Here, we present the one-term (2.35), two-term (2.45) and weighted two-term (2.60) exponential models corresponding to Cases A–G (see Table 2.2) by providing numerical values for the parameters appearing in each surrogate model. All values are rounded to three significant figures and presented in tables separated by dimension.

Case	One-term		Two-term		Two-term (weighted)		
	λ	λ_1	λ_2	λ_1	λ_2	θ	
A	1.50×10^{-4}	1.04×10^{-4}	2.71×10^{-4}	1.23×10^{-4}	2.13×10^{-4}	8.12×10^{-1}	
B	1.42×10^{-4}	9.95×10^{-5}	2.45×10^{-4}	1.19×10^{-4}	1.84×10^{-3}	8.27×10^{-1}	
C	6.00×10^{-4}	4.15×10^{-4}	1.09×10^{-3}	4.94×10^{-4}	8.51×10^{-3}	8.12×10^{-1}	
D	5.36×10^{-4}	3.83×10^{-4}	8.92×10^{-4}	4.56×10^{-4}	6.57×10^{-3}	8.41×10^{-1}	
E	2.40×10^{-3}	1.66×10^{-3}	4.34×10^{-3}	1.96×10^{-3}	3.40×10^{-2}	8.12×10^{-1}	
F	1.16×10^{-4}	7.34×10^{-5}	2.79×10^{-4}	—	—	—	
G	1.11×10^{-4}	7.13×10^{-5}	2.51×10^{-3}	—	—	—	

Table A1: Surrogate model parameters for Cases A–G appearing in the one-term (2.35), two-term (2.45) and weighted two-term (2.60) exponential models ($d = 1$).

Case	One-term		Two-term		Two-term (weighted)		
	λ	λ_1	λ_2	λ_1	λ_2	θ	
A	2.00×10^{-4}	1.27×10^{-4}	4.73×10^{-4}	1.45×10^{-4}	1.65×10^{-3}	6.99×10^{-1}	
B	1.85×10^{-4}	1.21×10^{-4}	3.98×10^{-4}	1.39×10^{-4}	1.39×10^{-3}	7.24×10^{-1}	
C	4.16×10^{-4}	2.75×10^{-4}	8.55×10^{-4}	3.22×10^{-4}	4.58×10^{-3}	7.58×10^{-1}	
D	3.70×10^{-4}	2.54×10^{-4}	6.80×10^{-4}	3.00×10^{-4}	3.50×10^{-3}	7.93×10^{-1}	
E	1.19×10^{-3}	8.20×10^{-4}	2.17×10^{-3}	9.76×10^{-4}	1.61×10^{-2}	8.08×10^{-1}	
F	1.75×10^{-4}	1.02×10^{-4}	6.09×10^{-4}	—	—	—	
G	1.63×10^{-4}	9.79×10^{-5}	4.90×10^{-4}	—	—	—	

Table A2: Surrogate model parameters for Cases A–G appearing in the one-term (2.35), two-term (2.45) and weighted two-term (2.60) exponential models ($d = 2$).

Case	One-term		Two-term		Two-term (weighted)		
	λ	λ_1	λ_2	λ_1	λ_2	θ	
A	2.50×10^{-4}	1.51×10^{-4}	7.24×10^{-4}	1.66×10^{-4}	1.58×10^{-3}	6.23×10^{-1}	
B	2.27×10^{-4}	1.42×10^{-4}	5.61×10^{-4}	1.59×10^{-4}	1.29×10^{-3}	6.57×10^{-1}	
C	3.78×10^{-4}	2.40×10^{-4}	8.95×10^{-4}	2.75×10^{-4}	3.34×10^{-3}	7.03×10^{-1}	
D	3.34×10^{-4}	2.21×10^{-4}	6.81×10^{-4}	2.57×10^{-4}	2.52×10^{-3}	7.44×10^{-1}	
E	8.24×10^{-4}	5.57×10^{-4}	1.58×10^{-3}	6.59×10^{-4}	9.58×10^{-3}	7.85×10^{-1}	
F	2.33×10^{-4}	1.32×10^{-4}	9.86×10^{-4}	—	—	—	
G	2.13×10^{-4}	1.26×10^{-4}	6.98×10^{-4}	—	—	—	

Table A3: Surrogate model parameters for Cases A–G appearing in the one-term (2.35), two-term (2.45) and weighted two-term (2.60) exponential models ($d = 3$).

B. Integral evaluations

The one-term, two-term and weighted two-term models for Cases C, D, E and G in [Table 2.1](#), outlined in sections [2.4.3](#), [2.4.4](#) and [2.4.5](#), respectively, depend on various geometrical constants I_1, I_2, I_3, I_4 and I_5 . These constants are expressed as definite integrals for succinctness. Closed-form expressions for these integrals, evaluated for $d = 1, 2, 3$, are given below:

Homogeneous geometries

$$\begin{aligned}
 I_1(r) &= \begin{cases} r - \ell_0, & \text{for } d = 1, \\ \log(r/\ell_0), & \text{for } d = 2, \\ (r - \ell_0)/(r\ell_0), & \text{for } d = 3, \end{cases} \\
 I_2(r) &= \begin{cases} \frac{1}{2}(r - \ell_0)^2, & \text{for } d = 1, \\ \frac{1}{4}[2r^2 \log(r/\ell_0) - (r^2 - \ell_0^2)], & \text{for } d = 2, \\ (r - \ell_0)^2(\ell_0 + 2r)/(6\ell_0), & \text{for } d = 3, \end{cases} \\
 I_3(r) &= \begin{cases} \frac{1}{3}(r - \ell_0)^3, & \text{for } d = 1, \\ \frac{1}{4}[(r^2 + \ell_0^2) \log(r/\ell_0) - (r^2 - \ell_0^2)], & \text{for } d = 2, \\ (r - \ell_0)^3/(6r\ell_0), & \text{for } d = 3, \end{cases} \\
 I_4(r) &= \begin{cases} \frac{1}{4}(r - \ell_0)^4, & \text{for } d = 1, \\ \frac{1}{64}[4r^2(r^2 + 2\ell_0^2) \log(r/\ell_0) + \ell_0^2 - 5r^4 + 4r^2\ell_0^2], & \text{for } d = 2, \\ (r - \ell_0)^4(\ell_0 + 4r)/(120\ell_0), & \text{for } d = 3, \end{cases} \\
 I_5(r) &= \begin{cases} \frac{1}{5}(r - \ell_0)^5, & \text{for } d = 1, \\ \frac{1}{128}[2(r^4 + 4r^2\ell_0^2 + \ell_0^4) \log(r/\ell_0) - 3(r^4 - \ell_0^4)], & \text{for } d = 2, \\ (r - \ell_0)^5/(120r\ell_0), & \text{for } d = 3. \end{cases}
 \end{aligned}$$

Heterogeneous geometries

$$I_1^{(1)}(r) = \begin{cases} r - \ell_0, & \text{for } d = 1, \\ \log(r/\ell_0), & \text{for } d = 2, \\ (r - \ell_0)/(r\ell_0), & \text{for } d = 3, \end{cases} \quad \text{and} \quad I_1^{(2)}(r) = \begin{cases} r - \ell_1, & \text{for } d = 1, \\ \log(r/\ell_1), & \text{for } d = 2, \\ (r - \ell_1)/(r\ell_1), & \text{for } d = 3. \end{cases}$$

Bibliography

- [1] H. C. Berg. *Random walks in biology*. Princeton University Press, 1993.
- [2] P. C. Bressloff. *Stochastic Processes in Cell Biology*, volume 2 of *Interdisciplinary Applied Mathematics*. Springer Cham, Switzerland, 2021. doi: [10.1007/978-3-030-72519-8](https://doi.org/10.1007/978-3-030-72519-8).
- [3] E. A. Codling, M. J. Plank, and S. Benhamou. Random walk models in biology. *Journal of the Royal Society Interface*, 5(25):813–834, 2008. doi: [10.1098/rsif.2008.0014](https://doi.org/10.1098/rsif.2008.0014).
- [4] A. Okubo and S. A. Levin. *Diffusion and Ecological Problems: Modern Perspectives*. Springer, New York, 2nd edition, 2001. doi: [10.1007/978-1-4757-4978-6](https://doi.org/10.1007/978-1-4757-4978-6).
- [5] G. A. Truskey, F. Yuan, and D. F. Katz. *Transport Phenomena in Biological Systems*. Pearson Education, New Jersey, 2nd edition, 2009.
- [6] S. Karlin. *A First Course in Stochastic Processes*. Academic Press, United States, 1968.
- [7] S. A. Levin, T. G. Hallam, and L. J. Gross. *Applied mathematical ecology*, volume 18. Springer-Verlag, 2012.
- [8] M. K. Das, P. P. Mukherjee, and K. Muralidhar. *Modeling Transport Phenomena in Porous Media with Applications*. Mechanical Engineering Series. Springer International Publishing, Cham, Switzerland, 1st edition, 2018. doi: [10.1007/978-3-319-69866-3](https://doi.org/10.1007/978-3-319-69866-3).
- [9] N. Merhav. *Statistical physics for electrical engineering*. Springer, 2017. doi: [10.1007/978-3-319-62063-3](https://doi.org/10.1007/978-3-319-62063-3).
- [10] N. G. van Kampen. *Stochastic Processes in Physics and Chemistry*. Elsevier, Amsterdam, 3rd edition, 2007.
- [11] A. Jain, S. McGinty, G. Pontrelli, and L. Zhou. Theoretical modeling of endovascular drug delivery into a multilayer arterial wall from a drug-coated balloon. *International Journal of Heat and Mass Transfer*, 187, 2022. doi: [10.1016/j.ijheatmasstransfer.2022.122572](https://doi.org/10.1016/j.ijheatmasstransfer.2022.122572).
- [12] J. Siepmann, R. A. Siegel, and M. J. Rathbone. *Fundamentals and Applications of Controlled Release Drug Delivery*. Springer, New York, 2012. doi: [10.1007/978-1-4614-0881-9](https://doi.org/10.1007/978-1-4614-0881-9).
- [13] F. C. Collins and G. E. Kimball. Diffusion-controlled reaction rates. *Journal of Colloid Science*, 4(4):425–437, 1949. doi: [10.1016/0095-8522\(49\)90023-9](https://doi.org/10.1016/0095-8522(49)90023-9).

- [14] J. L. Plawsky. *Transport Phenomena Fundamentals*. Chemical Industries. CRC Press, Boca Raton, 4th edition, 2020. doi: [10.1201/9781315113388](https://doi.org/10.1201/9781315113388).
- [15] E. J. Carr and C. J. Wood. Rear-surface integral method for calculating thermal diffusivity: Finite pulse time correction and two-layer samples. *International Journal of Heat and Mass Transfer*, 144:118609, 2019. doi: [10.1016/j.ijheatmasstransfer.2019.118609](https://doi.org/10.1016/j.ijheatmasstransfer.2019.118609).
- [16] E. J. Carr and L. P. Filippini. Analytical formulas for calculating the thermal diffusivity of cylindrical shell and spherical shell samples. *International Journal of Heat and Mass Transfer*, 202:123693, 2023. doi: [10.1016/j.ijheatmasstransfer.2022.123693](https://doi.org/10.1016/j.ijheatmasstransfer.2022.123693).
- [17] M. S. Gomes-Filho, M. A. A. Barbosa, and F. A. Oliveira. A statistical mechanical model for drug release: Relations between release parameters and porosity. *Physica A: Statistical Mechanics and its Applications*, 540:123165, 2020. doi: <https://doi.org/10.1016/j.physa.2019.123165>.
- [18] E. J. Carr. Exponential and weibull models for spherical and spherical-shell diffusion-controlled release systems with semi-absorbing boundaries. *Physica A: Statistical Mechanics and its Applications*, 605:127985, 2022. doi: [10.1016/j.physa.2022.127985](https://doi.org/10.1016/j.physa.2022.127985).
- [19] M. Ignacio, M. Bagheri, M. V. Chubynsky, H. W. de Haan, and G. W. Slater. Diffusivity interfaces in lattice Monte Carlo simulations: Modeling inhomogeneous delivery and release systems. *Physical Review E*, 105(6):064135, 2022. doi: [10.1103/PhysRevE.105.064135](https://doi.org/10.1103/PhysRevE.105.064135).
- [20] S. Redner. *A Guide to First-Passage Processes*. Cambridge University Press, New York, 2001.
- [21] M. J. Simpson and R. E. Baker. Exact calculations of survival probability for diffusion on growing lines, disks, and spheres: The role of dimension. *Journal of Chemical Physics*, 143(9), 2015. doi: [10.1063/1.4929993](https://doi.org/10.1063/1.4929993).
- [22] M. Ignacio, M. V. Chubynsky, and G. W. Slater. Interpreting the Weibull fitting parameters for diffusion-controlled release data. *Physica A: Statistical Mechanics and its Applications*, 486:486–496, 2017. doi: [10.1016/j.physa.2017.05.033](https://doi.org/10.1016/j.physa.2017.05.033).
- [23] J. Siepmann and F. Siepmann. Modeling of diffusion controlled drug delivery. *Journal of Controlled Release*, 161(2):351–362, 2012. doi: [10.1016/j.jconrel.2011.10.006](https://doi.org/10.1016/j.jconrel.2011.10.006).
- [24] W. H. A. Schilders, H. A Van der Vorst, and J. Rommes. *Model order reduction: theory, research aspects and applications*, volume 13. Springer, 2008.
- [25] B. Kaoui, M. Lauricella, and G. Pontrelli. Mechanistic modelling of drug release from multi-layer capsules. *Computers in Biology and Medicine*, 93:149–157, 2018. doi: [10.1016/j.combiomed.2017.12.010](https://doi.org/10.1016/j.combiomed.2017.12.010).

- [26] D. Y. Arifin, L. Y. Lee, and C. H. Wang. Mathematical modeling and simulation of drug release from microspheres: Implications to drug delivery systems. *Advanced Drug Delivery Reviews*, 58(12–13):1274–1325, 2006. doi: [10.1016/j.addr.2006.09.007](https://doi.org/10.1016/j.addr.2006.09.007).
- [27] S. Dash, P. N. Murthy, L. Nath, and P. Chowdhury. Kinetic modeling on drug release from controlled drug delivery systems. *Acta Poloniae Pharmaceutica*, 67(3):217–223, 2010.
- [28] E. J. Carr and G. Pontrelli. Drug delivery from microcapsules: How can we estimate the release time? *Mathematical Biosciences*, 315:108216, 2019. doi: [10.1016/j.mbs.2019.108216](https://doi.org/10.1016/j.mbs.2019.108216).
- [29] E. J. Carr and G. Pontrelli. Modelling mass diffusion for a multi-layer sphere immersed in a semi-infinite medium: application to drug delivery. *Mathematical Biosciences*, 303:1–9, 2018. doi: [10.1016/j.mbs.2018.04.004](https://doi.org/10.1016/j.mbs.2018.04.004).
- [30] A. S. Timin, D. J. Gould, and G. B. Sukhorukov. Multi-layer microcapsules: fresh insights and new applications. *Expert Opinion on Drug Delivery*, 14(5):583–587, 2017. doi: [10.1080/17425247.2017.1285279](https://doi.org/10.1080/17425247.2017.1285279).
- [31] L. Simon and J. Ospina. A three-dimensional semi-analytical solution for predicting drug release through the orifice of a spherical device. *International Journal of Pharmaceutics*, 509(1-2):477–482, 2016. doi: [10.1016/j.ijpharm.2016.06.020](https://doi.org/10.1016/j.ijpharm.2016.06.020).
- [32] M. Hayek. An exact solution for a nonlinear diffusion equation in a radially symmetric inhomogeneous medium. *Computers & Mathematics with Applications*, 68(12):1751–1757, 2014. doi: [10.1016/j.camwa.2014.10.015](https://doi.org/10.1016/j.camwa.2014.10.015).
- [33] T. Higuchi. Mechanism of sustained-action medication. theoretical analysis of rate of release of solid drugs dispersed in solid matrices. *Journal of Pharmaceutical Sciences*, 52(12):1145–1149, 1963. doi: [10.1002/jps.2600521210](https://doi.org/10.1002/jps.2600521210).
- [34] L. Simon and J. Ospina. *Closed-form solutions for drug transport through controlled-release devices in two and three dimensions*. Closed-form Solutions for Drug Transport through Controlled-Release Devices in Two and Three Dimensions. John Wiley & Sons, Inc., 2015. doi: [10.1002/9781119055976](https://doi.org/10.1002/9781119055976).
- [35] R. S. Langer and D. L. Wise. *Medical Applications of Controlled Release, Applications and Evaluation*, volume 1–2. CRC Press, Boca Raton, 1984.
- [36] J. R. Robinson and V. H. L. Lee. *Controlled Drug Delivery*. Marcel Dekker, Inc., New York, 1987.
- [37] L. A. Duc, J. W. Han, and D. H. Keum. Thin layer drying characteristics of rape-seed (*Brassica napus* L.). *Journal of Stored Products Research*, 47(1):32–38, 2011. doi: [10.1016/j.jspr.2010.05.006](https://doi.org/10.1016/j.jspr.2010.05.006).
- [38] M. Aghbashlo, M. H. Kianmehr, S. Khani, and M. Ghasemi. Mathematical modelling of thin-layer drying of carrot. *International Agrophysics*, 23(4):313–317, 2009.

- [39] D. I. Onwude, N. Hashim, R. B. Janius, N. M. Nawi, and K. Abdan. Modeling the thin-layer drying of fruits and vegetables: A review. *Comprehensive Reviews in Food Science and Food Safety*, 15(3):599–618, 2016. doi: [10.1111/1541-4337.12196](https://doi.org/10.1111/1541-4337.12196).
- [40] V. Chasiotis, D. Tzempelikos, D. Mitrakos, and A. Filios. Numerical and experimental analysis of heat and moisture transfer of *Lavandula x allardii* leaves during non-isothermal convective drying. *Journal of Food Engineering*, 311, 2021. doi: [10.1016/j.jfoodeng.2021.110708](https://doi.org/10.1016/j.jfoodeng.2021.110708).
- [41] E. K. Akpinar. Determination of suitable thin layer drying curve model for some vegetables and fruits. *Journal of Food Engineering*, 73(1):75–84, 2006. doi: [10.1016/j.jfoodeng.2005.01.007](https://doi.org/10.1016/j.jfoodeng.2005.01.007).
- [42] C. Ertekin and M. Z. Firat. A comprehensive review of thin-layer drying models used in agricultural products. *Critical Reviews in Food Science and Nutrition*, 57(4):701–717, 2017. doi: [10.1080/10408398.2014.910493](https://doi.org/10.1080/10408398.2014.910493).
- [43] A. Midilli, H. Kucuk, and Z. Yapar. A new model for single-layer drying. *Drying Technology*, 20(7):1503–1513, 2002. doi: [10.1081/DRT-120005864](https://doi.org/10.1081/DRT-120005864).
- [44] J. Crank. *The Mathematics of Diffusion*. Clarendon Press, Oxford, 2nd edition, 1975.
- [45] M. Özdemir, F. G. Seyhan, A. Ö Bodurb, and Y. O. Devres. Effect of initial moisture content on the thin layer drying characteristics of hazelnuts during roasting. *Drying Technology*, 18(7):1465–1479, 2000. doi: [10.1080/07373930008917788](https://doi.org/10.1080/07373930008917788).
- [46] Z. Erbay and F. Icier. A review of thin layer drying of foods: Theory, modeling, and experimental results. *Critical Reviews in Food Science and Nutrition*, 50(5):441–464, 2010. doi: [10.1080/10408390802437063](https://doi.org/10.1080/10408390802437063).
- [47] M. Fortes and M. R. Okos. Non-equilibrium thermodynamics approach to heat and mass transfer in corn kernels. *Transactions of the ASAE*, 24(3):761–769, 1981. doi: [10.13031/2013.34335](https://doi.org/10.13031/2013.34335).
- [48] C. J. Andrews, L. Cuttle, and M. J. Simpson. Quantifying the role of burn temperature, burn duration and skin thickness in an in vivo animal skin model of heat conduction. *International Journal of Heat and Mass Transfer*, 101:542–549, 2016. doi: [10.1016/j.ijheatmasstransfer.2016.05.070](https://doi.org/10.1016/j.ijheatmasstransfer.2016.05.070).
- [49] M. J. Simpson. Depth-averaging errors in reactive transport modeling. *Water Resources Research*, 45(2), 2009. doi: [10.1029/2008WR007356](https://doi.org/10.1029/2008WR007356).
- [50] R. W. Baker and H. S. Lonsdale. *Controlled Release from Biologically Active Agents*. Plenum Press, New York, 1974.

- [51] A. El-Beltagy, G. R. Gamea, and A. H. Amer Essa. Solar drying characteristics of strawberry. *Journal of Food Engineering*, 78(2):456–464, 2007. doi: [10.1016/j.jfoodeng.2005.10.015](https://doi.org/10.1016/j.jfoodeng.2005.10.015).
- [52] M. S. Zenoozian, H. Feng, S. M. A. Razavi, F. Shahidi, and H. R. Pourreza. Image analysis and dynamic modeling of thin-layer drying of osmotically dehydrated pumpkin. *Journal of Food Processing and Preservation*, 32(1):88–102, 2008. doi: [10.1111/j.1745-4549.2007.00167.x](https://doi.org/10.1111/j.1745-4549.2007.00167.x).
- [53] D. A. Tzempelikos, A. P. Vouros, A. V. Bardakas, A. E. Filios, and D. P. Margaris. Experimental study on convective drying of quince slices and evaluation of thin-layer drying models. *Engineering in Agriculture, Environment and Food*, 8(3):169–177, 2015. doi: [10.1016/j.eaef.2014.12.002](https://doi.org/10.1016/j.eaef.2014.12.002).
- [54] A. O. Omolola, A. I. O. Jideani, and P. F. Kapila. Modeling microwave drying kinetics and moisture diffusivity of Mabonde banana variety. *International Journal of Agricultural and Biological Engineering*, 7(6):107–113, 2014. doi: [10.3965/j.ijabe.20140706.013](https://doi.org/10.3965/j.ijabe.20140706.013).
- [55] W. P. da Silva, C. M. D. P. S. Silva, J. A. R. de Sousa, and V. S. O. Farias. Empirical and diffusion models to describe water transport into chickpea (*Cicer arietinum* L.). *International Journal of Food Science and Technology*, 48(2):267–273, 2013. doi: [10.1111/j.1365-2621.2012.03183.x](https://doi.org/10.1111/j.1365-2621.2012.03183.x).
- [56] E. J. Carr and M. J. Simpson. New homogenization approaches for stochastic transport through heterogeneous media. *The Journal of Chemical Physics*, 150(4):044104, 2019. doi: [10.1063/1.5067290](https://doi.org/10.1063/1.5067290).
- [57] E. J. Carr, J. M. Ryan, and M. J. Simpson. Diffusion in heterogeneous discs and spheres: New closed-form expressions for exit times and homogenization formulas. *Journal of Chemical Physics*, 153(7), 2020. doi: [10.1063/5.0010810](https://doi.org/10.1063/5.0010810).
- [58] P. Lötstedt and L. Meinecke. Simulation of stochastic diffusion via first exit times. *Journal of Computational Physics*, 300:862–886, 2015. doi: [10.1016/j.jcp.2015.07.065](https://doi.org/10.1016/j.jcp.2015.07.065).
- [59] G. Vaccario, C. Antoine, and J. Talbot. First-passage times in d -dimensional heterogeneous media. *Physical Review Letters*, 115(24), 2015. doi: [10.1103/PhysRevLett.115.240601](https://doi.org/10.1103/PhysRevLett.115.240601).
- [60] O. Corzo, N. Bracho, A. Pereira, and A. Vásquez. Weibull distribution for modeling air drying of coroba slices. *LWT - Food Science and Technology*, 41(10):2023–2028, 2008. doi: [10.1016/j.lwt.2008.01.002](https://doi.org/10.1016/j.lwt.2008.01.002).
- [61] R. Erban and S. J. Chapman. Reactive boundary conditions for stochastic simulations of reaction-diffusion processes. *Physical Biology*, 4(1):16–28, 2007. doi: [10.1088/1478-3975/4/1/003](https://doi.org/10.1088/1478-3975/4/1/003).

- [62] E. J. Carr and I. W. Turner. A semi-analytical solution for multilayer diffusion in a composite medium consisting of a large number of layers. *Applied Mathematical Modelling*, 40(15):7034–7050, 2016. doi: [10.1016/j.apm.2016.02.041](https://doi.org/10.1016/j.apm.2016.02.041).
- [63] R. I. Hickson, S. I. Barry, and G. N. Mercer. Critical times in multilayer diffusion. Part 1: Exact solutions. *International Journal of Heat and Mass Transfer*, 52(25):5776–5783, 2009. doi: [10.1016/j.ijheatmasstransfer.2009.08.013](https://doi.org/10.1016/j.ijheatmasstransfer.2009.08.013).
- [64] M. J. Simpson, A. P. Browning, D. J. Warne, O. J. Maclaren, and R. E. Baker. Parameter identifiability and model selection for sigmoid population growth models. *Journal of Theoretical Biology*, 535:110998, 2022.
- [65] Mathworks. MATLAB **fzero**, 2023. <https://au.mathworks.com/help/matlab/ref/fzero.html> (Accessed: May 2023).
- [66] Mathworks. MATLAB **bvp4c**, 2023. <https://au.mathworks.com/help/matlab/ref/bvp4c.html> (Accessed: May 2023).
- [67] Wolfram. Mathematica, 2023. <https://www.wolfram.com/mathematica/> (Accessed: June 2023).